Aalborg University

Spring 2011

Assessment of Vibrations in Floors Excited by Rhythmical Human Force

Lars Horsager
Mads Rosager Mortensen
Michael Thorgaard Kristensen

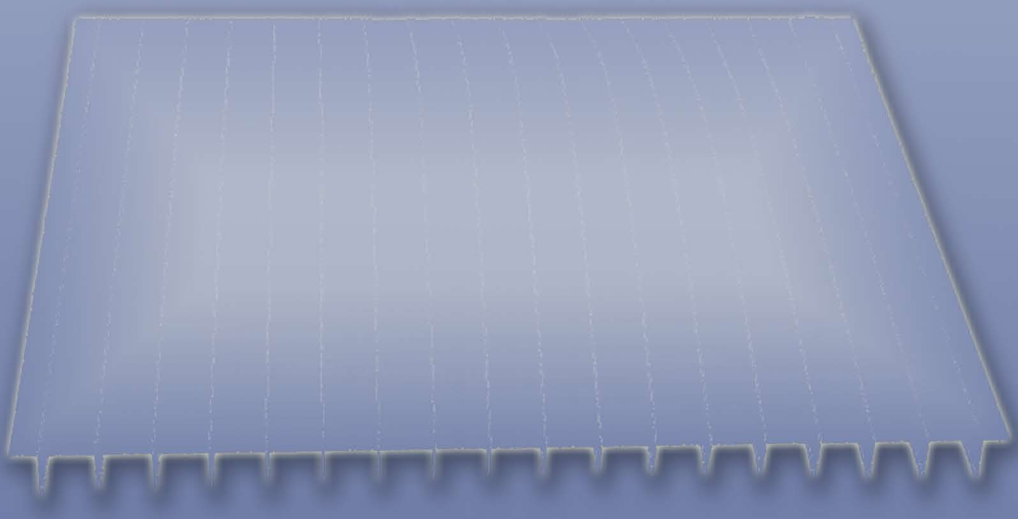

Master's Thesis
M.Sc. Programme in Structural and Civil Engineering

Title: Assessment of Vibrations in Floors Excited by Rhythmical Human Force

Project period: Spring 2011

Project type: Master's Thesis

Project group: B120b

Participants:

Lars Horsager

Mads Rosager Mortensen

Michael Thorgaard Kristensen

Supervisor:
Lars Pedersen

Synopsis:

An actual deck in the cultural centre of Nordkraft is analyzed with respect to structural vibrations. The deck forms the floor of a sports hall and is placed on top of a theatre hall. The construction is suspected to be excitable by human jumping loads in an critical manner, and the response of the deck towards this load type has the main focus.
At first, a frequency analysis of the deck is performed in order to clarify the natural frequencies, vibration modes as well as other modal parameters. From this knowledge, the structural response from human-induced jumping loads is analyzed and compared to the limit values given in the relevant building code. During both the frequency analysis and response analysis different techniques are utilized including analytical and numerical methods, as well as experimental measurements on the actual construction. Results from the different approaches are compared and assessed.
Through experiments, characteristic properties of human-induced jumping loads are described, and this is used to assess the load expressions, which has been used to model the human jumping loads.

Number printed: 5 copies

Number of pages: 131 pages

Enclosed: Appendix CD containing calculations

Finished: June 9, 2011

Dansk resumé

Dette speciale er udarbejdet i foråret 2011 af studiegruppe B120b som afslutningen på uddannelsesforløbet ved Aalborg Universitet til: Kandidat i Bygge- og Anlægskonstruktion. Rapportens titel er: *Vurdering af vibrationer i gulve påvirket af rytmisk personlast* og tager sit udgangspunkt i en konkret dækkonstruktion i Nordkraft-bygningen i Aalborg. Dækkonstruktionen antages at være kritisk med hensyn til påvirkninger fra rytmisk personlast, og opgavens primære formål er derfor at undersøge dækkonstruktionens dynamiske respons overfor denne lasttype. Dækket er opbygget af ni forspændte TTD dækelementer med overbeton, og konstruktionen dækker et areal på 16.3×21.6 m, hvor elementerne spænder i den korte retning.

På den undersøgte dækkonstruktion i Nordkraft-bygningen har DGI-Huset en idrætshal, og dækket bliver således udsat for forskellige former for rytmisk personlast. Under dækkonstruktionen findes den største af Teater Nordkrafts teatersale. Analysen af dækkets dynamiske opførsel deles i en egensvingningsanalyse, hvor egenfrekvenser og egensvingningsformer bestemmes, samt en responsanalyse, hvor dækket antages påvirket af en rytmisk personlast fra hop.

Egensvingningsanalyse

Egenfrekvenser samt egensvingningsformer analyseres med både analytiske, numeriske og eksperimentielle metoder. De numeriske modeller er opstillet i det kommercielle beregningsprogram ABAQUS og både solid- såvel som skalfiniteelementmodeller er anvendt. Endvidere betragtes både bjælke- såvel som plademodeller af varierende kompleksitet i de analytiske og numeriske metoder. Det findes ved sammenligning med eksperimentielle målinger, at plademodellerne er bedst egnede til beregning af dækkets egenfrekvenser og egensvingningsformer. Derimod er bjælkemodellerne kun anvendelige til bestemmelse af den første svingningsform. Ud fra forsøg findes de tre første egenværdier til at være henholdsvis 8.3 Hz, 9.4 Hz og 11.0 Hz.

Resultaterne fra de analytiske og numeriske modeller vurderes ud fra forsøgene på dækket, og stivheden anvendt i beregningsmodellerne opdateres, således at en bedre overensstemmelse mellem egenfrekvenser fra forsøg og modeller opnås. Desuden illustreres fordele og ulemper ved de enkelte analysemetoder.

Responsanalyse

De opdaterede modeller bruges herefter til den egentlige vurdering af gulvets dynamiske respons, hvis underlagt en rytmisk hoppelast. Det ønskes her undersøgt, hvorvidt det for udvalgte lastscenarier er muligt at opnå vibrationer, som er i strid med de for anvendelsesgrænsetilstanden normgivne værdier, målt i accelerationsniveau. Her tages udgangspunkt i det danske nationale anneks til Eurocode, hvor en øvre grænse på 10 % af tyngdeaccelerationen for standardafvigelsen af accelerationen angives [10].

Til at simulere den rytmiske personlast anvendes to forskellige lastmodeller. Den første lastmodel er angivet i det danske nationale anneks til Eurocode, Eurocode-modellen, mens den anden lastmodel er angivet i en artikel af Ellis & Ji [8], Ellis & Ji-modellen. Der tages udgangspunkt i laster, som kan frembringes af maksimalt 20 hoppende personer. I forbindelse med anvendelsen af lastmodellerne udføres laboratorieforsøg for at vurdere visse af de brugte inputparametre. Beskrivelsen af disse forsøg er vedlagt rapporten som bilag.

Fra den indledende undersøgelse af gulvkonstruktionen, blev det fundet at tre vibrationsformer ville være dominerende for den dynamiske respons, og der opstilles derfor tre lastscenarier. Hvert lastscenarie svarer til en placering af den rytmiske personlast på dækket, som vil

anslå én af de første tre egensvingningsformer maksimalt. For hvert lastscenarie tilpasses hoppefrekvensen ligeledes, således resonans opnås for hver af de tre første egensvingningsformer. Disse scenarier modelleres analytisk, numerisk og eksperimentielt. De analytiske løsninger bygger på en antagelse om modal dekobling, mens den numeriske løsning foretages i ABAQUS ved hjælp af samme skalmodel, som blev anvendt i egensvingningsanalysen. Løsningen i ABAQUS bygger på direkte integration af de styrende svingningsligninger for hvert tidsskridt.

De fundne resultater sammenlignes, hvorved fordele og ulemper mellem de enkelte metoder kan kommenteres. Det findes, at Eurocode-modellen generelt giver mindre præcise resultater for accelerationsniveauet for de valgte lastscenarier på grund af nogle basale antagelser omkring frekvensfordelingen i lastmodellen, mens anvendelse af Ellis & Ji-modellen genererer rimelig virkelighedstro værdier. De fundne accelerationsniveauer anvendes til at kommentere og opstille scenarier, hvor anvendelsesgrænseværdierne kan blive overskredet, og chancen for at opnå et sådant scenarie kommenteres.

Ud over forskellene mellem de to anvendte lastmodeller, findes den anvendte beregningsmetode ligeledes at have afgørende betydning. Metoderne, hvor modal dekomposition antages, giver mindre præcise resultater sammenlignet med eksperimentielle målinger i forhold til ABAQUS-resultaterne. Samlet set synes resultaterne af responsanalysen at være meget følsomme overfor både den anvendte lastmodel samt den beregningsmetode, som vælges.

Preface

This Master's Thesis has been prepared by three students at Aalborg University and is the final work concluding the educational programme: Master of Science in Engineering in Structural and Civil Engineering. The project period has lasted from February 2011 until June 2011 as a full time study.

The report is divided into a main part and appendices, which are enclosed at the end of the main part. In addition to the written report, an Appendix CD is enclosed. Here, calculation files and documents from various programs, which have been used during the project work, can be found. Program names are written with a different font, e.g. MATLAB, and reference to a specific file is made with a third font in the following way: `filename.ext`.

Acknowledgements

The subject of the Master's Thesis has involved a considerable amount of experimental work on the deck, which is investigated. In order to plan the experiments, detailed knowledge of the construction was essential. In this respect, the authors would like to thank Lars Damgaard, from the engineering consultant company Korsbæk & Partners, for providing construction drawings and calculations as well as helping to formulate the problem of this thesis. We also greatly appreciate the detailed calculation drawings from the company of Spæncom, which helped us improve our analyses.

During the experimental work, the involved tenants of Nordkraft, which are DGI-Huset on top of the deck, and Teater Nordkraft under the deck, have been very helpful in finding suitable times for conducting experiments and for putting their equipment at our disposal. Finally, we would like to thank the 20 volunteers who helped us conduct the final experiment on the deck.

Lars Horsager
Mads Rosager Mortensen
Michael Thorgaard Kristensen
Aalborg University, June 2011

Contents

List of Symbols

Symbols included in the main report are shown in the following list. Auxiliary symbols might be found in appendices, where an explanation to them also can be found.

Latin symbols	
A, B, C, D	Integration constants to be found from initial conditions / boundary conditions.
$a(t)$	Acceleration a at time t.
a_i, b_i	Coefficients of load model.
a_{max}	Maximum value of acceleration during time series.
a_{rms}	Root-mean-square value of acceleration during time series.
A_{cab}	Cross sectional area of prestressed cable.
A_{rib}	Cross sectional area of rib in TTD element.
$A(t)$	Time dependent amplitude function.
c, c_{h}	Modal damping coefficient of structure and human, respectively.
c_{r}	Contact ratio, $c_{\text{r}} = t_{\text{c}} / T_{\text{p}}$.
C_i	Crowd reduction factor for the i^{th} jumping load component.
$\mathbf{C}$	Damping matrix.
D_{cab}	Diameter of prestressed cable.
D	Dynamic amplification factor.
$D, D_{\text{x}}, D_{\text{y}}, D_{\text{xy}}$	Flexural and torsional stiffnesses.
$E_{\text{c}}, E_{\text{s}}$	Young's modulus of concrete and steel, respectively.
EI	Bending stiffness (used in general sense before choosing Young's modulus and moment of inertia).
f	Cyclic natural frequency, $f = \omega/2\pi$.
f_{ck}	Characteristic strength of concrete.
f_{h}	Fundamental frequency of human.
f_{p}	Jumping frequency.
$f_{mn}(t)$	Time dependent modal forcing function.
$\mathbf{f}$	Matrix of modal forcing functions.
$F(t)$	Time dependent forcing function.
g_{mn}	Static modal load.
G	Static weight of humans.
G_{s}	Equivalent static weight of humans.
H	Effective torsional stiffness of plate, $H = \nu D + 2D_{\text{xy}}$.
H_i	Structural response factor of i^{th} jumping load component.
I, I_{t}	Moment of inertia and transformed moment of inertia, respectively.
I_{p}	Polar moment of rib.
i, I	Number of load component of human jumping load, and total number of load components considered in a specific load model, respectively.
j, N	Index for jumping humans, and total number of jumping humans, respectively.
$J_{\text{x}}, J_{\text{y}}$	Rotary inertia of ribs in x- and y-direction, respectively.
k, k_{h}	Modal stiffness of structure and human, respectively.
k_{a}	Acceleration response factor.
k_{F}	Load response factor.
$\mathbf{K}$	Stiffness matrix.
$L_{\text{x}}, L_{\text{y}}$	Dimensions of deck in x- and y-direction.
m, m_{h}	Modal mass of structure and human, respectively.
$M_{\text{p}}, M_{\text{s}}$	Mass of plate and stiffeners, respectively.
$\mathbf{M}$	Mass matrix.

continues…

n, m	Vibration mode number in x- and y-direction, respectively.
N_e	Number of “effective” humans.
q	Modal coordinate describing structure motion.
$\mathbf{q}$	Matrix of modal coordinates.
q_h	Modal coordinate describing motion of human.
s	Number of ribs / stiffeners in y-direction.
S	Standard deviation of stochastic variable.
t	Thickness of deck / Time.
Δt	Time step.
t_{tot}	Total time of analysis.
t_c	Contact time during the jumping load period, T_p.
T	Period of vibration.
T_p	Period of jumping load.
T_{max}	Maximum kinetic energy.
U_{max}	Maximum potential energy.
u	Displacement of deck in z-direction.
u_p	Deflection due to the static human load G.
V	Coefficient of variation.
X	Load effect.
$\|X\|$	Force amplitude.

Greek symbols

α_i	Fourier coefficient of the i^{th} jumping load component.
β	Length to width ratio, $\beta = L_y/L_x$.
γ	Mass per unit length of ribs / stiffeners.
$\Gamma_\alpha, \Lambda_\alpha, \Psi_\alpha$	Constants.
δ	Logarithmic decrement.
Δ	Non dimensional stiffness parameter.
ϵ	Scaling factor, $\epsilon = E_s/E_c$.
ζ, ζ_h	Damping ratio of structure and human, respectively.
η	Reduction factor due to load distribution.
θ	Angle, $\theta = \pi/2 - \varphi$.
λ	Auxiliary parameter, $\lambda^4 = \mu\omega^2 L_x^4/EI$.
μ	Mass per unit length of TTD element.
ν_c, ν_s	Poisson’s ratio of concrete and steel, respectively.
$\rho, \overline{\rho}$	Density of reinforced concrete, and equivalent mass per unit area of orthotropic plate, respectively.
ρ_i	Correlation coefficients of the i^{th} jumping load component.
σ_a	Standard deviation of acceleration.
τ	Time (used in calculations when t designates thickness).
φ_i	Phase lag for the i^{th} jumping load component.
Φ	Shape function.
Ψ	Phase lag of response compared to load.
ω	Circular natural frequency, $\omega = f \cdot 2\pi$.
ω_p	Circular forcing frequency.

Chapter 1

Introduction

Near the water front of Aalborg city centre lies the newly renovated building of Nordkraft, an old power plant now utilized for cultural activities such as sports, concerts, cafés, theatres, and cinemas. Due to its historical usage as a power plant building, the complex comprising Nordkraft is rather large and not originally designed for purposes where vibrations and noise could be a problem. As a consequence, the combination of different activities gives rise to high demands on the magnitude of vibration and noise transmission through walls and floors.

The project revolves around a part of the floor construction of the rightmost of the two larger sports halls situated on the second level in Nordkraft. In Figure 1.1 a cut through the building is shown and the relevant sports floor is marked. This sports floor separates the sports hall from the main theatre hall of "Theatre Nordkraft". At present, noise inconvenience can be experienced in the theatre hall, when the sports hall is used. This is due to direct sound transmission through the deck and shaking of lighting equipment attached to the underside of the deck, which is affected by vibrations in the deck. From this it could be asked whether the structural vibrations of the deck are of a magnitude, which also causes inconvenience for the users of the sports hall. An assessment of this question will be the main focus of this report.

Figure 1.1: Cross sectional cut through Nordkraft [19].

Naturally, the magnitude of vibrations in the deck is dependent on the type of activity in the sports hall. The human-induced forces, which causes the vibrations, differ according to the activity of the humans. However, in order to examine a critical situation, focus will be on human-induced jumping loads, as these are the most powerful human loads [3].

The considered deck consists of 9 prestressed concrete TTD elements manufactured by the concrete element company Spæncom A/S. In Figure 1.2, a plan drawing of the sports floor is shown, and the position of the 9 TTD elements are shown in relation to the floor. Figure 1.3 shows the TTD elements in relation to the two theatre halls underneath the sports hall, and as seen, the TTD elements are exactly above the larger of the theatre halls.

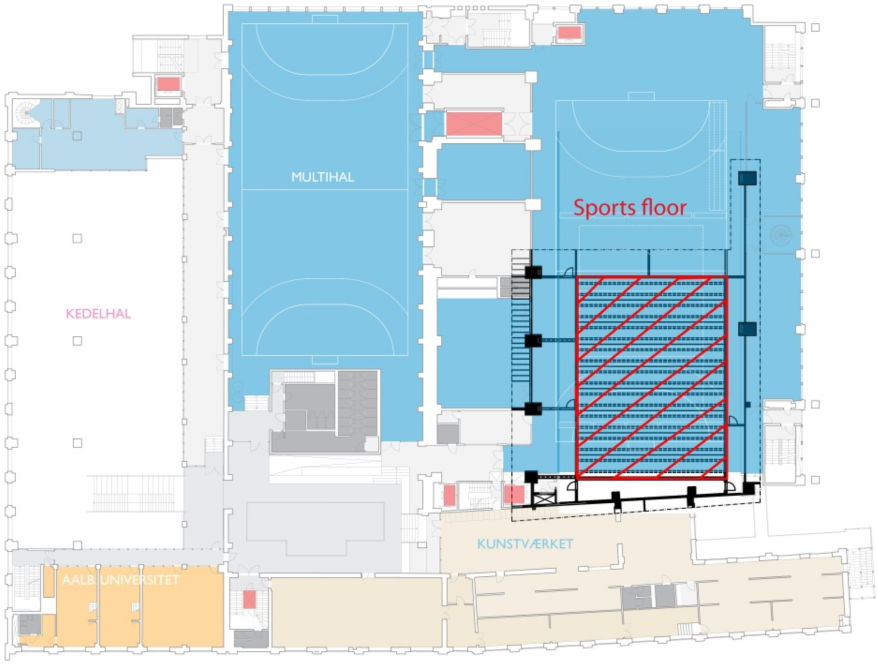

Figure 1.2: Floor plan of level two, TTD elements are marked with a red box [19].

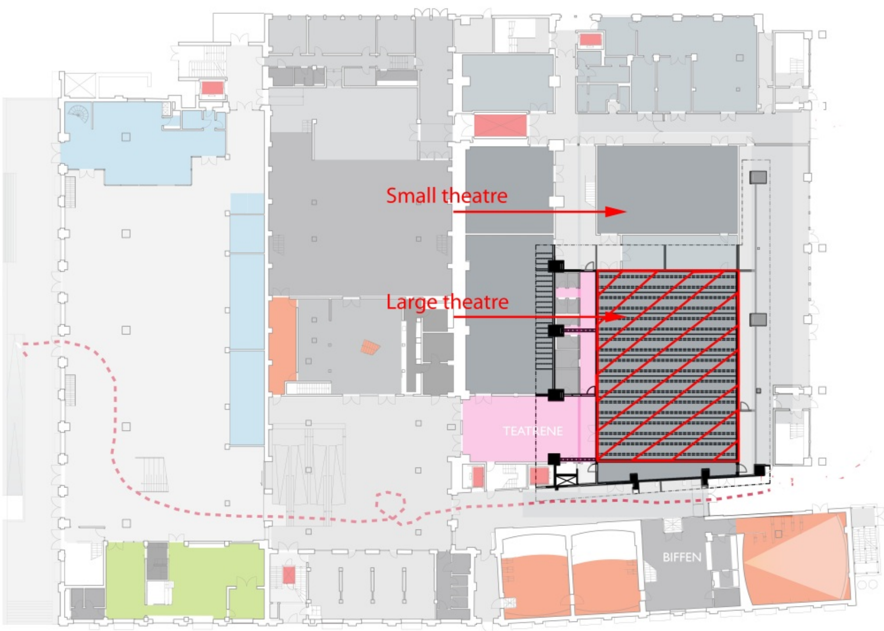

Figure 1.3: Floor plan of level one, TTD elements are are marked with a red box [19].

In Figure 1.4 and Figure 1.5 photos of the sports hall and the main theatre hall are shown. The considered deck is placed in the far end of the sports hall seen from Figure 1.4. As seen in Figure 1.5, lighting equipment is attached to the TTD elements from underneath.

Figure 1.4: Sports hall of DGI-Huset in Nordkraft.

Figure 1.5: Theatre Hall of Teater Nordkraft.

1.1 Technical Properties of TTD element

A short description of the construction will be given. The TTD elements span $L_x = 16.3\,\text{m}$ in the direction of the stiffeners and are supported by the concrete walls of the theatre hall. The length of the deck perpendicular to the stiffeners is $L_y = 21.6\,\text{m}$. A detailed plan of the 9 TTD elements is shown in Figure 1.6, and the specification of four detail drawings, A–D, is shown in the figure. These detail drawings, which are shown in Figure 1.7 and Figure 1.8, illustrate the boundary conditions of the four sides of the deck.

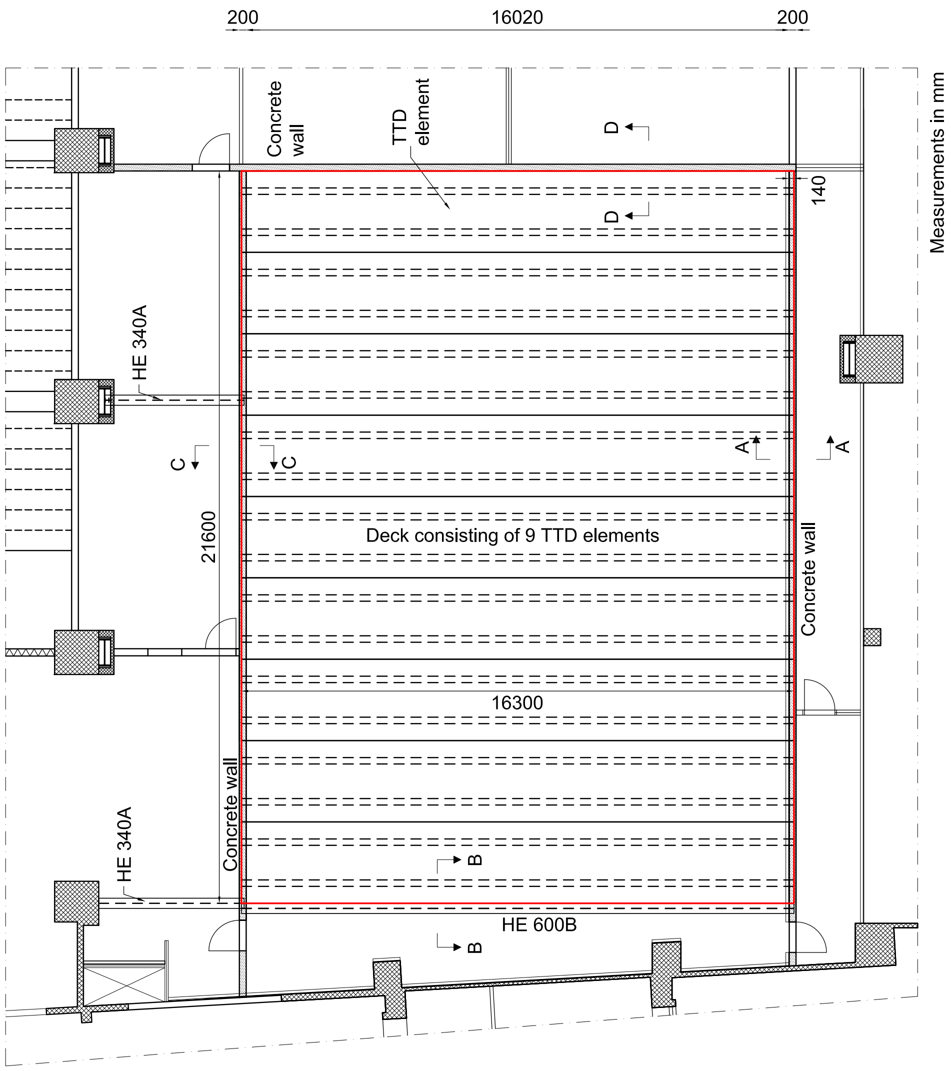

Figure 1.6: Floor plan of TTD elements.

In relation to the shown detail drawings of the floor structure, it should be noticed that concrete topping is cast on top of the TTD elements. Moreover, the interface between the TTD elements and the concrete topping might be considered rough, meaning that shear forces can be transferred from the TTD elements into the layer of the concrete topping. The assumption that the interface is capable of transferring shear forces of a certain level is built on the fact that the TTD elements have visible rebar steel in the top surface for the same purpose. A cross sectional cut of a TTD element can be seen in Figure 1.9. In addition to this, it can be observed that the

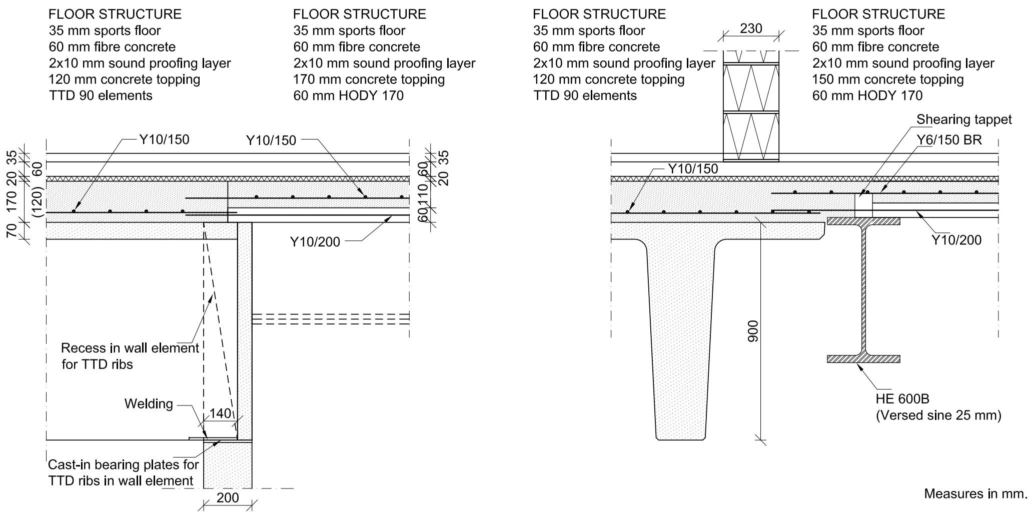

(a) Detail A-A (b) Detail B-B

Figure 1.7: Detail drawings.

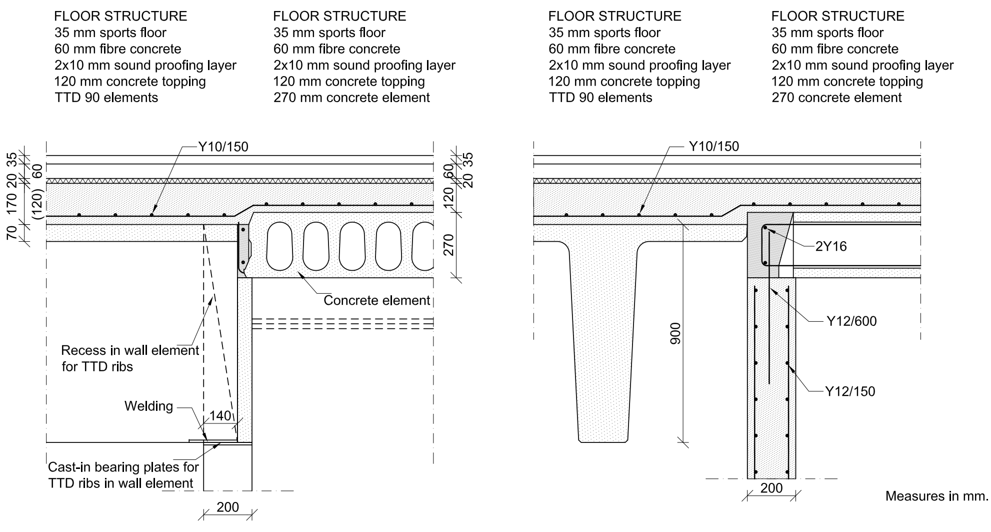

(a) Detail C-C (b) Detail D-D

Figure 1.8: Detail drawings.

concrete topping forms a continuous layer, which connects the TTD elements to the surrounding floor construction. This is the case for all four sides of the plate.

Statically, the TTD elements are connected by the concrete topping, and thereby, the TTD elements and the concrete topping are regarded as rigidly connected. In contrast to this, the sound proofing layer is a rubber-like material, which come in 10 mm mats, and its ability to transfer forces is not certain. Two sound proofing mats are used. Therefore, a calculation model of the floor structure should take into account not only the stiffness and mass of different layers, but also the interface between them.

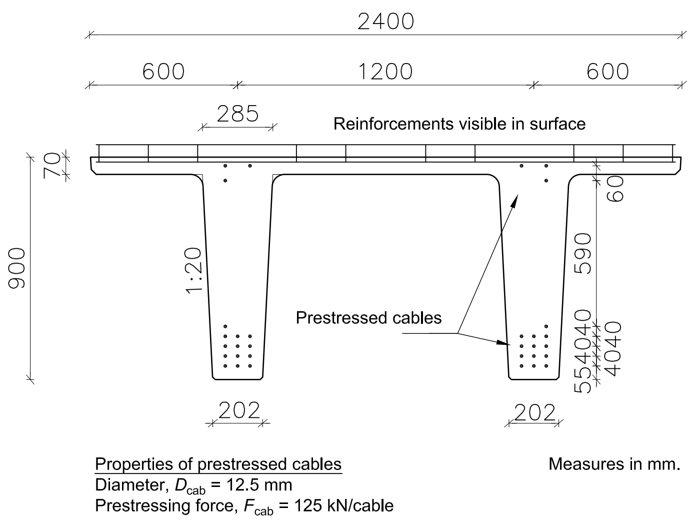

Figure 1.9: TTD cross section [24].

The TTD elements come with a versed sine of approximately 50 mm and are designed to have a minimum of 120 mm concrete topping, which in combination gives the deck an average of approximately 150 mm concrete topping, see Figure 1.7 and Figure 1.8. The sound proofing layer is covered by 60 mm of fibre reinforced concrete, on which the sports floor is placed. The actual sports floor is a flooring solution from Virklund-Sport A/S called Boflex, which consists of a 30 mm wooden construction covered with 4 mm of sports linoleum as seen in Figure 1.10.

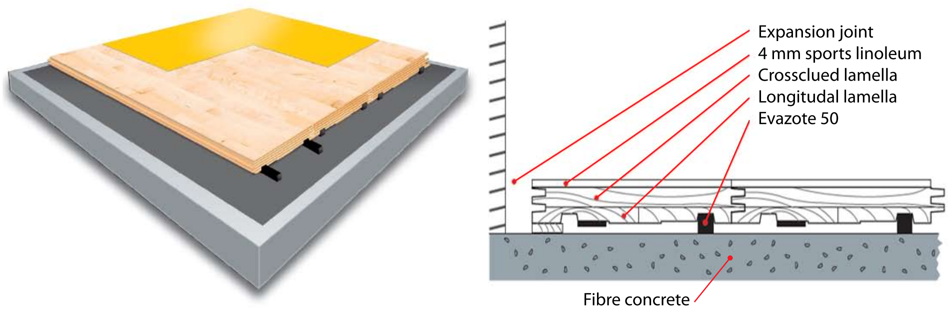

Figure 1.10: Boflex sports floor construction [29].

From this brief description of the deck, it is obvious that assumptions must be made in order to make a mathematical treatment of the deck possible. This is due to the fact that the deck is made up of numerous layers and materials, and the interfaces between the different layers are not fully known with respect to strength and stiffness. Before a more profound technical treatment of the deck is undertaken, the scope of the project must at first be presented and explained.

1.2 Scope and Methods of Project

The scope of the project is to assess the vibrations of the deck, which separates the sports hall and the main theatre hall in Nordkraft with respect realistic load scenarios. The vibrations are assumed to be excited by jumping loads, which represents a critical case of human-induced loads. These kind of vibrations, which are not directly critical with respect to the ultimate limit state (ULS) of the construction, are instead treated as a serviceability limit state (SLS) problem. It should be stressed that original design calculations of the actual deck are known to the authors, where both the ultimate and serviceability limit states are considered. From these it is clear that the ultimate limit state is of no problem, whereas the serviceability limit calculations show that vibrations might reach a level, which is close to unacceptable. This makes the deck in Nordkraft rather interesting as the found vibrational response is relatively sensitive to the chosen calculation model of both structure and load. However, the scope of the project is limited to an investigation of the serviceability for some selected scenarios, and hence a conclusive control of the serviceability limit will not be obtained.

The objective when analyzing the response of a construction with respect to a certain load type is illustrated in a general sense in Figure 1.11, which points out that both the load and construction must be characterized in order to assess the response. In principle, a spectrum shows the energy content at a certain frequency. A general representation of a jumping load can be seen in the upper graph. The main energy is present at the jumping frequency f_p, but energy is also concentrated at frequencies $i f_\mathrm{p}$, where $i = 1, 2, \ldots$. These peaks of the load spectrum are designated load components or load harmonics. If one of the load components hit the maximum of the frequency response spectrum, resonance occurs, and the response of the structure might be dramatically amplified.

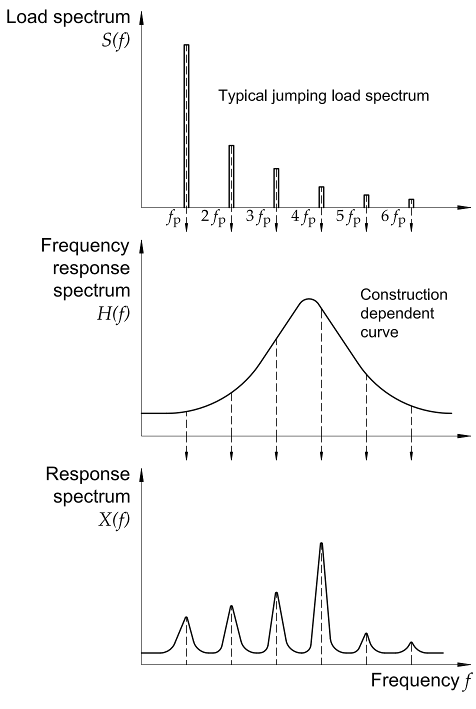

Figure 1.11: Principle in response analysis.

To help the jumper(s) to jump with an exact frequency f_p, music with an overall beat frequency equal to the aimed jumping frequency has been chosen. This procedure was chosen instead of using a signal sound as it is believed that it is easier to keep the pace of a known piece of music. Furthermore, jumping to the sound of music is a more realistic scenario. In relation to this, it is also chosen to focus on jumping frequencies near 2.0 Hz, which is the region of frequencies that is expected to be the most natural ones to keep up the pace with.

The assessment of vibrations in the deck includes numerous phases, and in accordance with Figure 1.11, the vibrational response is dependent on two main conditions, namely the dynamic properties of the construction and the applied load. The first part of the report concerns the determination of essential parameters, which describes the dynamic properties of the construction. Hereafter, the vibrational response of the construction is analyzed with respect to human-induced jumping loads. In case the vibrations are found too severe, examples of remedial measures are finally stated. Figure 1.12 shows the different phases throughout the report and their associated methods and main results. The connection between methods and main results is illustrated with symbols.

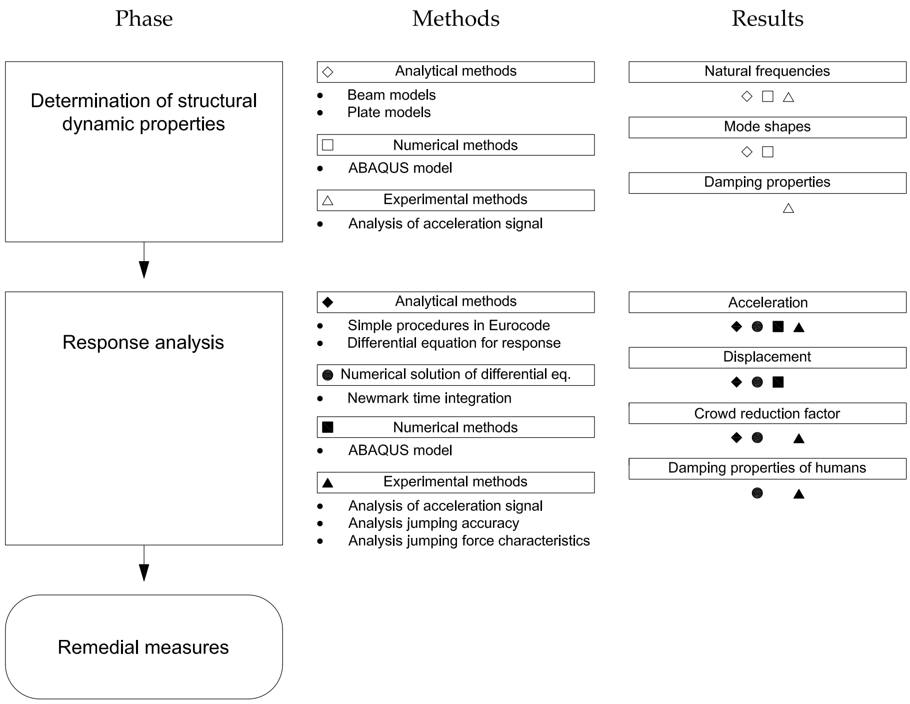

Figure 1.12: Methods, phases, and main results in the project.

Determination of structural dynamic properties includes the following:

- The natural frequencies of the deck are estimated by both analytical and numerical methods. Beam and plate models are used in the analytical approach, whereas the commercial software ABAQUS is used for the numerical treatment. As the deck is a rather complex structure, certain approximations must be made, and the different methods used will be more or less precise. Finally, the natural frequencies are measured experimentally, and the obtained results are compared with the estimated analytical and numerical values. Thereby, assumed parameters in the analytical and numerical methods are updated, so their solutions fit that of the experiment as close as possible.

- In connection with the determination of the natural frequencies, the vibrational mode shapes as well as other modal parameters will also be found as these are highly connected with each other.

- The deck is a physical construction, and when idealized to a vibrating system, it will possess damping in some manner. The amount of damping is important when it comes to the response of the system from human-induced jumping loads. The damping properties will be determined through analysis of a measured acceleration signal on the deck.

When these issues have been treated, the deck should be well-described when it comes to its free vibrations, and furthermore, a calculation framework should be set up, with which the response to jumping loads can be predicted. Two load models will be used as the basis for analyzing the deck in detail. The first load model is described in the Danish National Annex to Eurocode 1 [11], while the second load model is described in an article by Ellis & Ji [8]. Therefore, the next steps will be to excite the structure with load scenarios, which are predominant in the sports hall. As a consequence, the following is done:

- The load models are applied to the analytical and numerical models of the floor and from these, the response of the floor is estimated. The analytical models are here a simple procedure described in Eurocode meant for practical design purposes, and a differential equation solution in modal coordinates. Also, Newmark time integration is used as a way of solving the governing differential equation of motion. As in the first phase, the numerical model is made in ABAQUS. Both the Eurocode load model and Ellis & Ji load model are used in connection with analytical and numerical solution. As numerous different load scenarios are possible in the sports hall, some cases which may be critical will be defined and examined.

- Experiments on the floor in Nordkraft are carried out in order to verify the used calculation models. The same load scenarios as used in the calculation models are applied, where a group of humans participated in the experiments to reassemble a certain load on the floor.

- The experiments serve also to clarify the effect of numerous humans jumping compared to just one human, i.e. it gives an estimate of the so-called crowd reduction factor, which takes into account that total synchronization of humans cannot be achieved. Thus, the jumping load is not proportional with the number of people.

- Likewise, the damping properties of passive humans are also assessed through the experiments. These experimental results are compared to results obtained from the Newmark time integration, where passive humans are modelled as a spring-mass-damper system.

- An additional test series is made in order to analyze the precision with which a human can jump with a given frequency. The results of this experiment are used when considering the crowd reduction factor with a group of jumping humans. Likewise, also one-person jumping tests have been performed to assess the two used load models.

Finally, the results from the analysis of the deck response are summarized and assessed. Especially, in case the vibrational response of the deck are unacceptable, a possible solution to this problem is described.

1.3 Geometrical and Material Parameters

The vibrational behaviour of the deck is very dependent on various geometric and material parameters. Generally, both geometrical and material parameters are treated in a deterministic manner disregarding that some of them could be described by means of a statistical distribution. However, qualified estimates of various parameters are needed in order to achieve reliable results, see Table 1.1. Later, Young's modulus of concrete E_c is updated by use of experiments.

Length of deck parallel to ribs	L_x	16.3 m
Length of deck perpendicular to ribs	L_y	21.6 m
Area of cross section in Figure 1.13	A_{rib}	2.02×10^5 mm^2
Young's modulus of steel	E_s	200 GPa
Young's modulus of concrete (initial guess)	E_c	40 GPa
Poisson's ratio of steel	ν_s	0.3
Poisson's ratio of concrete	ν_c	0.2
Density of reinforced concrete	ρ	2400 kg/m^3

Table 1.1: Geometrical and material parameters of deck.

The moment of inertia I of the deck cross section is calculated in different ways throughout the report, and therefore, a description of how the used value is obtained will be given in connection with the specific calculation. But generally, two different approaches can be followed regarding the steel of the prestressed cables of the TTD elements:

1. Either the stiffness of the steel is taken into account by calculating a "transformed moment of inertia" I_t. Here, the relatively small area of the steel is scaled with a factor $\epsilon = E_s/E_c$ and the transformed moment of inertia is calculated from this new cross section [15]. The transformed moment of inertia should be calculated with respect to the neutral axis of the new cross section, taking into account the scaled areas of the steel. It should be recognized that this modification is somewhat mixing the definitions of Young's modulus E, which is a material parameter, and the moment of inertia I, which is a geometrical parameter. Nevertheless, it can be done to incorporate the larger stiffness of steel compared to concrete.

2. Otherwise, the steel of the prestressed cables can be disregarded in the calculation of the moment of inertia, i.e. the cross sectional area of the cables is regarded as concrete.

The effect of the prestressing force in the cables is disregarded in both cases, and generally, the prestressing force is not treated as a parameter in the calculations throughout the report. A MATLAB-script has been written, which is able to calculate the moment of inertia in both of the two mentioned cases. Likewise, it is also able to handle different heights of the concrete topping, and the axis, about which the moment of inertia is calculated, can be adjusted manually. The script can be found in `Transformed_I.m`, and two examples of its output can be seen in Figure 1.13 and Figure 1.14, where the prestressed cables are excluded and included, respectively. The thickness of the concrete topping is assumed to be 150 mm.

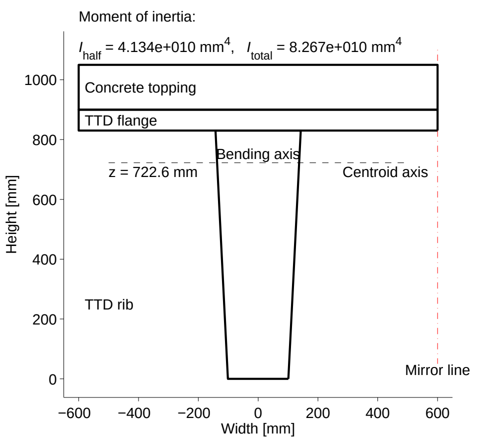

Figure 1.13: Idealized half cross section of TTD element disregarding prestressed cables.

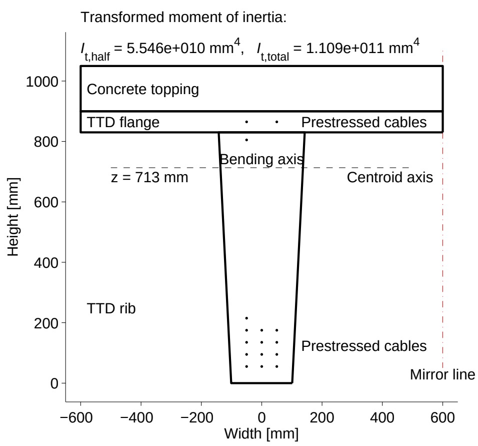

Figure 1.14: Idealized half cross section of TTD element including prestressed cables.

For Young's modulus, both a static and dynamic value exists, and in particular, Young's modulus for concrete is quite uncertain. Therefore, the value of $E_c = 40\,\text{GPa}$ is used initially, and when sufficient experimental data for the deck is found, E_c is updated to fit the specific concrete construction. The other parameters in Table 1.1 are kept at the given value.

The guessed value of $E_c = 40\,\text{GPa}$ can be based on the Danish National Annex to Eurocode 2 [12], where an approximate formula is given to calculate Young's modulus $E_{c,\text{init}}$ for the initial slope on the stress-strain curve, see Eq. (1.1). The characteristic concrete strength is $f_{ck} = 45\,\text{MPa}$.

$$E_{c,\text{init}} = 51000 \cdot \frac{f_{ck}}{f_{ck} + 13} \approx 40 \times 10^3\,\text{MPa} \tag{1.1}$$

1.4 Design Guidelines

When assessing the performance of the floor under human-induced jumping loads, it is necessary to define some boundaries, which states the limit between an acceptable vibration level and an unacceptable vibration level. But as the human perception of vibration is a very subjective matter, such limits are not easy to define. Generally, the level of vibration which is considered acceptable will vary from person to person, and is likely to be dependent on age, gender, the character of the activity, etc. [30].

The matter of human perception of vibrations could be the case of a distinct study, and this will not be treated profoundly here. Nevertheless, to establish some limits for acceptable vibrations of the floor, the rules from the Danish National Annex to Eurocode 0 [10] are adopted, and these are repeated in Table 1.2. As seen, the limits depend on the type of construction and its usage, and therefore in this case, the sports hall in Nordkraft must be placed within the first row. The frequency limits given in Table 1.2 can be assessed after analyzing the structure in free vibrations, whereas the acceleration limit only can be assessed after a more detailed response analysis. The frequency limits are suggested in order to ensure sufficiently high natural frequencies of a structure so that one of the lower load components, i.e. a load component with a relatively high energy content, will not be in resonance.

Construction	Load	Normally satisfactory condition	Often not satisfactory condition	Limit acceleration σ_a or a_{rms}
Grand stands, fitness centres, sports halls, and meeting rooms	Rhythmical human-induced loads	$f > 10\,\text{Hz}$	$f < 6\,\text{Hz}$	10% of g
Residences	Walking load	$f > 8\,\text{Hz}$	$f < 5\,\text{Hz}$	0.1% of g
Offices	Walking load	$f > 8\,\text{Hz}$	$f < 5\,\text{Hz}$	0.2% of g

Table 1.2: Suggested limits for natural frequencies and accelerations [10].

The acceleration limits are given with respect to the so-called standard deviation of the acceleration σ_a, which is equivalent to the so-called root-mean-square acceleration a_{rms} in most English literature. Both measures will be used. It should be noted that a simplified formula for calculating σ_a is stated in Eurocode, which assumes a perfect sinusoidal acceleration signal. Therefore, if the maximum acceleration value in a time series is denoted a_{max}, the standard deviation of the acceleration σ_a can be found as in Eq. (1.2).

$$\sigma_a = \frac{1}{\sqrt{2}} a_{max} \tag{1.2}$$

However, this will always yield a conservative value [10]. The root-mean-square acceleration a_{rms} is calculated as given in Eq. (1.3), where T is the period of time over which the acceleration is measured. $a(t)$ designates an acceleration time series [3].

$$a_{\mathrm{rms}} = \sqrt{\frac{1}{T}\int_0^T a^2(t)\, dt} \tag{1.3}$$

Chapter 2

Analytical Methods

This chapter presents various analytical methods for estimating the natural frequencies of the floor construction. At first, the floor construction is simplified to a beam model, and the frequencies are estimated from this by different approaches. Afterwards, the floor construction is modelled as an orthotropic plate, which is used to estimate the natural frequencies.

✦ ✦ ✦

2.1 Dynamic Analysis of Beam Models

As a quick alternative to analyzing a complex numerical model or plate model of the sports floor, an analytical estimate of the natural frequencies can be performed by means of simple beam models. Here, two different methods are presented. The first method to be considered is based on the solution of the governing differential equation of a vibrating beam. Here the TTD element is assumed to be a Bernoulli-Euler beam with constant mass per unit length $\mu = \rho A_{\text{rib}}$ and constant bending stiffness EI throughout its length. Afterwards, the approximative method of Rayleigh's fraction is used, where an assumed vibration shape of the beam must be guessed in order to obtain results. As touched upon in the introduction, it is not totally obvious how to model the boundary conditions of the floor construction. Hence, for the beam models two extreme cases are examined, namely a simply supported beam, and a beam clamped in both ends. The beam models are based on a rib in the element as shown in Figure 2.1.

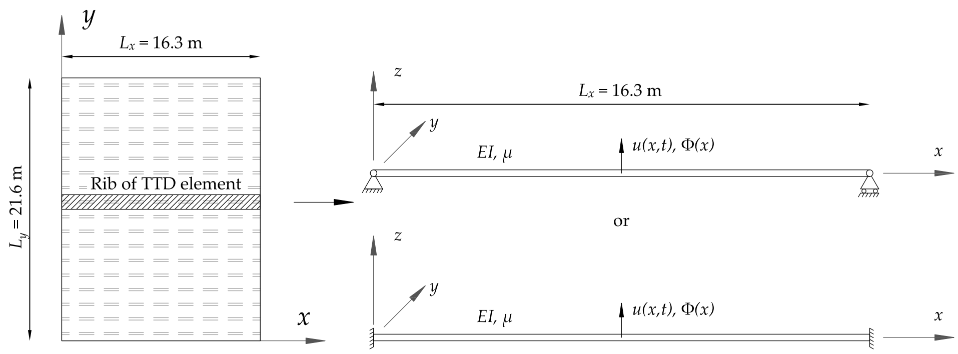

Figure 2.1: Simply supported and clamped beam.

2.1.1 Differential Equation

The governing differential equation of a vibrating Bernoulli-Euler beam is given by Eq. (2.1). No normal force nor exiting force is assumed when formulating the differential equation [17].

$$EI\,\frac{\partial^4 u(x,t)}{\partial x^4} + \mu\,\frac{\partial^2 u(x,t)}{\partial t^2} = 0 \tag{2.1}$$

A solution of Eq. (2.1) is obtained from assuming that each differential mass element $\mu\,dx$ is performing harmonic oscillations in phase. Taking that $\Phi(x)$ is the real amplitude of the differential mass element $\mu\,dx$ and ω is the circular eigenfrequency of the oscillation, a solution to the differential equation is given by Eq. (2.2).

$$u(x,t) = \Phi(x)\cos(\omega t) \tag{2.2}$$

Eq. (2.2) is substituted into the differential equation of Eq. (2.1) and a new differential equation is obtained, see Eq. (2.3). This is also an eigenvalue problem, which is the basis for calculating circular eigenfrequencies ω_m and mode shapes $\Phi_m(x)$ for the m^{th} mode. Along with the differential equation, the relevant boundary conditions for the two considered cases are shown in Eq. (2.3).

$$\left.\begin{array}{l}
\text{Differential equation} \\
\qquad EI\dfrac{d^4\Phi(x)}{dx^4} - \omega^2\mu\Phi(x) = 0 \\[2ex]
\text{Simply supported beam} \\
\qquad \Phi(0) = 0 \qquad \dfrac{d^2\Phi(0)}{dx^2} = 0 \\
\qquad \Phi(L_{\mathrm{x}}) = 0 \qquad \dfrac{d^2\Phi(L_{\mathrm{x}})}{dx^2} = 0 \\[2ex]
\text{Clamped beam in both ends} \\
\qquad \Phi(0) = 0 \qquad \dfrac{d\Phi(0)}{dx} = 0 \\
\qquad \Phi(L_{\mathrm{x}}) = 0 \qquad \dfrac{d\Phi(L_{\mathrm{x}})}{dx} = 0
\end{array}\right\} \tag{2.3}$$

The general solution for the differential equation of Eq. (2.3) is stated in two different ways for the simply supported beam and the clamped beam, respectively [17, 27]. The general solution for the differential equation in case of a simply supported beam is given by Eq. (2.4a), while the general solution for the clamped beam case is stated in a slightly different way in Eq. (2.4b).

$$\Phi(x) = A\sin\left(\lambda\frac{x}{L_{\mathrm{x}}}\right) + B\cos\left(\lambda\frac{x}{L_{\mathrm{x}}}\right) + C\sinh\left(\lambda\frac{x}{L_{\mathrm{x}}}\right) + D\cosh\left(\lambda\frac{x}{L_{\mathrm{x}}}\right) \tag{2.4a}$$

$$\begin{aligned}
\Phi(x) = A&\left(\cos\left(\lambda\frac{x}{L_{\mathrm{x}}}\right) + \cosh\left(\lambda\frac{x}{L_{\mathrm{x}}}\right)\right) + B\left(\cos\left(\lambda\frac{x}{L_{\mathrm{x}}}\right) - \cosh\left(\lambda\frac{x}{L_{\mathrm{x}}}\right)\right)\dots \\
&+ C\left(\sin\left(\lambda\frac{x}{L_{\mathrm{x}}}\right) + \sinh\left(\lambda\frac{x}{L_{\mathrm{x}}}\right)\right) + D\left(\sin\left(\lambda\frac{x}{L_{\mathrm{x}}}\right) - \sinh\left(\lambda\frac{x}{L_{\mathrm{x}}}\right)\right)
\end{aligned} \tag{2.4b}$$

where $\lambda^4 = \dfrac{\mu\omega^2 L_{\mathrm{x}}^4}{EI}$

When using the boundary conditions for a simply supported beam together with Eq. (2.4a) a frequency condition can be found from which the circular eigenfrequencies and mode shapes can be found. This classical solution is not shown here, but can be seen in [17]. The circular eigenfrequencies and the corresponding mode shapes can be found from Eq. (2.5).

$$\omega_m = m^2\pi^2\sqrt{\frac{EI}{\mu L_x^4}}$$
$$\Phi_{m,\mathrm{Simp}}(x) = A_m \sin\left(m\pi\frac{x}{L_x}\right) \tag{2.5}$$

Eigenvalues obtained by Eq. (2.5) are presented later after the presentation of other approaches, whereas the three first mode shapes of a simply supported beam can be seen in Figure 2.2. As seen from the shapes of the curves, these mode shapes satisfy the boundary conditions of a simply supported beam.

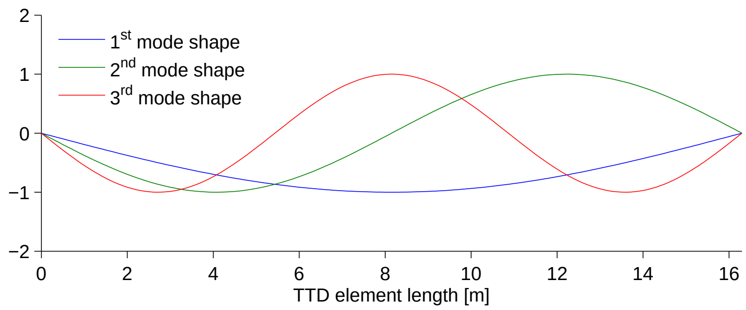

Figure 2.2: Three first mode shapes of a simply supported beam.

To solve the problem of a beam with two clamped ends, the boundary conditions for a clamped beam stated in Eq. (2.3) are used together with the general solution, Eq. (2.4b). The boundary conditions at $x = 0$ yield that $A = C = 0$. From this, using the boundary conditions at $x = L_x$, the following system of equations is obtained, Eq. (2.6). Index m is implicitly assumed.

$$\mathbf{K}(\lambda(\omega))\begin{bmatrix} B \\ D \end{bmatrix} = \begin{bmatrix} 0 \\ 0 \end{bmatrix} \quad \Leftrightarrow \quad \begin{bmatrix} \cos(\lambda) - \cosh(\lambda) & \sin(\lambda) - \sinh(\lambda) \\ \sin(\lambda) + \sinh(\lambda) & -\cos(\lambda) + \cosh(\lambda) \end{bmatrix}\begin{bmatrix} B \\ D \end{bmatrix} = \begin{bmatrix} 0 \\ 0 \end{bmatrix} \tag{2.6}$$

To obtain other than the trivial solution, the following frequency condition must be solved: $\det(\mathbf{K}(\lambda(\omega))) = 0$. This yields the following equation, Eq. (2.7).

$$\cos(\lambda)\cosh(\lambda) = 1 \tag{2.7}$$

The determination of roots λ_m from Eq. (2.7) is not straightforward, and as a consequence a Newton-Raphson iterative solution of the equation is used. The calculations can be found in both `Analytical_frequency_of_beam_model.xmcd` and `Roots_NR.m`. The three first roots of Eq. (2.7) are given below:

λ_1	λ_2	λ_3
4.7300	7.8532	10.9956

The circular eigenfrequencies are implicitly given by these roots, and the exact values can be obtained by use of the definition of λ in Eq. (2.4b). To obtain the mode shapes, the roots λ_m are used in Eq. (2.6) to obtain the values of B_m and D_m. Either B_m or D_m must be arbitrarily chosen, and therefore it is rather the ratio B_m/D_m which is found. Hereafter, the values of λ_m, B_m, and

D_m are substituted into the general solution of Eq. (2.4b), see Eq. (2.8).

$$\lambda_m^4 = \frac{\mu \omega_m^2 L_x^4}{EI} \quad \Leftrightarrow \quad \omega_m = \sqrt{\frac{\lambda_m^4 EI}{\mu L_x^4}}$$

$$\Phi_{m,\text{Clamp}}(x) = B\left(\cos\left(\lambda_m \frac{x}{L_x}\right) - \cosh\left(\lambda_m \frac{x}{L_x}\right)\right)\dots \\ + D\left(\sin\left(\lambda_m \frac{x}{L_x}\right) - \sinh\left(\lambda_m \frac{x}{L_x}\right)\right) \tag{2.8}$$

The results for the circular eigenfrequencies are given later, whereas the three first mode shapes are depicted in Figure 2.3. The zero slope of all curves at each of the supports should be noted, as it satisfies the boundary conditions.

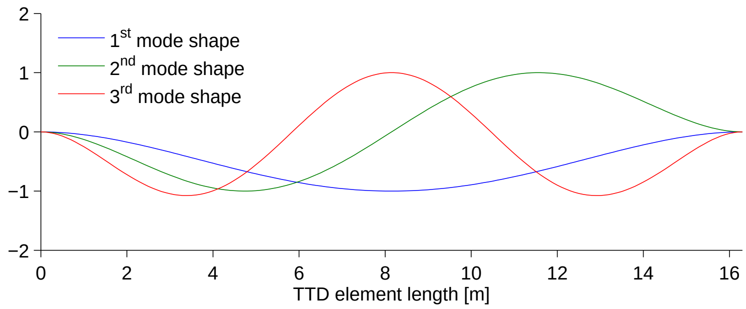

Figure 2.3: Three first mode shapes of a beam fixed in both ends.

2.1.2 Rayleigh's Fraction

An estimate of a specific natural frequency for both beam cases can be found by the use of Rayleigh's fraction. This method estimates the natural frequency from a given approximated mode shape $\Phi_{\text{app}}(x)$, which makes the accuracy of the estimate highly dependent on the chosen mode shape. The method is based on analyzing the ratio between the maximum potential energy (strain energy) and the maximum kinetic energy of the system. The estimate on the natural frequency can be found from Eq. (2.9), where $U_{\max}$ is the maximum potential energy and $T_{\max}$ is the kinetic energy during one period of vibration. The theoretical background of Rayleigh's fraction is more profoundly treated in Appendix A.

$$\left.\begin{aligned} U_{\max} &= \frac{1}{2}\int_{L_x} EI\left(\frac{d^2\Phi_{\text{app}}(x)}{dx^2}\right)^2 dx \\ T_{\max} &= \frac{1}{2}\omega^2\int_{L_x} \mu\left(\Phi_{\text{app}}(x)\right)^2 dx \end{aligned}\right\} \quad \omega^2 = \frac{\int_{L_x} EI\left(\frac{d^2\Phi_{\text{app}}(x)}{dx^2}\right)^2 dx}{\int_{L_x} \mu\left(\Phi_{\text{app}}(x)\right)^2 dx} \tag{2.9}$$

When the properties of the beam are given, i.e. length L_x, Young's modulus E, moment of inertia I, and the mass per unit length μ, only an approximated shape of the first vibration mode $\Phi_{\text{app}}(x)$ must be given. The only requirement to the approximated shape $\Phi_{\text{app}}(x)$ is that it fulfils the geometric boundary conditions [4].

For the simply supported beam and the beam with two ends clamped, the used approximative shapes are given by Eq. (2.10a) and Eq. (2.10b), respectively. For the simply supported beam, Eq. (2.10a) is actually the exact vibrational shape, and therefore, Rayleigh's fraction is also expected to yield the exact solution. Regarding the approximated shape for the clamped beam case, Eq. (2.10b), it should be noted that the expression is defined within the boundaries from $-\frac{1}{2}L_\mathrm{x}$ to $\frac{1}{2}L_\mathrm{x}$ instead of 0 to L_x as for the simply supported case.

$$\Phi_{\mathrm{app,Simp}}(x) = \sin\left(\pi \frac{x}{L_\mathrm{x}}\right) \tag{2.10a}$$

$$\Phi_{\mathrm{app,Clamp}}(x) = \left(1 - 4\frac{x}{L_\mathrm{x}}\right)^2 \tag{2.10b}$$

The mode shape of a clamped beam can be described by Eq. (2.10b) for the first bending mode and is illustrated in Figure 2.4, where it for the sake of completeness is plotted together with the exact mode shape for the beam with two clamped ends. The constants B_m and D_m in the expression of the exact mode shape are modified so the mid-beam deflection is the same for the exact and approximated shape. Thus, comparing the two shapes, Eq. (2.10b) seems to be a good approximation to the exact shape, Eq. (2.8), and therefore a close estimate of the circular eigenfrequency can be found.

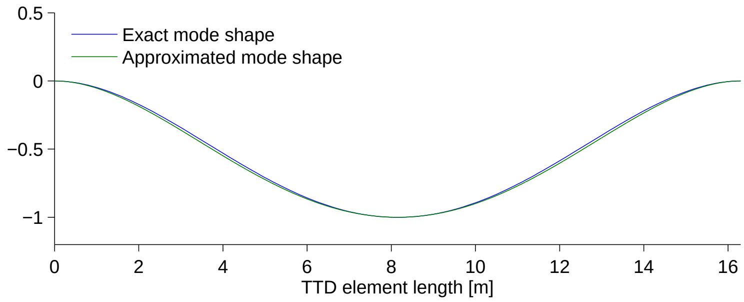

Figure 2.4: Comparison of approximated and exact shape.

In the calculations a dynamic Young's modulus of 40 GPa is used. The moment of inertia is calculated for the pure geometry of the TTD element with 150 mm of concrete topping and no corrections done to account for the prestressed cables. On these premises the moment of inertia becomes $I = 4.134 \times 10^{10}\,\mathrm{mm}^4$, see Figure 1.13. The exact length of the beam is set to $L_\mathrm{x} = 16.3\,\mathrm{m}$. With these parameters the frequency estimates can be calculated and the results can be seen in Table 2.1. The calculations can be found in the MATHCAD document `Analytical_frequency_of_beam.xmcd`. The relationship $f = \omega/2\pi$ has been utilized in Table 2.1.

f_m [Hz]	m	Simple	Clamped
	1	7.19	16.29
Analytical solutions	2	28.75	44.92
	3	64.69	88.05
Rayleigh's fraction	1	7.19	16.35

Table 2.1: Estimated natural frequencies of the TTD element.

By comparison of the values, it is seen that the estimated frequencies obtained by Rayleigh's fraction is quite close to those of the exact analytical solution. The exact eigenfrequency is found for the simply supported case as the exact mode shape has been used, and for the clamped case, the estimate of Rayleigh's fraction is slightly higher.

2.1.3 Frequency Drop due to Additional Mass

The frequency estimates done in the previous section only takes into account the mass of the TTD element and the concrete topping. The actual deck has additional 20 mm sound proofing rubber mats on which 60 mm fibre concrete is placed. On top of the fibre concrete the actual sports floor construction, Boflex, is installed. These layers naturally adds mass to the construction and will hence alter the dynamics of the system estimated previously. As the connection between concrete topping, sound proofing mats, and fibre concrete is not fully know, it is in the following assumed that the layers add mass but no stiffness to the dynamic system. The additional three layers are simplified to one 80 mm thick layer with an average mass equal to concrete.

Describing the TTD element and concrete topping as a dynamic system with modal parameters m and k, the expression for the angular eigenfrequency is given by [17]:

$$\omega = \sqrt{\frac{k}{m}} \qquad \text{where} \qquad \begin{cases} m = \int_{L_x} \mu \Phi(x)^2 dx \\ k = \int_{L_x} EI \left(\frac{d^2}{dx^2} \Phi(x) \right)^2 dx \end{cases} \tag{2.11}$$

The change in eigenfrequency, when adding a rigid mass attachment of mass Δm, can be shown with the following expressions, Eq. (2.12). Δm is determined as in Eq.(2.11), but with a mass per unit length μ_{add}, which corresponds to the mass of the additional layers.

$$\left. \begin{aligned} \omega &= \sqrt{\frac{k}{m}} && \Rightarrow \quad k = \omega^2 m \\ \omega_{\text{new}} &= \sqrt{\frac{k}{m + \Delta m}} && \Rightarrow \quad k = \omega_{\text{new}}^2 (m + \Delta m) \end{aligned} \right\} \quad \begin{aligned} \omega^2 m &= \omega_{\text{new}}^2 (m + \Delta m) \quad \Rightarrow \\ \omega_{\text{new}} &= \omega \sqrt{\frac{m}{m + \Delta m}} \quad \Rightarrow \\ f_{\text{new}} &= f \sqrt{\frac{1}{1 + \frac{\Delta m}{m}}} \end{aligned} \tag{2.12}$$

Eq. (2.12) can be used to account for the mass of the additional layers by calculating the modal masses. The modal masses are dependent on the mode shape and hence varies if the beam is assumed simply supported or clamped in both ends. The modal masses and reduction in natural frequency are carried out in the MATHCAD-document `Analytical_frequency_of_beam_model.xmcd` and the results can be seen in Table 2.2. The reduction factor is in every case calculated to be $\sqrt{1/\left(1 + \frac{\Delta m}{m}\right)} = 0.92$.

f_m [Hz]	m	Simple	Clamped
Differential equation	1	6.62	15.01
	2	26.48	41.37
	3	59.59	81.10
Rayleigh's fraction	1	6.62	15.06

Table 2.2: Reduced natural frequencies when accounting for added mass of top layers.

From the analytical frequency estimates assuming the deck to follow a beam model, it can be seen that the simply supported model predicts a natural frequency where caution should be taken as the low frequency might be excited by load components of human jumping loads. The natural frequencies for the simply supported beam models are lower than the suggested limits defined in Table 1.2. It should also be noted that the boundary conditions, simple or clamped, have severe effects on the estimated frequency, and it could be argued that depending on the construction, both cases should be calculated and used as limit cases as the actual frequency in reality will take on a value in between.

2.2 Dynamic Analysis of Plate Models

The natural frequencies of the deck can be determined using different approaches. An analogy to a plate model seems relevant due to the size and shape of the deck. The TTD element structure exhibits some of the characteristics of a plate, namely, two dimensions of the structure are considerable larger than the latter. Furthermore, due to the concrete topping, the deck can be considered as a continuous structure as the concrete topping connects all of the nine TTD elements. Nevertheless, there are some obvious problems in adopting a plate model as the basis for determining the natural frequencies. First of all, the two ribs of each TTD element makes the bending stiffness of the structure considerably larger in one direction compared to the perpendicular direction. Secondly, the deck is made of two materials: concrete and steel, where steel is found both in form of rebar in the concrete topping and prestressed cables in the TTD elements. These two facts complicate the formulation of a useful plate model for the determination of natural frequencies.

The different bending stiffnesses in two perpendicular directions makes the model of an isotropic plate insufficient, i.e. a plate model with the same stiffness in all directions. Instead, an orthotropic plate model is adopted. Here, it is important to point out that orthotropy can be understood in two different ways. First, natural orthotropy is the case where the material itself has an orthotropic structure as for example tree, where the stiffness in the direction of the fibres is larger than in the cross-fibre direction. Secondly, when the geometric shape of the structure or a mix of materials is the source of the orthotropic behaviour, the structure is designated structural orthotropic. From these definitions it is clear that the deck falls within the second category as the rib stiffeners of the deck increase the bending stiffness in only one direction [28]. The overall dimensions of the plate problem are illustrated in Figure 2.5.

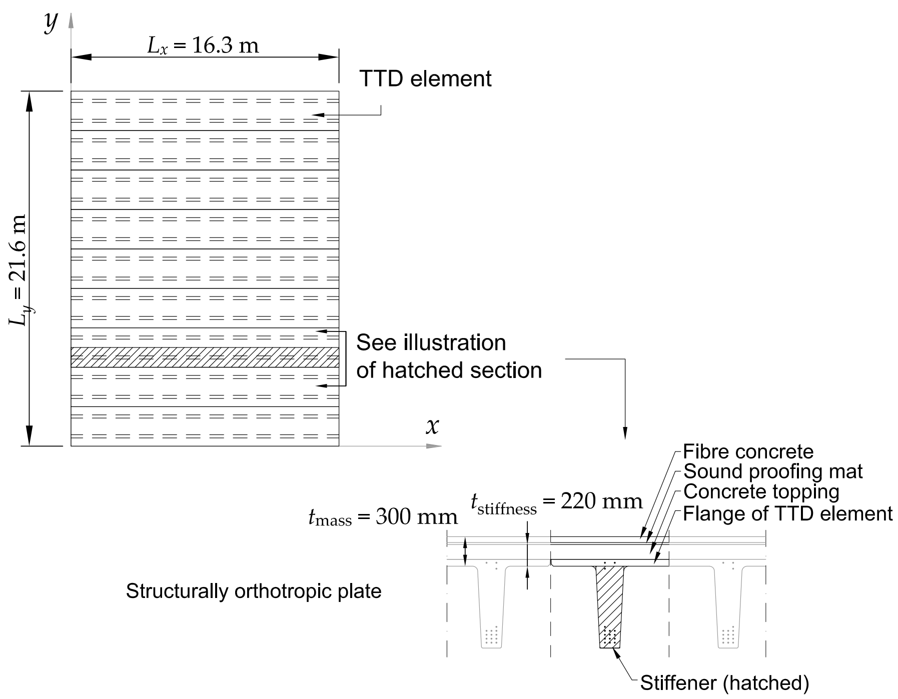

Figure 2.5: Overview of analytical plate problem.

Generally, orthotropic plate models apply for plates of natural orthotropy, while approximations have to be made for plates of structural orthotropy. In the following section it will be described, how the deck is modelled by various orthotropic plate models as well as the approximations connected with them. Finally, the natural frequencies are found using the different approaches. Generally, two different methods are used:

- Estimates of the natural frequencies are found using the governing differential equation of motion of an orthotropic plate. This equation is of 4^{th} order and a specific solution might be obtained by use of sine-series, which satisfy the boundary conditions of a simply supported plate. Therefore, assuming a sine-series solution, this approach is limited to plates, which are simply supported on all four edges [28].

- Energy methods can be used to estimate the natural frequencies of a structure. In this case, both Rayleigh's fraction and the Rayleigh-Ritz method have been utilized. Expressions for the potential energy U and kinetic energy T of the structure are formulated by use of approximate shape functions satisfying the boundary conditions. From this, estimates of the natural frequencies are calculated from a minimization procedure, see Appendix A.

It should be noted that the stiffnesses, which are calculated in the coming sections, are designated with respect to the primary direction of the normal strains, which accompany bending. E.g. the flexural stiffness D_{x} is used when bending occurs around an axis parallel to the y-axis, and the normal strains develop in the x-direction.

As seen in Figure 2.5, the deck can be divided into two main parts. A plate with uniform thickness and some equally spaced rib stiffeners, which together may be designated a structurally orthotropic plate. The plate with uniform thickness consists of: the flange of the TTD element, concrete topping, a sound proofing mat, and a fibre concrete layer. The very top layer, the sports floor, is not considered at all in the following calculations due to its relative low weight and stiffness. Two different thickness measures of the plate are used. When calculations regarding the stiffness of the plate are made, only the combined thickness of the flange and concrete topping is used. However, when calculations regarding the mass are made, the total thickness of flange, concrete topping, sound proofing mat, and fibre concrete is used. This distinction is made as the sound proofing mat is considered very flexible with respect to vibrations.

2.2.1 Differential Equation of Motion

The governing differential equation of motion of an orthotropic plate is given by Eq. (2.13). Here, only the homogeneous part has been shown as free vibrations are studied. The differential equation has been formulated in such a way that it takes the effect of the rotating inertia of the stiffeners J_{x} and J_{y} into account [28].

The inclusion of the rotating inertia or the mass moment of inertia of the stiffeners is important as the rib stiffeners have a mass, where energy should be used in order to put these into motion. Therefore, the mass moment of inertias enter together with the mass of the uniform plate.

$$D_{\text{x}} \frac{\partial^4 u}{\partial x^4} + 2H \frac{\partial^4 u}{\partial x^2 \partial y^2} + D_{\text{y}} \frac{\partial^4 u}{\partial y^4} + \frac{\partial^2}{\partial \tau^2} \left(\rho t u - J_{\text{x}} \frac{\partial^2 u}{\partial x^2} - J_{\text{y}} \frac{\partial^2 u}{\partial y^2} \right) = 0 \tag{2.13}$$

where

u	Lateral deflection of plate with respect to in-plane coordinates $u(x, y)$.
D_x	Flexural stiffness in the x-direction.
D_y	Flexural stiffness in the y-direction, $D_y = D = Et^3/(12(1-\nu^2))$.
H	Effective torsional stiffness, $H = \nu D + 2D_{xy}$, definition of D_{xy} is seen in Eq. (B.2) in Appendix B.
J_x	Mass moment of inertia per unit area, in x-direction.
J_y	Mass moment of inertia per unit area, in y-direction.
ρ	Density of material.
t	Thickness of uniform thick plate disregarding stiffeners.
τ	Time.

It is obvious that the plate rigidity parameters: D_x, D_y, and H must be determined in a way that takes the structural orthotropy of the deck into account. Furthermore, in the determination of the plate rigidities it is important to recognize that the stiffeners of the uniform plate have an eccentric position with respect to the mid-plane of the plate, where normal strains develop in the mid-plane of the uniform plate. The determination of the plate rigidities is treated in Appendix B using an approach suggested by Iyengar [14]. Likewise, the determination of the mass moment of inertias, J_x and J_y, is treated in Appendix B.

One solution of the homogeneous differential equation, Eq. (2.13), is given by Eq. (2.14). Due to the sine-terms, the lateral deflection $u(x, y)$ will always be zero at the boundaries as will the curvature. Therefore, Eq. (2.14) satisfies only simply supported boundary conditions.

$$u(x, y, \tau) = \sum\sum \sin\left(m\pi\frac{x}{L_x}\right)\sin\left(n\pi\frac{y}{L_y}\right)\sin(\omega_{mn}\tau) \tag{2.14}$$

where

ω_{mn}	Natural circular frequency of plate.
m	Number of half-sine mode in x-direction.
n	Number of half-sine mode in y-direction.
L_x	Width of plate parallel to stiffeners.
L_y	Length of plate perpendicular to stiffeners.

The suggested solution, Eq. (2.14), is substituted into the differential equation, Eq. (2.13), and after some mathematical manipulations, which are not treated here, an expression for the natural circular frequency is given by Eq. (2.15).

$$\omega_{mn}^2 = \pi^4 \frac{D_x\left(\frac{m}{L_x}\right)^4 + 2H\left(\frac{mn}{L_xL_y}\right)^2 + D_y\left(\frac{n}{L_y}\right)^4}{\rho t + \pi^2\left(J_x\left(\frac{m}{L_x}\right)^2 + J_y\left(\frac{n}{L_y}\right)^2\right)} \tag{2.15}$$

The results obtained from Eq. (2.15) are presented in Section 2.2.4 together with results from other approaches. The calculation can be found in `Analytical_frequency_of_plate_model.xmcd`.

2.2.2 Rayleigh's Method

One of the energy methods which has been used to estimate the natural frequency of the structure is based on an article of Dickinson [6]. Rayleigh's method is used, but unfortunately, the approximated functions defining the shape of the vibrating plate is not stated in the article, and it has not been possible to find the source, where the functions are defined. Nevertheless, the method has been applied due to its simplicity.

The natural circular frequency ω of the plate is found from Eq. (2.16). The designations "simple-simple" and "clamped-clamped" refer to the boundary conditions of two sides opposite each other.

$$\frac{\rho t \omega^2 L_\mathrm{x}^2 L_\mathrm{y}^2}{\pi^4 H} = \frac{D_\mathrm{x}}{H}\Gamma_\mathrm{x}^4 \frac{L_\mathrm{y}^2}{L_\mathrm{x}^2} + \frac{D_\mathrm{y}}{H}\Gamma_\mathrm{y}^4 \frac{L_\mathrm{x}^2}{L_\mathrm{y}^2} + 2\left[\Lambda_\mathrm{x}\Lambda_\mathrm{y} + 2\frac{D_\mathrm{xy}}{H}\left(\Psi_\mathrm{x}\Psi_\mathrm{y} - \Lambda_\mathrm{x}\Lambda_\mathrm{y}\right)\right] \tag{2.16}$$

Coefficients in Eq. (2.16). α takes the value of x and y respectively, and p is the number of nodal lines including supported edges perpendicular to direction α [6].

	p	Γ_α	Λ_α	Ψ_α
Simple-simple	2,3,4	$p-1$	$(p-1)^2$	$(p-1)^2$
Clamped-clamped	2	1.506	1.248	1.248

The plate rigidities used in the formula are calculated in Appendix B for two different values of the second moment of area of the stiffeners. Results are summarized in Section 2.2.4, and the calculations can be found in `Analytical_frequency_of_plate_model.xmcd`.

Rayleigh's method will yield frequencies that can be expected to be higher than the exact ones. If the chosen shape function is not the correct one, additional constraints are applied to the model, and these will increase the rigidity in the system. To minimize the added rigidity, Ritz proposed to superpose a number of assumed shape functions, and then find a minimum of this function by differentiation with regard to the amplitudes of the assumed functions. The shape is defined by the function $\Phi(x, y)$, which is used in the time varying function, Eq. (2.17).

$$u(x, y, \tau) = \Phi(x, y)\cos(\omega\tau) \tag{2.17}$$

The shape function used for Ritz's solution is, when assuming a sine shape of deflection, actually a summation of the shape functions which are used in Rayleigh's solution. The number of summed functions limits the number of frequencies which can be computed. The shape functions used for the two methods are shown for a simply supported plate in Eq. (2.18a) and Eq. (2.18b).

$$\text{Rayleigh:} \qquad \Phi_{mn}(x, y) = \sin\left(m\pi\frac{x}{L_\mathrm{x}}\right)\sin\left(n\pi\frac{y}{L_\mathrm{y}}\right) \tag{2.18a}$$

$$\text{Rayleigh-Ritz:} \qquad \Phi(x, y) = \sum_m\sum_n A_{mn}\sin\left(m\pi\frac{x}{L_\mathrm{x}}\right)\sin\left(n\pi\frac{y}{L_\mathrm{y}}\right) \tag{2.18b}$$

For comparison with Eq. (2.16), a Rayleigh solution has been derived specifically for the floor. The solution is described in further details in Appendix A, and the solution, when Eq. (2.18a) is assumed as shape function, is presented in Eq. (2.19).

$$\omega_{mn} = \frac{\pi^2}{L_\mathrm{x}^2}\sqrt{\frac{\dfrac{D}{2L_\mathrm{y}^3}\left(n^2L_\mathrm{x}^2 + m^2L_\mathrm{y}^2\right)^2 + m^4 EI\sum_i \sin^2\left(n\pi\dfrac{y_i}{L_\mathrm{y}}\right)}{\dfrac{1}{2}\rho t L_\mathrm{y} + \rho A\sum_i \sin^2\left(n\pi\dfrac{y_i}{L_\mathrm{y}}\right)}} \tag{2.19}$$

where

- D Uniform flexural stiffness of plate.
- EI Bending stiffness of a stiffener.
- y_i Distance to stiffener number i along the y-axis.

The natural frequencies can be calculated as stated in Eq. (2.19) with the MATLAB script `Rayleigh_Floor.m`.

2.2.3 Rayleigh-Ritz' Method

The Rayleigh-Ritz solutions described in [28] are used for two different cases of boundary conditions: the plate is simply supported on all four edges, and the plate is clamped on all four edges.

When assuming four simply supported edges, the expression given in Eq. (2.18b) is used as it satisfies the boundary conditions on all edges. It is used in Eq. (2.17) and the potential energy U and kinetic energy T is formulated, after which the procedure described in Appendix A is imposed. This leads to the following frequency condition given in Eq. (2.20).

$$\omega^2 = \frac{EI\pi^4}{L_x^3 M_s} \cdot \frac{m^4 + \dfrac{\Delta}{(s+1)\beta^3}(m^2\beta^2 + n^2)^2}{1 + \dfrac{M_p}{(s+1)M_s}} \tag{2.20}$$

where

M_s	Masses of stiffeners.
M_p	Mass of plate.
I	Second moment of area of stiffener, see Appendix B.
Δ	Non dimensional stiffness parameter, $\Delta = \frac{L_x D}{EI}$.
s	Number of stiffeners.
β	Length to width ratio, $\beta = \frac{L_y}{L_x}$.

When assuming four clamped edges, another function describing the shape of the plate during vibration must be used. In accordance with [28], the expression given in Eq. (2.21) is used.

$$\Phi(x,y) = A_{11}\left(1 - \cos\left(2\pi\frac{x}{L_x}\right)\right)\left(1 - \cos\left(2\pi\frac{y}{L_y}\right)\right) \tag{2.21}$$

As before, Eq. (2.21) is used in Eq. (2.17), and the Rayleigh-Ritz procedure is applied. This leads to the frequency condition given in Eq. (2.22).

$$\omega^2 = \frac{16\pi^4 EI}{3M_s L_x^3} \cdot \frac{1 + \dfrac{\Delta}{3(s+1)}\left(3\beta^{-3} + 2\beta^{-2} + \dfrac{3}{\beta^{-1}}\right)}{1 + \dfrac{M_p}{(s+1)M_s}} \tag{2.22}$$

The natural frequencies obtained by Eq. (2.20) and Eq. (2.22) are shown in Section 2.2.4. The calculations can be found in the file `Analytical_frequency_of_plate_model.xmcd`.

2.2.4 Results

The obtained natural frequencies assuming different boundary conditions are presented in this section. Generally, two different moment of inertia of the stiffeners have been used in the calculations – one taking into account the stiffness of the prestressed cables and the other disregarding it as described in Appendix B. Therefore, for different boundary conditions, two cases of estimated natural frequencies exist. In Table 2.3, the results of the preceding formulas are shown. The angular frequency ω has been used to calculate the frequency f by the relation $f = \omega/2\pi$.

In the first method, the differential equation of a vibrating orthotropic plate has been used, which require determination of orthotropic plate rigidities. Secondly, the energy methods have been used in various forms, which also require the choice of appropriate shape functions for the considered vibration mode as well as boundary conditions.

f_{11} [Hz]	CASE 1 $I = 4.079 \times 10^{10}\,\mathrm{mm}^4$ $EI = 1.63 \times 10^9\,\mathrm{Nm}^2$	CASE 2 $I = 2.779 \times 10^{10}\,\mathrm{mm}^4$ $EI = 1.11 \times 10^9\,\mathrm{Nm}^2$
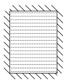 *Simply supported on four sides*		
Differential Equation, Eq. (2.15)	7.24	6.10
Rayleigh's fraction – Dickinson, Eq. (2.16)	6.46	5.45
Rayleigh's fraction – Authors, Eq. (2.19)	6.72	5.62
Rayleigh-Ritz, Eq. (2.20)	6.82	5.71
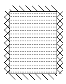 *Clamped on edges perpendicular to stiffeners, simply supported on edges parallel to stiffeners*		
Rayleigh's fraction – Dickinson, Eq. (2.16)	12.56	10.52
 *Clamped on four sides*		
Rayleigh's fraction – Dickinson, Eq. (2.16)	12.81	10.76
Rayleigh-Ritz, Eq. (2.22)	15.61	13.01

Table 2.3: First natural frequency.

The results of Table 2.3 reveal the importance of estimating the moment of inertia as exact as possible. All frequencies calculated with $I = 2.779 \times 10^{10}\,\mathrm{mm}^4$ are 15.7 - 16.7 % lower than the frequencies calculated with $I = 4.079 \times 10^{10}\,\mathrm{mm}^4$. Therefore, the natural frequencies are quite sensitive to the value of the evaluated stiffness of the orthotropic plate.

Likewise, the natural frequencies are quite sensitive to the boundary conditions of the plate. The values of a simply supported plate on four sides are nearly doubled, when all four sides are clamped. However, it seems of less importance when the plate is clamped in the stiffener direction and simply supported on the sides parallel to the stiffeners, as the frequency is only slightly higher when all sides are clamped.

The boundary conditions are not expected to be perfectly clamped, and as seen from the experimental results presented in Chapter 4, the estimates using a simply supported case is closest to the experimental results. The rather large difference between the results for a simple and clamped case also indicates that it is difficult in practice to model correct boundary conditions in an analytical approach.

As not only the first natural frequency is of interest, the five first natural frequencies for the plate calculated by the four methods assuming simply supported boundaries conditions can be seen in Table 2.4. The analytical methods assuming clamped boundary conditions will not be treated further as the estimated fundamental frequencies seems unrealistic high.

f_{mn} [Hz]	f_{11}	f_{12}	f_{13}	f_{14}	f_{15}
Differential equation, Eq. (2.15)	7.24	10.64	15.32	21.08	24.28
Rayleigh's fraction – Dickinson, Eq. (2.16)	6.46	9.54	13.83	19.23	22.18
Rayleigh's fraction – Authors, Eq. (2.19)	6.72	7.39	9.24	12.64	17.58
Rayleigh-Ritz, Eq. (2.20)	6.82	7.47	9.28	12.61	17.48

Table 2.4: First five natural frequencies for different approaches.

The importance of precise estimates of boundary conditions as well as stiffness parameters is very relevant when it comes to practical design. When the estimated fundamental frequencies in Table 2.3 are compared with the limit frequencies from the Danish National Annex given in Table 1.2. All methods using simply supported boundary conditions falls within an intermediate field: $6\,\text{Hz} < f_{11} < 10\,\text{Hz}$, which is neither designated “normally satisfactory” nor “often not satisfactory”. On the other hand, all methods assuming clamped boundary conditions falls with in: $f_{11} > 10\,\text{Hz}$, which Eurocode states as a “normally satisfactory condition”.

The values shown in Table 2.4 are plotted in Figure 2.6. Very good agreement is seen between the methods from Eq. (2.19) and Eq. (2.20), whereas the two other methods yield somewhat higher results. The quick increase in frequency seen in the approach using the differential equation and the Rayleigh fraction from Dickinson is notable compared to the more smooth curve by the two latter methods. Obviously, the four analytical methods fall within two categories, where the solution from the author’s derivation and Rayleigh-Ritz seem to be the most convincing.

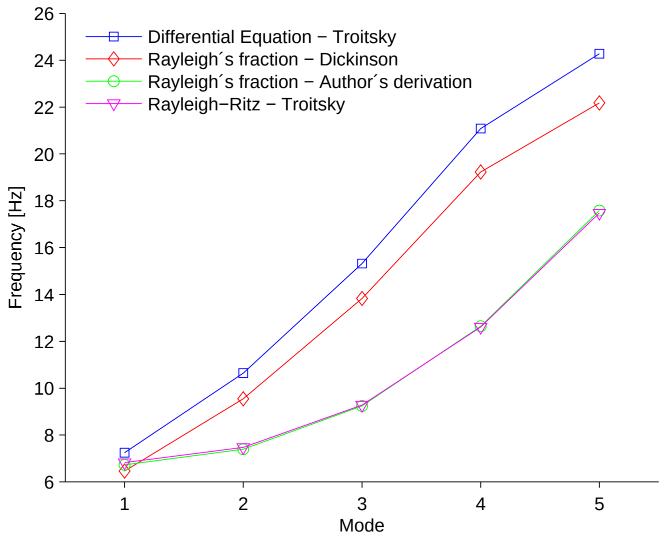

Figure 2.6: Results from methods assuming simply supported boundaries.

Chapter 3

ABAQUS Model

Due to the orthotropic composition of the deck, the numerical approach to determine the eigenmodes and -frequencies is made in the finite element (FE) program ABAQUS*. The deck is modelled with a shell and a solid model. To be able to make a comparison with the analytical calculations, both half a TTD element (corresponding to the beam model) and the full deck is modelled. This chapter describes which choices are made in the modelling process, the results, and the validity of the results.*

✦ ✦ ✦

It is sought that the models will have similar boundary conditions, and that they represent the real ones as good as possible. First of all, as illustrated in Chapter 1, the TTD decks lie on panels in the walls. Also, the concrete topping continues over the walls. This has given rise to two boundary conditions. The bottom of the TTD deck is supported against vertical translation. Furthermore, the surface of the concrete topping is pinned at the walls. An illustration of the aimed boundary conditions is showed in Figure 3.1.

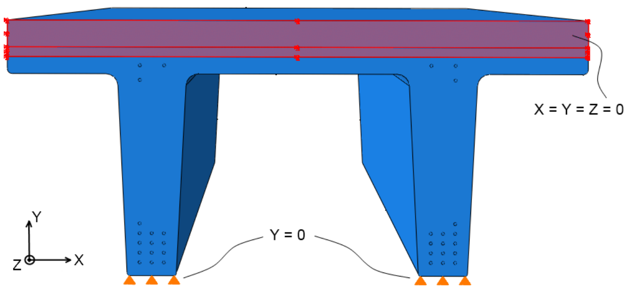

Figure 3.1: Illustration of chosen boundary conditions (equivalent to Figure 1.9).

The aimed boundary conditions mean that it is difficult to apply the exact same boundary conditions on both the shell and the solid model. In the solid model, the boundary conditions can be applied to the wanted surfaces of the model which match the real geometry, and hence the upper boundary condition will act as partly fixed. But in the shell model the boundary conditions can only be applied to points or edges of the shell. This means that it must be chosen whether the boundary conditions at the concrete topping must be considered as a fixity of the TTD element in the shell model, or if it should be considered pinned. As not all of the flange is connected at the borders, it is chosen that the shell model will be pinned at the flange of the deck.

3.1 Shell Model

The first FE approach is a shell model. In the following, the shell model is described along with illustrations of the eigenmodes and the natural frequency results.

3.1.1 Model Description

The shell model contains one shell for the rib and one for the horizontal part of the TTD element. To account for the increased stiffness due to the cables in the rib, beam elements are merged to the shell elements. A sketch of the principle is shown in Figure 3.2.

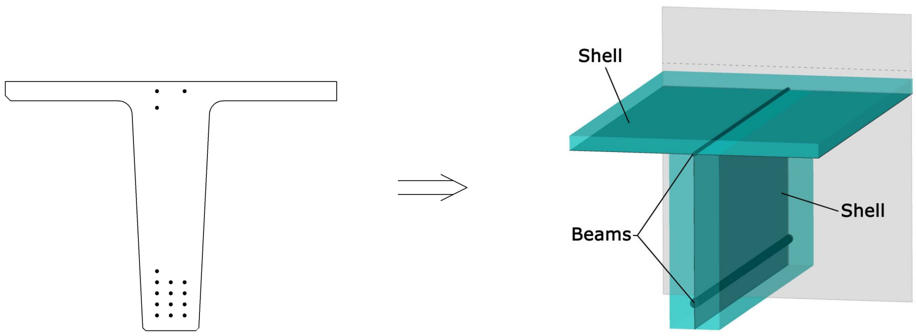

Figure 3.2: 3D sketch of shell model.

To merge the two shells, the shells must intersect. By default, the plane drawn will be the mid plane in depth, but it is possible to offset the shell from the plane, which is drawn. Hence, the two shells are drawn as a "T", and the upper shell is then offset from the intersection. The vertical shell which represents the rib is of uniform thickness, however in reality it is a trapezoid. Therefore, the shell is assigned a uniform thickness that will ensure an equivalent bending stiffness, EI, in the expected bending direction. This results in a uniform thickness of 241 mm.

The prestressed cables are represented by two steel beams. The lower beam accounts for the 13 cables at the bottom, and the upper beam accounts for 3 cables. As it is expected that the cables primarily contribute with axial stiffness, the corresponding beams have cross sectional areas equal to the sum of the areas of the cables. I.e. if the cross sectional area of a cable in the lower group are denoted $A_{\mathrm{cab},i}$, $i = 1,\ldots,13$, then the cross sectional area of the beam will be $A_{\mathrm{cab}} = \sum A_{\mathrm{cab},i}$. Furthermore, the lower beam is positioned at the centre of mass of the rebar group, whereas the upper is positioned at the intersection, see Figure 3.3.

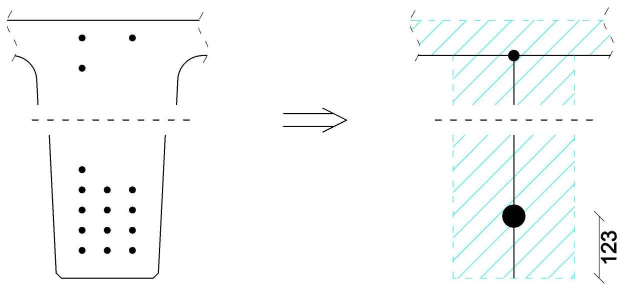

Figure 3.3: Equivalent modelling of rebars [mm].

Besides the TTD element, also the concrete topping is assumed to contribute to the stiffness of the deck. Therefore, the thickness of the upper shell is increased with 150 mm, which is the average thickness of the concrete topping. The concrete topping on top of the TTD deck also contains reinforcement in terms of Ø10 reinforcement with spacing of 150 mm in both directions, which can be included in a shell in ABAQUS. The reinforcement is then included as a layer with equivalent thickness at a given position in the shell. The rebar layer is typed in as shown in Figure 3.4, which also shows an illustration on how the rebar layer is implemented.

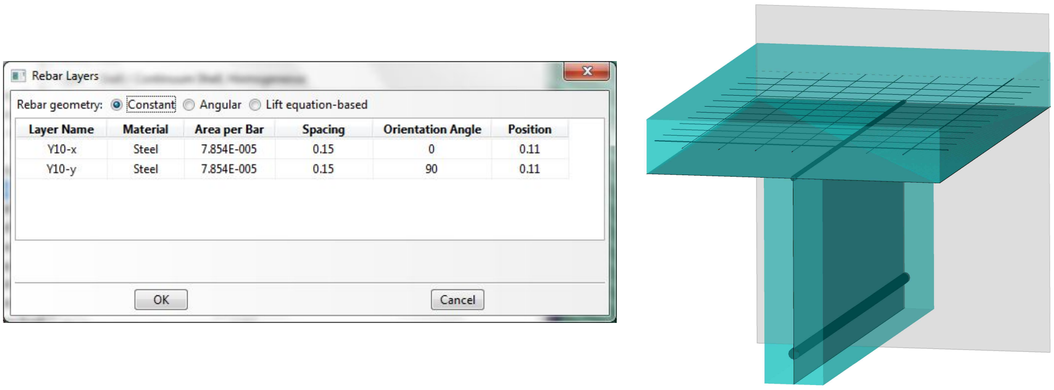

Figure 3.4: Rebar dialog box for shell and illustration of model.

The layers on top of the concrete topping is not assumed to contribute to the stiffness, but the mass will influence the eigenfrequencies. Therefore, the ratio between total mass and model volume is used to calculate an equivalent density, which is used for all materials to ensure the correct sum of masses of the shell model.

The shell model is evaluated for both half a TTD deck, as shown in Figure 3.2, and the full deck, which consists of 9 TTD elements, see Figure 3.5.

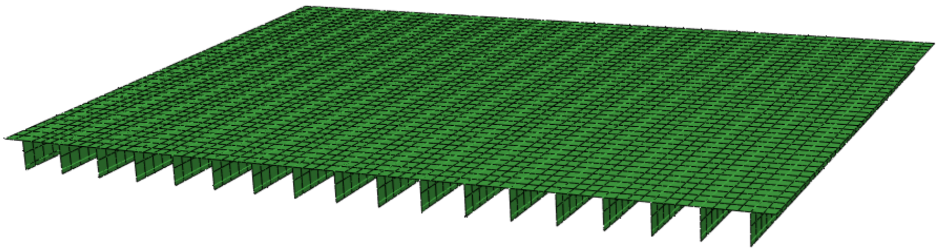

Figure 3.5: Shell model of full deck in ABAQUS.

The elements used in the shell model are *S8R* for shell elements, and *B32* elements for beam elements [23]. Both type of elements are quadratic elements. An example of the mesh in the shell model is shown in Figure 3.6.

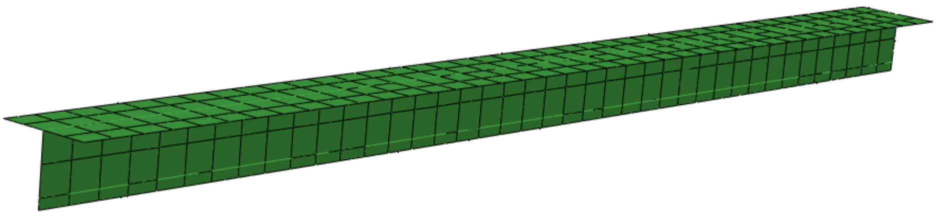

Figure 3.6: Example of mesh in the shell model.

The parts which are used in the shell model are listed in Table 3.1.

	Thickness t [mm]	Diameter D [mm]	Young's modulus E [GPa]	Poisson's ratio ν [–]	Element type
Vertical shell	241	—	40	0.2	S8R
Horizontal shell	220	—	40	0.2	S8R
Lower beam	—	45.07	200	0.3	B32
Upper beam	—	21.65	200	0.3	B32
Rebar layer	—	10	200	0.3	S8R

Table 3.1: Properties of the parts used in the shell model.

The shell model is found on the Appendix CD as the file `Shell.cae`.

3.1.2 Eigenmodes

As the half TTD element is simplified as a beam, additional boundary conditions are applied to avoid eigenmodes in the sideways direction as the beam is modelled in 3D. Hence, “rollers” are applied at the sides of the TTD element so it cannot move sideways nor rotate around its own axis. The first three eigenmodes for the beam are shown in Figure 3.7 to Figure 3.9.

Figure 3.7: First eigenmode for the beam model

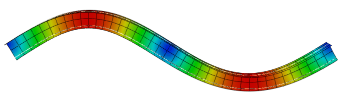

Figure 3.8: Second eigenmode for the beam model

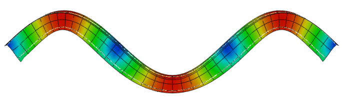

Figure 3.9: Third eigenmode for the beam model

The further modes of the beam model proceed in a similar manner with more oscillations. When

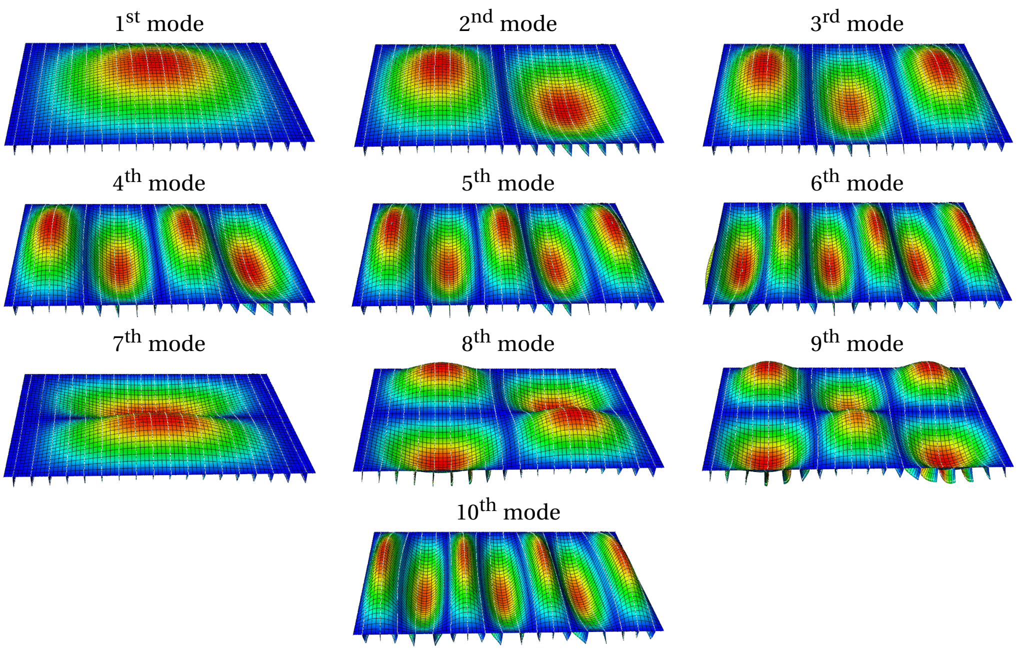

Figure 3.10: First 10 eigenmodes for the plate model.

the TTD elements are assembled to a full deck they act as a plate and will show a combination of modes from the two directions. The first 10 eigenmodes are shown in Figure 3.10.

3.1.3 Eigenfrequencies

The frequency analysis has been run to determine the first 10 eigenmodes for both shell models. The results are shown in Table 3.2.

Mode	Half TTD (beam) model [Hz]	Full deck (plate) model [Hz]
1	7.29	7.62
2	26.85	8.58
3	57.43	10.80
4	91.65	14.09
5	99.44	18.90
6	103.23	24.45
7	105.93	27.12
8	111.34	28.00
9	119.71	29.60
10	130.93	31.33

Table 3.2: First 10 eigenfrequencies for the shell models.

When comparing the mode shapes for the two models, it is found that mode 1 of the beam model corresponds to mode 1 of the plate model, and that mode 2 of the beam model corresponds to mode 7 of the plate model. This indicates that the stiffness in the perpendicular direction of the TTD elements is much smaller, and has little influence on the global stiffness of the deck. Furthermore, it demonstrates that a beam model is inadequate to give estimations on more than the first mode of the deck.

3.2 Solid Model

As a first approach, it was attempted to model the solid model as close to reality as possible. By this, the main difference from the shell model is that each cable in the TTD element is modelled separately. However, it showed that because of the very fine mesh necessary near each cable, the model became too computational heavy to work with. Therefore, an approach similar to the shell model was adopted for modelling of the cables.

3.2.1 Model Description

To reduce computational time significantly, the two groups of cables are assembled into two single cables with the same assumptions as for the shell model. The correct and the simplified geometry of the half TTD element are seen in Figure 3.11.

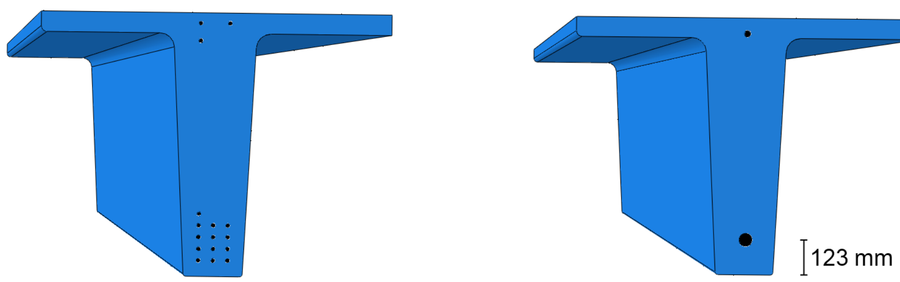

Figure 3.11: Left: Model with correct geometry. Right: Simplified model.

As for the shell model, the concrete topping is added on top of the TTD element, but the reinforcement is modelled as a thin steel plate. The thickness of this plate is chosen so the volume is equal to the total volume of the reinforcement, resulting in a plate with a thickness of 1 mm. The full model of a half TTD element is seen in Figure 3.12 with the borders of the thin steel plate marked with red colour.

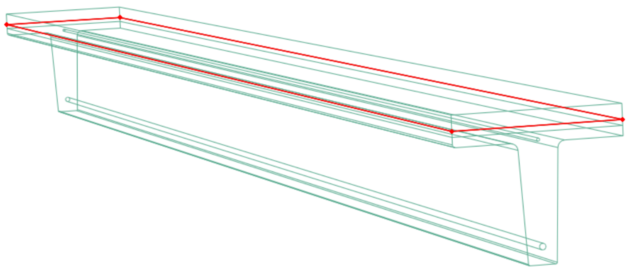

Figure 3.12: Model of half TTD element with concrete topping included.

Also the solid model is assembled to a full deck consisting of 9 TTD elements, see Figure 3.13.

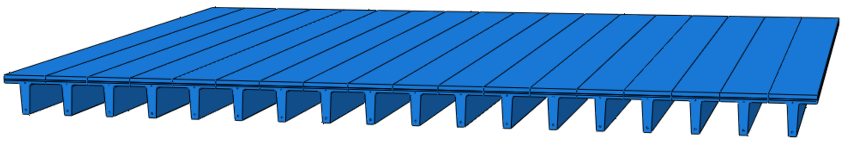

Figure 3.13: Solid model of full deck.

When conducting a dynamic analysis on a solid model, care must be taken when choosing element types. Especially when choosing linear elements, the results might become misleading due to phenomena like *shear locking* and *hourglassing*, which are further explained in [26]. The element type chosen for the solid model is *C3D20R*, however when evaluating the full deck, this choice of element type made the model too computationally heavy. This means that the beam model is modelled with *C3D20R* elements, and the plate model is modelled with *C3D15* elements. Both element types are quadratic elements. An example of the mesh is shown in Figure 3.14.

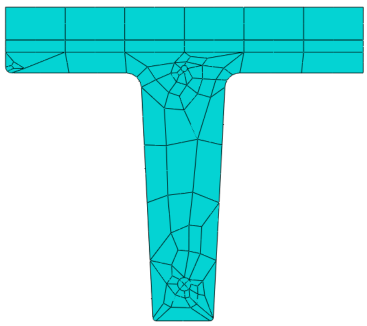

Figure 3.14: Example of mesh in the solid model.

The solid model is found on the Appendix CD as the file `Solid.cae`.

3.2.2 Eigenmodes

The mode shapes for the beam are similar to the ones of the shell model. However, due to the partly fixed ends, the curvature near the ends is different, which for the top side correspond to the shape of a fixed beam, see Figure 3.15.

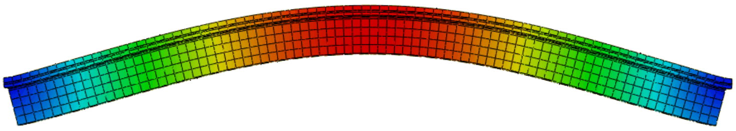

Figure 3.15: First eigenmode of solid beam model.

The mode shapes of the full deck are also very similar to the ones of the shell, and the difference in curvature is not as pronounced as for the beam model. The main observed difference is that the 10th mode is different, see comparison in Figure 3.16.

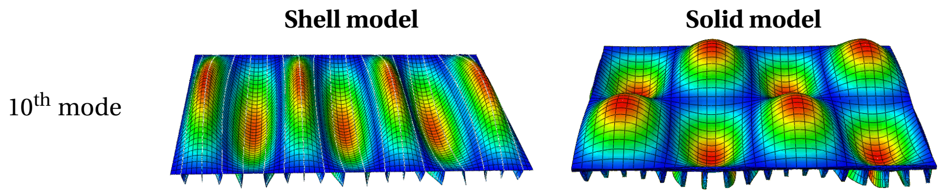

Figure 3.16: Comparison of 10th mode for both models.

3.2.3 Eigenfrequencies

The frequency analysis has been run to determine the first 10 eigenmodes for both solid models. The results for both are shown in Table 3.3.

Mode	Half TTD (beam) model [Hz]	Full deck (plate) model [Hz]
1	9.15	8.07
2	27.89	8.90
3	59.17	10.94
4	91.95	14.50
5	110.15	19.54
6	114.33	25.87
7	116.00	26.61
8	125.11	27.98
9	137.25	29.89
10	139.48	32.44

Table 3.3: First 10 eigenfrequencies for the solid models.

It is evident that when comparing to the shell model, the choice of boundary conditions has significant influence on whether the deck can be simplified to a beam model. The results show a higher first frequency for the beam model than for the plate model, which is not expected, as the plate model has additional stiffness from the perpendicular direction. The first frequency is even higher if the same element type is used for the beam (*C3D15*). This indicates that partly fixed boundary conditions have smaller influence when the plate model is considered. Actually, the eigenfrequencies for the plate model are close to the ones for the shell plate model, see Table 3.2, though slightly higher.

3.3 Selection of Model for Response Analysis

To model the response of the deck when exposed to loads, one model must be chosen which can satisfy the behaviour of the deck, but which is not too computationally heavy. It is obvious that a beam model is not adequate to model the behaviour of the deck as the two first modes actually represents the first and seventh mode of the deck. Therefore, a plate model must be chosen. The solid plate model is expected to give slightly more accurate results than the shell equivalent, as it the real geometry can be modelled quite accurately. However, the solid model is so computationally heavy, that it is not suitable for time series of response analyses. Furthermore, the shell plate model gives results which are close to the ones of the solid model. The only visible difference appears at the tenth mode, which indicates that the rigidity of the plate might be interpreted slightly different in the two models. As the tenth and higher modes are not considered relevant, and as the shell plate model is computationally much lighter to run, the shell plate model is chosen henceforth in the project.

Chapter 4

Experiments in Nordkraft

In order to clarify the properties of the floor construction, and if possible update certain parameters of the analytical and numerical models, a series of tests were performed both on top and from underneath the floor. This chapter presents the experiment set-up and results of the tests.

✦ ✦ ✦

4.1 Experiment Set-up

The investigated floor construction is situated with its upper surface in the sports hall under management of DGI-Huset and beneath in the main theatre hall of Teater Nordkraft. This gave rise to the requirement that the experiment set-up had to be light and easy to put up and remove again. As the underside of the deck is located 6 metres above the floor in the theatre hall, an easy to install reference point for a displacement transducer was abandoned, and the initial equipment was chosen to focus on an accelerometer. The used accelerometer, produced by Brüel & Kjær with model name 4370 and capable of measuring frequencies from 0.1 to 4800 Hz, is connected to a signal amplifier which is used to set the output signal to an appropriate level. The signal amplifier is wired to a so-called spider which handles the connection to the PC. It also allows more transducers to be connected if needed. The signal is logged by the program CATMANEASY at 1200 Hz and stored into `.asc` files. These files are loaded into MATLAB where the actual data processing takes place. The set-up can be seen in Figure 4.1 for measurements both on top and underneath the deck.

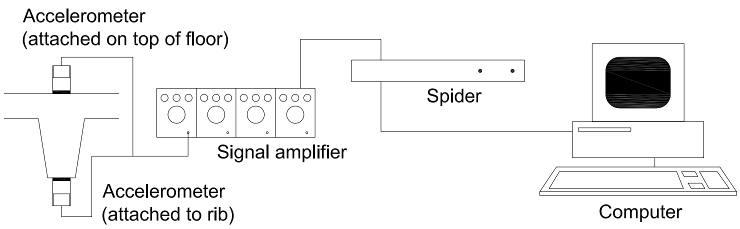

Figure 4.1: Set-up used for the experiments.

The data acquiring frequency, also called sampling frequency, has influence on the final data signal and treatment in many ways. As an example, the capture of one period of a sine wave with a frequency of 12 Hz at three different sampling frequencies, namely 60, 120, and 1200 Hz are shown in Figure 4.2.

The main data treatment consists of an FFT analysis which in short analyses the signal and returns a plot of which frequencies are present in the measured signal and their magnitude of amplitude relative to the amount of data samples H. The FFT analysis used in this project is carried out in the MATLAB script `FFT.m` which uses the built-in MATLAB function `fft(x)`. The procedure behind the FFT analysis is explained in more detail in Appendix C. One of the properties of the FFT analysis is that the sampling frequency has to be at least twice of the desired highest frequency of interest. Therefore, the sampling frequency becomes important in yet another way.

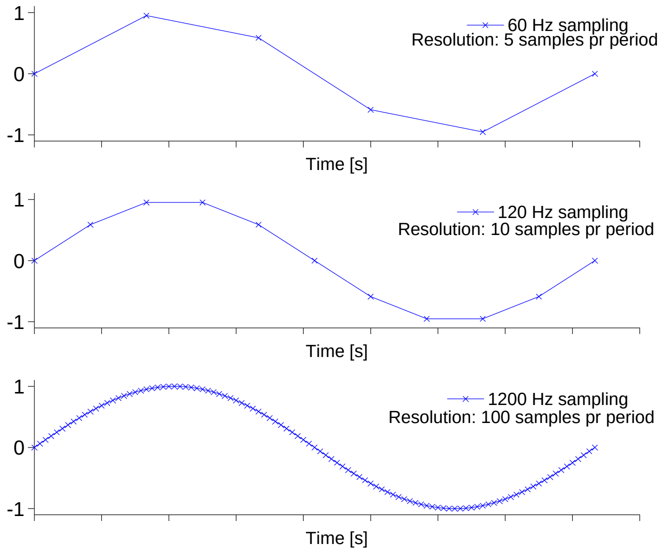

Figure 4.2: Capture of 12 Hz sine wave with three different sampling frequencies.

This is illustrated in Figure 4.3 where a sine wave with a frequency of 50 Hz is generated and sampled at the same three sampling frequencies as previously. The signals are hereafter run through the FFT analysis and the results can be seen in the rightmost figures. As seen from the signal sampled at 60 Hz, the FFT is not capable of identifying the frequency of 50 Hz whereas it detects a frequency at 10 Hz which is not actually present in the generated signal, this phenomenon is called aliasing and occurs since the signal is undersampled. To avoid undersampling the signals when performing the experiments at Nordkraft, the sampling rate was kept at 1200 Hz.

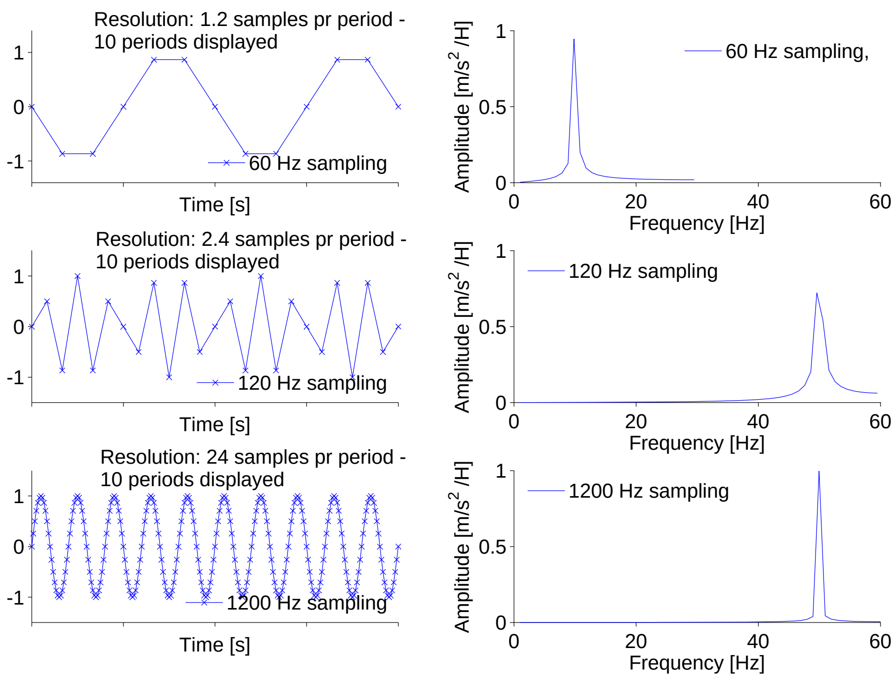

Figure 4.3: Resulting FFT spectrum according to sampling frequency.

4.2 Initial Experiments on Upper Side of Deck

The first experiments to be performed were carried out on top of the sports floor as it was easier than rigging the accelerometer to the deck at 6 metres height from the floor of the theatre hall. The tests were done in order to investigate if the floor construction in reality had vibration modes excitable by rhythmic human motion, as analytical hand calculations predicted anything between 6 and 16 Hz depending on boundary conditions and interaction of the layers in between. Initially, the exact centre point of the floor was chosen for measurements, but as seen in Figure 4.4 a heel impact load dissipated to fast for any modes to be detected. It was concluded that the Boflex sports floor was able to dissipate the relatively small load and vibrations from the heel impact too fast for any vibration to take place in the deck or at least to be measured with the accelerometer on top of the Boflex floor.

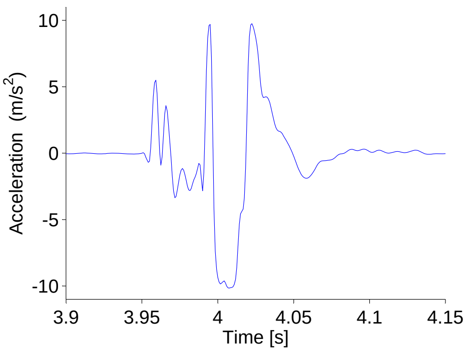

Figure 4.4: Measured acceleration signal from an initial heel impact test.

Several places on the floor, casings for fixing the various nets for sports activities like badminton and volleyball are moulded into the floor through the Boflex construction. These casings are casted into the concrete topping, and it was chosen to do measurements from one of these holes instead. An example of such a hole is show in Figure 4.5 and the corresponding measured acceleration signal is seen in Figure 4.6.

Figure 4.5: Casing used for measurements.

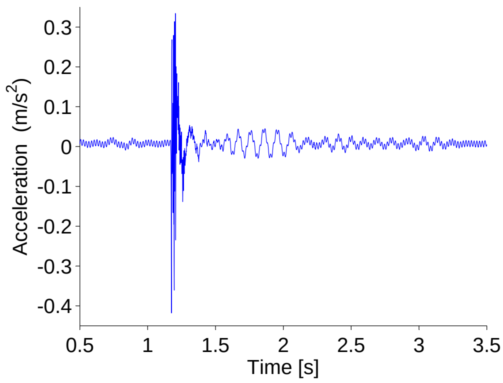

Figure 4.6: Measured acceleration signal from heel impact test with accelerometer in hole.

Six heel impact tests were performed, and from these signals, FFT analysis was used to identify possible modes at approximately 8.2, 9.4, 11, and 13 Hz, see Figure 4.7. The plots and data from the upper side tests are treated in `DataTreat_Upper.m`.

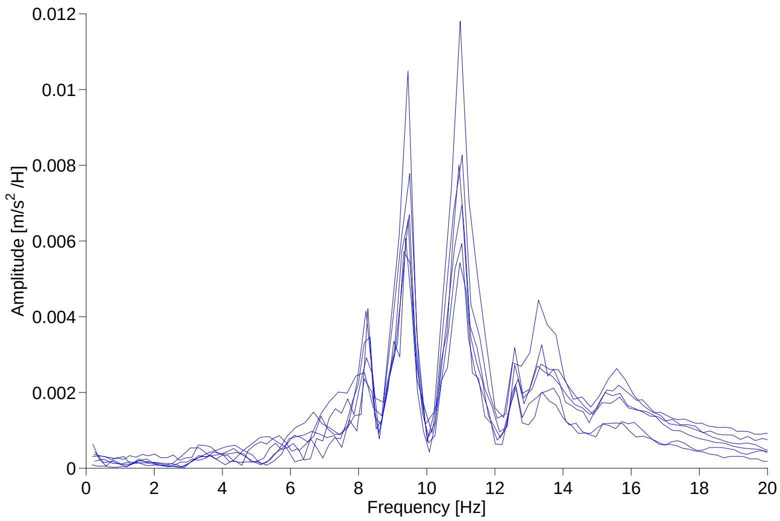

Figure 4.7: FFT plot of 6 impact tests with accelerometer placed in hole.

After the modes were identified, six jumping load tests were performed in order to see if it was possible for one man to excite one or more of the modes. No audio files were used to synchronize the jumping frequency to a specific frequency, but as it can be seen in Figure 4.8 the jumping frequency was very close to 2.2 Hz in all six tests. Jumping at 2.2 Hz should in theory make the fifth harmonic excite the mode at 11 Hz, which is also seen to be the case from the figure.

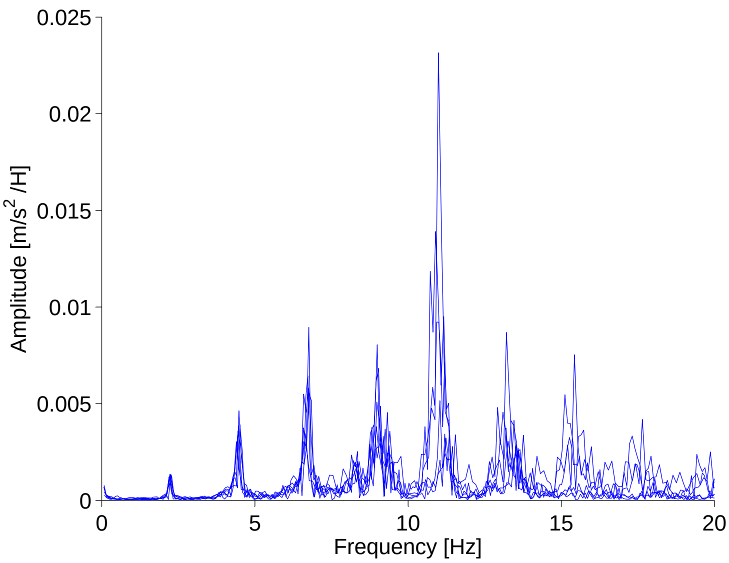

Figure 4.8: FFT plot of initial jumping load tests.

4.3 Experiments on Underside of Deck

After identifying the actual possibility of exciting some of the vibration modes by rhythmic jumping, it was also chosen to do measurements from underneath the deck in order to spot possible differences between measuring directly on the TTD element and on top of the complex floor construction. At the underside of the deck lighting equipment for use in the theatre is attached to the ribs. The hinges used for the lighting equipment is made from metal and hence attaching the accelerometer by the use of a magnet was possible. Wooden shims were installed between the rib and hinge to ensure as little independent movement of the hinge itself as possible. The accelerometer attachment can be seen in Figure 4.9. The accelerometer was attached midspan at rib 9, see Figure 6.1.

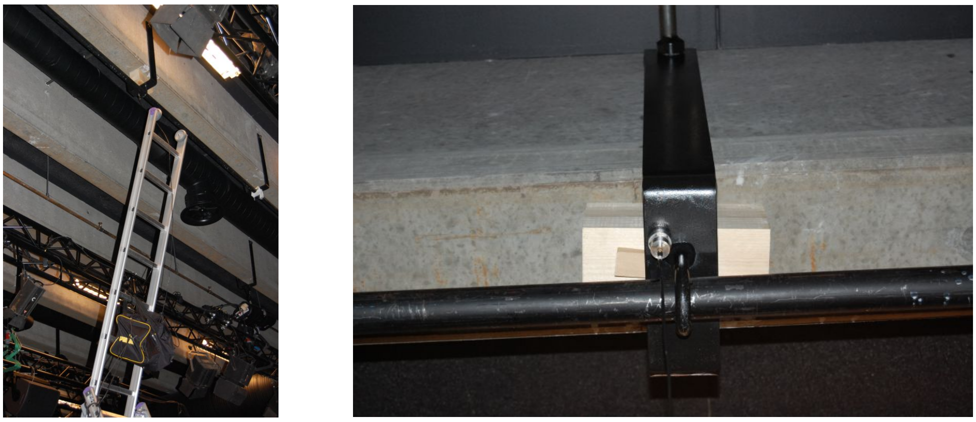

Figure 4.9: Accelerometer attachment method at underside of the deck.

The first tests to be run were three heel impact load test to compare with the ones from the upper side tests. The data treatment of the underside tests are carried out in `DataTreat_Under.m`. FFT plots from both test locations are shown in Figure 4.10. From impact tests at the underside, vibration modes could be detected at approximately 8.4, 11, 12.7 and possibly at 18.6 Hz. When comparing the two test series in Figure 4.10, it is seen that the upper side tests indicate a mode at approximately 9.4 Hz which is not seen from the underside tests. This can be explained by looking at Figure 3.10 where it can be seen that an accelerometer placed at the centre of the floor, which is the case for the measurements from the theatre hall, will not be able to detect the second mode as no vibration due to that mode is taking place at the centre point.

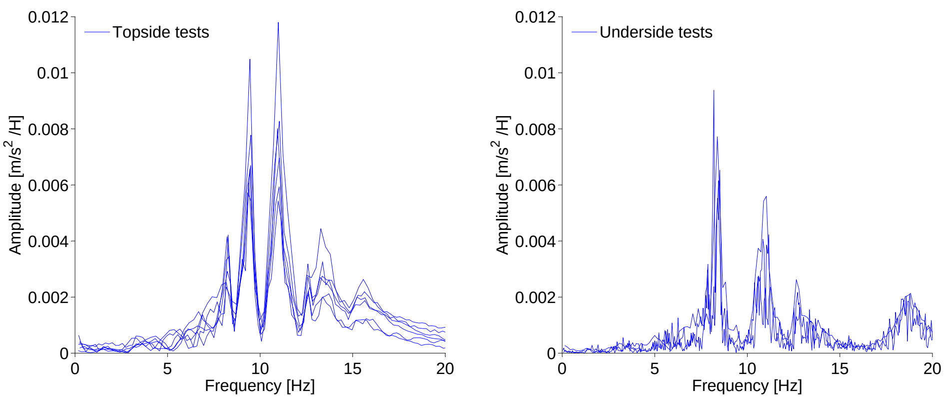

Figure 4.10: FFT plots of upper- and underside impact tests.

For the underside tests a more coordinated sequence of jumping tests were prepared. Music tracks that followed specific paces were selected so the jumping person would be able to jump at certain frequencies more accurately. An investigation of how accurately it in fact is possible to jump at various frequencies was made and is presented in Appendix D. Five frequencies were chosen to represent the spectrum of possible jumping frequencies, namely 1.6, 2.0, 2.1, 2.2, and

2.5 Hz. The frequencies 1.6, 2.0 and 2.1 Hz were chosen to identify the mode around 8 Hz more accurately, whereas the frequency 2.2 Hz was chosen to try to excite the mode at 11 Hz. The 2.5 Hz tests were done to elaborate the region between the two modes of 9 and 11 Hz as the fourth load component should be situated at around 10 Hz depending on how well the jumper was able to hit 2.5 Hz. FFT plots corresponding to the tests done at these frequencies is seen in Figure 4.11.

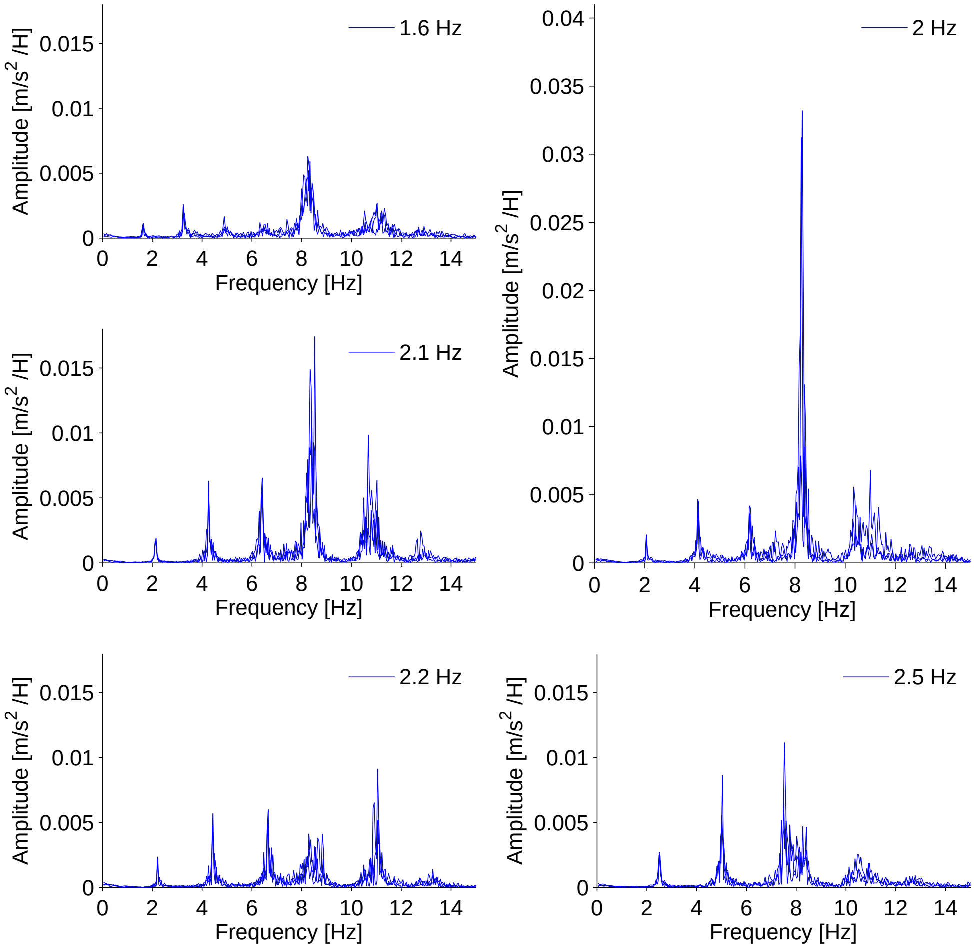

Figure 4.11: FFT plots of underside accelerations generated by jumping at various frequencies.

By looking at the FFT analysis plots, it is clear that the mode just above 8 Hz is able to be excited by one person jumping at slightly above 2 Hz due to the fourth harmonic, $4 \cdot 2.07\,\mathrm{Hz} = 8.28\,\mathrm{Hz}$. Here, the 2.07 Hz is taken as the actual jumping frequency as it can be read from the FFT plot. From the FFT plot it is also seen that the frequency of the mode is probably at 8.3 Hz rather than 8.4 Hz based on the peak values. Jumping at 1.6 Hz will also excite the 8.3 Hz mode, just not to the same magnitude. This is mainly due to the fact that when the fifth load component excites the mode, it carries less energy than lower load components. Also the fifth multiplier of 1.63 Hz is 8.15 Hz, so the excitation might be just in the beginning of the resonance region. This property is also seen from the 2.1 Hz jumping tests, were the actual jumping frequency is more likely to be 2.15 Hz, which causes the fourth harmonic to hit in the outer area of resonance, making the dynamic amplification less severe.

The mode at approximately 11 Hz was sought excited by the tests at 2.2 Hz, but no really clear resonance is experienced from this test series. The dynamic amplification seen at around 11 Hz is of same magnitude as seen in the 2.1 Hz jumping tests, so either this mode is not of same importance as the one at 9 Hz, or it is sufficiently narrow banded for none of the tests to hit close to pure resonance. This however, is not very likely as the 2.1 Hz and 2.2 Hz tests series covers the region around 11 Hz pretty well due to the spread in actual jumping frequency.

In Table 4.1 the results for the two tests series are summarized for the four first natural frequencies. Also, four target frequencies are stated, which represent the best estimates on the natural frequency for each mode.

f [Hz]	Mode	Upperside	Underside	Target
	1	8.2	8.3	8.3
	2	9.4	N/A	9.4
	3	11.0	11.0	11.0
	4	13.0	12.7	12.7

Table 4.1: Natural frequencies found from experiment.

4.4 Damping Ratio Determination from Half-Band Width Method

The tests conducted at Nordkraft can also be used for estimating the damping ratios of the deck. One of the two used methods is called the half-band width method and estimates the damping ratios by taking a closer look at the region around the resonance peak in the frequency domain from a impact excitation. The half-band width method identifies the peak and the magnitude of the peak. The half power value is calculated with Eq. (4.1) and the frequencies $f_{HP,1}$ and $f_{HP,2}$ corresponding to the half power magnitude are found. The damping ratio is given by either Eq. (4.2) or Eq. (4.3). If the resonance peak is well captured, the two calculation methods will give similar results. The method is illustrated in Figure 4.12 for the 2nd mode. The signals used for the half-band width method are zero-padded, which means zeros have been added to the original signal before the FFT analysis are performed. This does not add more information to the FFT plot, it only adds resolution and scales the amplitude values. The added resolution makes it possible to identify the half power frequencies more accurately.

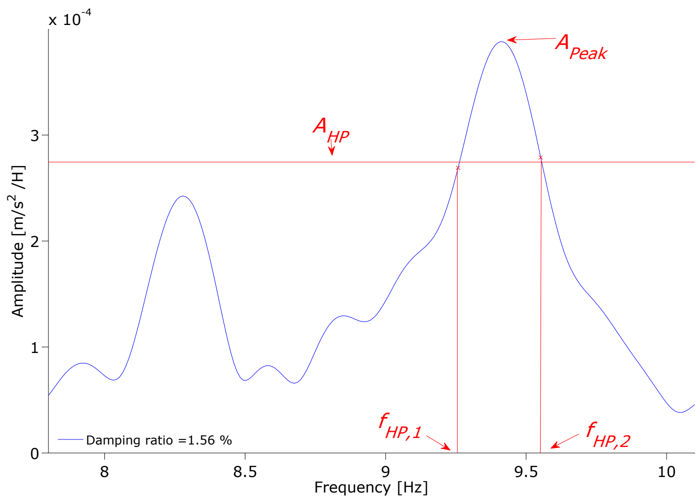

$$A_{HP} = \frac{A_{Peak}}{\sqrt{2}} \tag{4.1}$$

$$\zeta = \frac{f_{HP,2} - f_{HP,1}}{f_{HP,2} + f_{HP,1}} \tag{4.2}$$

$$\zeta = \frac{f_{HP,2} - f_{HP,1}}{2 f_{A_{Peak}}} \tag{4.3}$$

Figure 4.12: Illustration of half-band width method.

Six impact tests were conducted to determine the damping ratios of the first three vibration modes. The calculations and treatment of the data are carried out in `HalfPower.m`. The ratios obtained from the half-band width method are listed in Table 4.2.

Damping Ratio from Heel Impact	Mode	Damping Ratio, ζ [%]							
		1	2	3	4	5	6	Mean	
Using Eq (4.2)	1	2.39	1.29	1.88	N/A	1.58	1.70	**1.77**	**1.80**
	2	1.97	1.56	1.83	1.71	1.69	1.37	**1.69**	
	3	2.00	2.12	1.94	1.88	2.02	1.80	**1.96**	
Using Eq (4.3)	1	2.37	1.29	1.87	N/A	1.58	1.70	**1.76**	**1.80**
	2	1.98	1.56	1.82	1.71	1.69	1.37	**1.69**	
	3	1.99	2.11	1.94	1.88	2.02	1.79	**1.96**	

Table 4.2: Estimated damping ratios.

In the used dynamic models, it is implicitly assumed that the system of the deck can be decoupled into a system of independent modal equations. This is generally the case for lightly damped systems, where the eigenfrequencies are sufficiently separated [17]. Coupling between the different modal coordinates is dependent on the velocity term and hence the damping term. When assuming modal decoupling, damping can be expressed through the damping ratio ζ for the given mode, and as explained by Nielsen [17], decoupling can be assumed if Eq. (4.4) is fulfilled.

$$\omega_n\,(1+a\,\zeta_n) \quad < \quad \omega_{n+1}\,(1-a\,\zeta_{n+1})\ , \qquad \text{where} \qquad a\approx 2-3 \tag{4.4}$$

Eq. (4.4) is applied in the two limit cases, when $a = 2$ and $a = 3$ as shown Eq. (4.5). Only the separation of the first three modes is controlled.

$$\begin{aligned}
a=2 \qquad & \underbrace{\omega_1 = 2\pi\cdot 8.3\text{ Hz}\,,\ \zeta_1 = 0.0177 \qquad \omega_2 = 2\pi\cdot 9.4\text{ Hz}\,,\ \zeta_2 = 0.0169}_{\omega_1\,(1+a\,\zeta_1)\quad<\quad\omega_2\,(1-a\,\zeta_2)\quad\Leftrightarrow\quad 53.99\quad<\quad 57.07} \\
& \underbrace{\omega_2 = 2\pi\cdot 9.4\text{ Hz}\,,\ \zeta_2 = 0.0169 \qquad \omega_3 = 2\pi\cdot 11.0\text{ Hz}\,,\ \zeta_3 = 0.0196}_{\omega_2\,(1+a\,\zeta_2)\quad<\quad\omega_3\,(1-a\,\zeta_3)\quad\Leftrightarrow\quad 61.06\quad<\quad 66.41} \\
a=3 \qquad & \underbrace{\omega_1 = 2\pi\cdot 8.3\text{ Hz}\,,\ \zeta_1 = 0.0177 \qquad \omega_2 = 2\pi\cdot 9.4\text{ Hz}\,,\ \zeta_2 = 0.0169}_{\omega_1\,(1+a\,\zeta_1)\quad<\quad\omega_2\,(1-a\,\zeta_2)\quad\Leftrightarrow\quad 54.92\quad<\quad 56.07} \\
& \underbrace{\omega_2 = 2\pi\cdot 9.4\text{ Hz}\,,\ \zeta_2 = 0.0169 \qquad \omega_3 = 2\pi\cdot 11.0\text{ Hz}\,,\ \zeta_3 = 0.0196}_{\omega_2\,(1+a\,\zeta_2)\quad<\quad\omega_3\,(1-a\,\zeta_3)\quad\Leftrightarrow\quad 62.06\quad<\quad 65.05}
\end{aligned} \tag{4.5}$$

Eq. (4.5) reveals that modal decoupling can be assumed for the first three modes of vibration, as the inequality in Eq. (4.4) is fulfilled in every case.

4.5 Damping Ratio Determination from Logarithmic Decrement Method

The half-band width method used in Section 4.4 is a rather imprecise method for determination of the damping properties of a structure. This is due to the fact that the method is very dependent on the quality of the Fast Fourier Transform of the acceleration signal, which itself is very sensitive to e.g. noise. However, this might be the best solution at hand.

Nevertheless, it has also been attempted to find the damping ratios of the three first modes by means of the logarithmic decrement method. Again, impact tests are used, where the damping ratio of the first and third mode is found using the tests measured on the underside of the floor, while the damping ratio of the second mode is found using a test from the upper side of the floor.

Application of the logarithmic damping method requires an acceleration signal with a free decay, where the oscillations are performed with the natural frequency matching the specific mode of interest. But the acceleration signals from the impact tests are first of all quite noisy, and secondly, the signal contains oscillations with numerous frequencies. In order to prepare the acceleration signal for a logarithmic decrement analysis, a bandpass filter is applied to the time series, which is done in the MATLAB-file `Bandpass_filter.m`. The procedure is explained in relation to the damping ratio of the first mode.

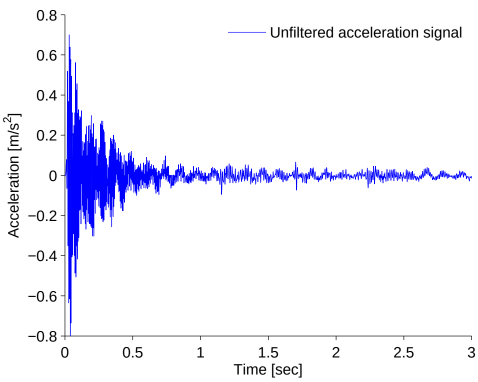

Figure 4.13: Unfiltered acceleration signal.

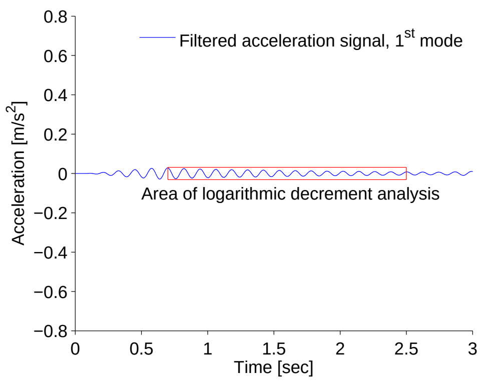

Figure 4.14: Filtered acceleration signal.

In Figure 4.13 and Figure 4.14, the unfiltered and filtered acceleration signal is shown, respectively, for an impact test where measurements are made on the underside of the deck. In Figure 4.14, oscillations with a frequency in the neighbourhood of the first natural frequency of 8.3 Hz have been filtered out of the original signal, see Figure 4.17 in comparison with Figure 4.16. After the bandpass filter is applied, the free decay is analyzed by means of the logarithmic decrement method as shown in Figure 4.14.

The method works by calculating the logarithmic decrement δ_i by the ratio of the magnitudes of subsequent peaks $a_{\max,0}$, $a_{\max,i}, \ldots$, $i = 1, 2, \ldots$ on the filtered acceleration signal. $a_{\max,0}$ is the magnitude of the first peak. The relationship given in Eq. (4.6) is utilized [17]:

$$\delta_i = \frac{1}{i} \ln\left(\frac{a_{\max,0}}{a_{\max,i}}\right) \quad \Leftrightarrow \quad i\,\delta_i = \ln\left(\frac{a_{\max,0}}{a_{\max,i}}\right) = \ln(R_a) \tag{4.6}$$

This relationship can be plotted for the used peaks in the analysis, and the logarithmic decrement can be estimated through the slope of a least square regression line. The method is illustrated in Figure 4.15 for the first mode.

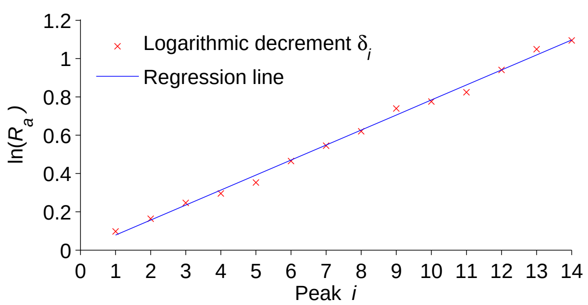

Figure 4.15: Linear regression of logarithmic decrement.

As seen from the figure, the fit of the regression line is rather close for the first mode, and this is also the case for the two remaining modes. From the found logarithmic decrement δ, the damping ratio ζ is found, see Eq. (4.7).

$$\zeta = \frac{\frac{\delta}{2\pi}}{\sqrt{1+\left(\frac{\delta}{2\pi}\right)^2}} \tag{4.7}$$

It should be mentioned that the acceleration signals of the impact tests are influenced quite much by higher frequencies, which cannot be explained from a structural point of view. This is seen from Figure 4.16, where a large concentration of energy is observed at higher frequencies. These higher frequencies seem to dominate the acceleration response immediately after the impact, after which the lower frequencies get excited.

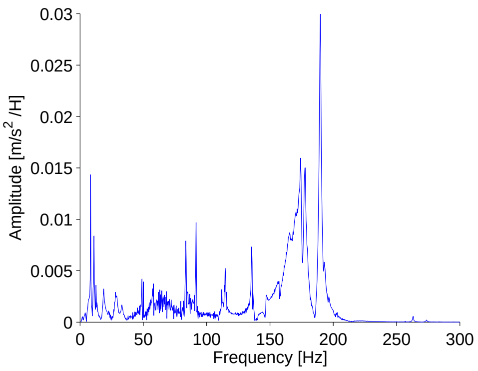

Figure 4.16: FFT plot of original signal.

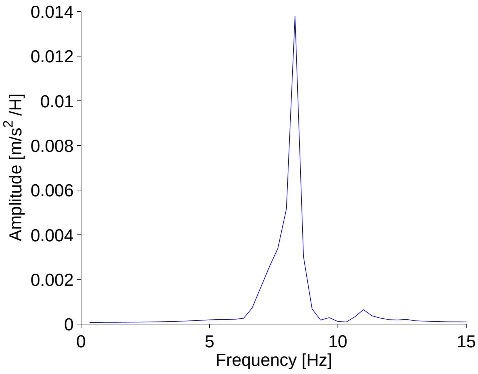

Figure 4.17: FFT plot of filtered signal.

The explained procedure is applied for the three first modes, and the results can be seen in Table 4.3. The shown bandpass filter intervals refer to frequency cut-off limits.

MODE	BANDPASS FILTER INTERVALS [Hz]	DAMPING RATIO ζ [%]
1	6.89–8.96	1.24
2	8.97–9.74	2.06
3	10.69–11.38	1.60

Table 4.3: Results of logarithmic decrement analysis.

The acceleration signals available for the logarithmic decrement analysis were not optimal. This is due to a relatively high amount of noise at higher frequencies than interesting in this assessment. Therefore, the results of the logarithmic decrement analysis serves merely as a reference case to the damping ratios from the half-band width method. As seen, the results from the two methods are of the same order of magnitude.

According to Bachmann et al. [3], the found damping ratios seem realistic for this kind of construction. For prestressed concrete constructions, he states an interval of 1 % to 3 % for the damping ratio.

Chapter **5**

Tuning of Models

To make it possible to get applicable responses in both the analytical model and the ABAQUS *model of the deck, these are tuned to meet the results from the conducted experiments. This means that it is attempted to tune the models so they approach the same natural frequencies which are detected in the experiments. If it is not possible to tune the models to obtain the same natural frequencies, the first frequency is prioritized, then the second, and so on.*

✦ ✦ ✦

The natural frequencies which have been computed, and the target frequencies estimated from the experiments, are listed in Table 5.1.

MODE	COMPUTED FREQUENCIES [Hz] ANALYTICAL PLATE MODEL (author's derivation, Eq. (2.19))	COMPUTED FREQUENCIES [Hz] ABAQUS MODEL (full deck – shell model)	TARGET FREQUENCY [Hz]
1	6.72	7.62	8.3
2	7.39	8.58	9.4
3	9.24	10.80	11.0
4	12.64	14.09	12.7

Table 5.1: Computed natural frequencies and target frequencies.

This chapter describes how the models which are intended to be used for the response investigation are tuned, and which limitations they each produce in comparison with the real behaviour detected in the experiments.

For both models, it has shown that the material parameters are the most appropriate to tune. The geometry is considered quite accurate, and the attempts to change the boundary conditions has shown that the initially chosen boundary conditions are in good agreement with the series of natural frequencies. However, the geometry is indirectly tuned in the analytical model as the bending stiffness EI which is tuned is the product of a material parameter E and a geometrical parameter.

5.1 Analytical Model

As seen in Table 5.1, the natural frequencies of the analytical solution are generally lower than the targets. The fourth mode seems to be almost equal to the target.

As illustrated in Chapter 3, only the mode number in the y-direction changes for the first six modes, whereas the mode number in the direction of the ribs remains at 1. This indicates that the rigidity in the x-direction is much larger than the rigidity in the y-direction. Therefore, the bending stiffness of the ribs is the main contributor to the modal stiffness for the first mode. As only the mode number in the y-direction increases for the next modes, the intervals between the frequencies of these modes are determined by the plate rigidity.

The parameters that have been changed to tune the analytical model are therefore the bending stiffness of the ribs EI, and the flexural stiffness of the plate D. The used EI takes the stiffness of the prestressed cables into account. With the first natural frequencies as first priorities, the bending stiffness of the ribs has been changed from $EI = 1.63 \times 10^9\,\mathrm{Nm}^2$ to $EI = 2.44 \times 10^9\,\mathrm{Nm}^2$. Here, it has not been distinguished between tuning of E and I. The flexural stiffness of the plate has been changed from $D = 3.70 \times 10^7\,\mathrm{Nm}$ to $D = 7.56 \times 10^7\,\mathrm{Nm}$, which results in the natural frequencies: 8.30, 9.40, 12.30, and 17.42 Hz. The first two natural frequencies are equal to the targets, but the third and fourth deviate with approximately 12 % and 31 %, respectively. The increase in stiffness of both ribs and plate can explained by the additional constraints caused by the boundary conditions, which are not perfectly simply supported.

The purpose of tuning the analytical model is to prepare a model based on modal decomposition. It has been chosen that this model should be able to represent the behaviour of the first three modes, and therefore the modal stiffness and modal mass of these three modes has been calculated in accordance with Eq. (A.7) in Appendix A after the tuning, see Table 5.2.

Mode	Modal Stiffness, k [$\times 10^6$ N/m]	Modal mass, m [$\times 10^3$ kg]
1	269.1	98.95
2	345.2	98.95
3	591.1	98.95

Table 5.2: Modal stiffness and modal mass of the first three modes.

5.2 ABAQUS Model

Like the results of the analytical solution, the calculated natural frequencies in ABAQUS are also lower than the detected ones in the experiments. Only the fourth natural frequency is higher, but as this is the frequency that has been least accurately determined, and furthermore is the least important, it is merely attempted to tune the model for the first three modes.

When the model is to be tuned, it seems most reasonable to change the parameters which are considered of most uncertain precision. This means that the main parameter that has been chosen for the tuning is Young's modulus of concrete. It was initially set to $E_c = 40\,\mathrm{GPa}$, but has been altered to $E_c = 48\,\mathrm{GPa}$, which gives the following four first natural frequencies: 8.30, 9.36, 11.79, and 15.39 Hz. The results of the tuning of the Abaqus model are overall better than the tuning of the analytical model. The first two natural frequencies are almost equal to the targets, and the deviations of the third and fourth are approximately 7 % and 21 %, respectively. These results are quite acceptable as the first three modes are of most interest. The change in Young's modulus is in good agreement with an article by Suikkanen, COWI [25], which states that the dynamic modulus can be taken as 20 % larger than the initial static modulus: $E_{c,dyn} = 1.2 \cdot 40\,\mathrm{GPa} = 48\,\mathrm{GPa}$. Young's modulus of steel is kept unchanged at $E_s = 200\,\mathrm{GPa}$, as it seems to be the optimal value.

The first two natural frequencies are very close to the targets, but the third, and especially the fourth, do not converge by altering Young's modulus.

Besides Young's modulus, other opportunities to alter the model is the geometry and the density. However, as both parameters are considered quite accurate, and as it is difficult to predict the change in frequencies due to an altered geometry, these are left unchanged.

5.3 Summary of Model Tuning

The parameters which have been changed are summed up in Table 5.3, and these values will be used henceforth in the report.

Here it must be noticed that the tuning of EI in the analytical model does not correspond to the tuning of E_c in the ABAQUS model. The tuned value of EI in the analytical solution corresponds to approximately $E = 60\,\mathrm{GPa}$ assuming that the same moment of inertia $I =$

	Original value	Updated value
Analytical model		
Bending stiffness of stiffeners, EI	$1.63 \times 10^9\,\mathrm{Nm}^2$	$2.44 \times 10^9\,\mathrm{Nm}^2$
Flexural stiffness of plate, D	$3.70 \times 10^7\,\mathrm{Nm}$	$7.56 \times 10^7\,\mathrm{Nm}$
ABAQUS *model*		
Young's modulus of concrete, E_c	40 GPa	48 GPa

Table 5.3: Tuned parameters.

$4.079 \times 10^{10}\,\mathrm{mm}^4$ for the rib is used, see Appendix B. Therefore, the tuning of the two models cannot be compared directly. However, this was also expected as the parameters such as moment of inertia and boundary conditions are not exactly the same in the two models. The resulting natural frequencies due to the changes are seen in Table 5.4.

	ANALYTICAL MODEL		ABAQUS MODEL	
MODE	Frequency [Hz]	Deviation [%]	Frequency [Hz]	Deviation [%]
1	8.30	0.0	8.30	0.0
2	9.40	0.0	9.36	−0.4
3	12.30	11.8	11.79	7.2
4	17.42	31.2	15.39	21.2

Table 5.4: Natural frequencies of tuned models and deviation from targets.

To illustrate the differences in the natural frequencies from the tuning, a plot of the results is seen in Figure 5.1.

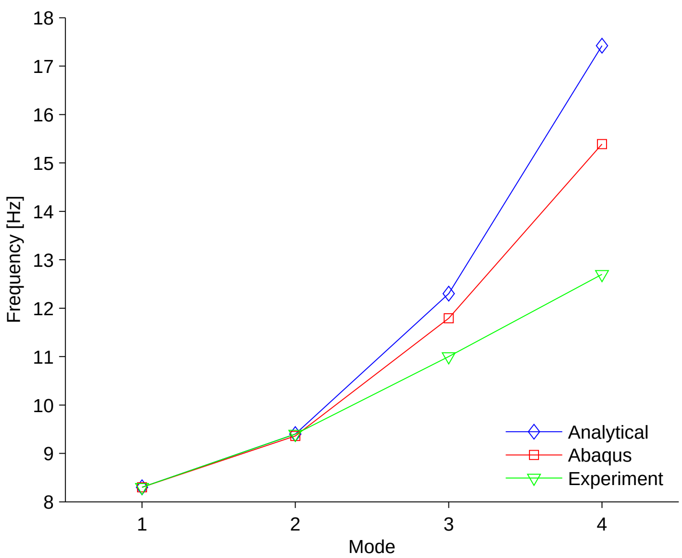

Figure 5.1: Plot of tuning results.

A precise model seems to be difficult to achieve for more than the first 2–3 modes. The value E_c should be carefully considered, and the stiffness of various kinds of reinforcement and prestressed cables should be included in the calculation model.

Chapter 6

Load Scenarios for Response Analysis

In this chapter load scenarios are defined from which the response of the deck is analyzed. The load is generated by jumping humans, and three different load areas are defined on the deck. The load areas are defined in such a way that each of them should excite one of the three first modes.

✦ ✦ ✦

The load scenarios defined in this chapter are based on the purpose of preparing a framework for response analyses. The jumping frequencies f_p are chosen in a region where it is known that it is fairly easy to keep the pace, and where accuracy of parameters such as contact ratio and jumping frequency has been investigated, see Appendix D. It is therefore elaborated that the control of the serviceability is merely based on these scenarios, and that other load scenarios most probably can be found which are more critical. Hence, the chosen load scenarios serve foremost as scenarios where reliable results are expected from the experiments.

The load areas, which form the basis for the response analysis, are defined in Figure 6.1. As seen from the figure each load area is defined in order to excite one of the three first modes. Clearly, the first scenario excites primarily the first mode, and also the third mode, whereas the second mode should not be excited. The second and third scenario will excite all modes, but primarily the one they are intended for.

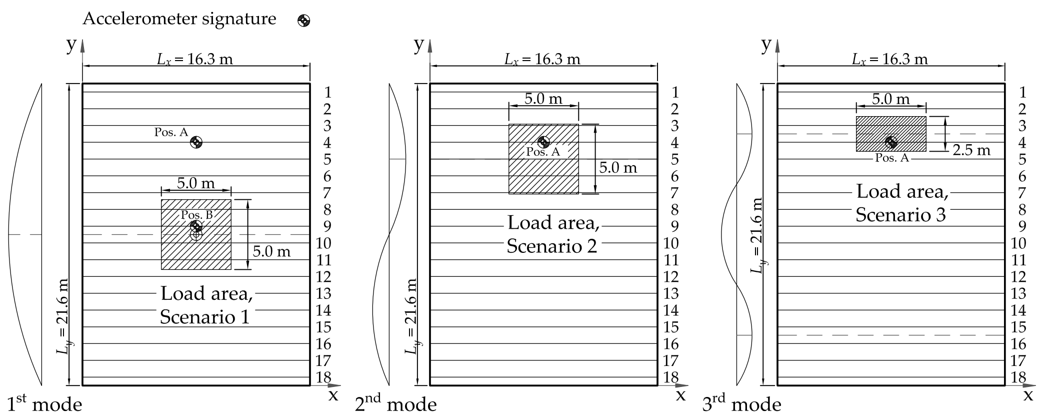

Figure 6.1: Load scenarios.

At most 20 humans are assumed to jump at the same time evenly distributed within the defined load areas, but also other intensities of jumping humans are examined in order to clarify the effect of synchronization between the individuals, also known as the crowd reduction effect. However, the number of people is only varied for the first scenario. It should be noticed that in the third scenario, the load area is half the size of the other load scenarios. The reason for this is that initially the jumping humans were divided in two equal sized groups to be placed in two load areas in each end of the floor, however due to obstacles on the floor, only one of the load areas was used, but the size was maintained, i.e. an area of half the size compared to the other scenarios.

On basis of the defined scenarios in Figure 6.1, the cases shown in Table 6.1 are examined with respect to the response of the deck, and these serve as reference situations both for calculation models and experiments. Hence, comparison between various calculation models and experiments is based on the cases defined in Table 6.1. The jumping frequency of the humans are varied through the various analyses, and generally it is attempted that one of the load components should hit resonance. The chosen jumping frequencies f_p means that the first natural frequency coincides with the fourth load components of the jumping frequencies for Scenario 1 and 2. The third natural coincide with the fifth load component for the jumping frequency in Scenario 3. To compare the response analysis in Chapter 8 with the results from the conducted experiments, the masses of the participants in the experiments have been recorded. The sum of these has been used to calculate an equivalent distributed load on the load areas. The average weight and the equivalent load are shown in Table 6.1.

Type of experiment	Jumping humans	Average			Acc. Pos.
		Mass [kg]	Weight [N]	Load [N/m^2]	
Control of serviceability limit state					
Scenario 1, $f_p = 2.08\,\text{Hz}$, $4f_p = 8.3\,\text{Hz}$	20	76.5	750	600	A
Scenario 2, $f_p = 2.35\,\text{Hz}$, $4f_p = 9.4\,\text{Hz}$	20	76.5	750	600	A
Scenario 3, $f_p = 2.20\,\text{Hz}$, $5f_p = 11.0\,\text{Hz}$	20	76.5	750	1201	A
Parameter study of crowd reduction effect					
Scenario 1, $f_p = 2.08\,\text{Hz}$, $4f_p = 8.3\,\text{Hz}$	20	76.5	750	600	B
	15	77.6	761	457	
	10	76.4	750	300	
	5	75.8	744	149	
Parameter study of human damping effect					
Scenario 1, $f_p = 2.08\,\text{Hz}$, $4f_p = 8.3\,\text{Hz}$	5 + 5 passive	71.0	697	139	B
	5 + 10 passive	71.0	697	139	
	5 + 15 passive	71.0	697	139	

Table 6.1: Average weights and loads from participants.

The designation “Acc. Pos.” refers to the position of the accelerometer in the experiments, which have been performed to measure the response. As the accelerometers are attached to the ribs, the accelerometer at Pos. B is attached to the 9$^{\text{th}}$ rib. Although the distance between the 9$^{\text{th}}$ rib and the exact midpoint of the deck $(x, y) = (L_x/2, L_y/2)$ is 600 mm, these two terms are used indiscriminately.

Generally, three main aspects are analyzed through both calculation models and experiments. According to Table 6.1, the substance of them is described in greater detail:

- *Control of serviceability limit state.* The magnitude of acceleration is compared to the limits given in Table 1.2. Assessment of the accelerations is based on the three load scenarios defined in Figure 6.1 and Table 6.1, and for each mode the jumping frequency of the humans is adjusted to hit the natural frequency of the considered mode. As mentioned earlier these scenarios do not necessarily represent the most critical scenarios, and therefore it is stressed that this assessment cannot be seen as an conclusive control of the serviceability limit state.

- *Parameter study of crowd reduction effect.* The so-called crowd reduction effect is investigated by varying the number of jumping humans. Total synchronization of jumping humans is not achievable in practice, which means that the jumping load of a crowd of humans is not proportional to that of a single human. In the calculation models, an expression which takes this into account is sought for, and this can be compared to the experimental results.

- *Parameter study of human damping effect.* When passive humans are present on the floor, while others are jumping, the passive humans will damp the vibrational response. This effect is investigated by varying the number of passive humans.

Chapter 7

Load Models

Two different load models will be used in relation to the deck in Nordkraft, and these will be described in the this chapter. The first load model is the codified Danish model given in the Danish National Annex to Eurocode 1 [11]. The second model is suggested by Ellis & Ji [8]. Both models are assessed by comparing jumping tests.

✦ ✦ ✦

Generally, the two jumping load models are based on a Fourier series on the form given by Eq. (7.1). $F(t)$ designates the load time history and has the unit of [kN/m^2]. In the present case considering a deck fixed against horizontal translations, only the vertical forces are considered.

$$F(t) = G\left(1.0 + \sum_{i=1}^{\infty} \alpha_i C_i \sin\left(2\pi i f_\mathrm{p} t + \varphi_i\right)\right) \tag{7.1}$$

where

- G Static weight of humans per unit area [kN/m^2].
- C_i Crowd reduction factor for the i^{th} jumping load component. This is an empirically determined factor, which is only used in connection to the Eurocode-model, as it takes into account the synchronization of jumping people.
- α_i Fourier coefficient of the i^{th} jumping load component. α_i is stated in relation to the relevant load model, and is originally estimated from jumping experiments.
- φ_i Phase lag for the i^{th} jumping load component. The determination of φ_i is stated in connection to the relevant load model.
- f_p Jumping frequency of persons.

A typical representation of a jumping load from one human can be seen in Figure 7.1, which shows a part of a jumping load time history. Jumping loads are characterized by the fact that during a time period t_c, the jumping human is in contact with the ground, where a relatively high impact is applied on the deck. During the rest of the jumping load period T_p, the human is in the air.

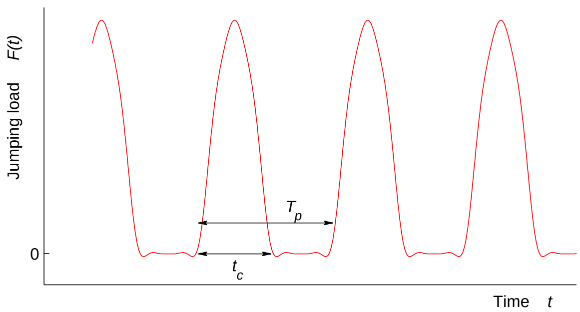

Figure 7.1: General representation of jumping load.

Jumping loads should be considered a specific case of human-induced loads, amongst for example walking or running. For all types of human-induced loads it should be considered if the load sources, i.e. the humans, are only influencing the load or also the dynamic properties of the construction, i.e. altering mass, damping, and stiffness properties. Nevertheless, experiments show that jumping loads should not be considered to alter the dynamic properties of the construction [9]. This assumption is based on the fact that all humans in a specific crowd are jumping. Standing humans on the deck will definitely alter the dynamic properties of the construction.

7.1 Eurocode Load Model

The load model given in the Danish National Annex to Eurocode 1 is a general model, which can also be used for other human-induced loads than jumping. In order to model a specific load type, the phase lags φ_i can be varied freely as no specific values are given in the code [11]. Instead it is stated that the most critical values of φ_i should be used, but this procedure will not necessarily show a time history, which is representative for a specific load type. Therefore, in order to replicate a given human-induced load, a $(F(t), t)$-plot should be used to make a visual check, see Figure 7.1.

The load model given in the Danish National Annex only takes into account the first three load components, i.e. $i = 1, 2, 3$. This means that the summation term in Eq. (7.1) should only include three terms. The relevant parameters to define the load model is given in Table 7.1.

ACTIVITY	G [kN/m^2]	f_p [Hz]	α_1	α_2	α_3	ρ_1	ρ_2	ρ_3
Free possibility for movement, e.g. fitness center	0.5–4.0	0.5–3.0	1.6	1.0	0.2	1.0	0.3	0.03
Reduced possibility for movement, e.g. grand stands with seating	0.5–4.0	0.5–3.0	0.4	0.25	0.05	1.0	0.1	0.01
Walking. Humans are not walking in pace.	Should be assessed	1.6–2.4	0.4	0.1	0.06	0	0	0

Table 7.1: Parameters in load model from Danish National Annex to Eurocode 1 [11].

With respect to the phase lags φ_i, they are chosen in a way so the sinus curves corresponding to each of the three first load components have a positive peak at the same position. Therefore, the phase lags for the Eurocode model is chosen as: $\varphi_i = \{0 \quad -\pi/2 \quad \pi\}$ for $i = 1, 2, 3$. This principle is illustrated in Figure 7.2, which shows the sinus curve for each of the three first modes with the corresponding Fourier coefficients α_i as amplitudes.

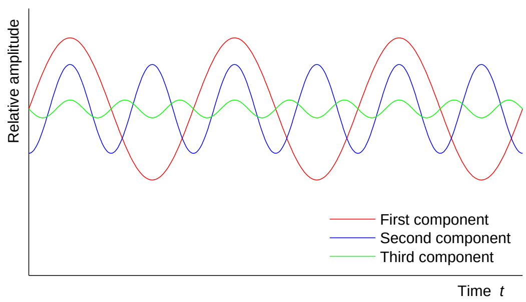

Figure 7.2: Sinus curves of three first load components

As movements of humans in the sports hall are unrestricted, the values in the first row of Table 7.1 must be used. According to the guidance in the National Annex, the jumping frequency f_p should be chosen within the stated interval, and when choosing a value for f_p, the lowest natural frequency of the construction f_1 should be kept in mind. A value, where resonance is obtained for one of the load harmonics, i.e. $i f_\mathrm{p} = f_1$, should be chosen for f_p. This could be a critical situation. Likewise, a situation where the maximum value of f_p is used should also be considered. Here, this corresponds to a jumping frequency at $f_\mathrm{p} = 3\,\mathrm{Hz}$. It should be pointed out that the load model does not take into account that humans are not able to jump with the exact same frequency during a load time history, see Appendix D.

The crowd reduction factor C_i, which is used in Eq. (7.1), is deduced from the situation, where N persons contribute to the load effect X_i of the i^{th} load harmonic. Each person is assumed to contribute with the load $F_{i,j}$:

$$X_i = a_1 F_{i,1} + a_2 F_{i,3} + \ldots + a_N F_{i,N} \tag{7.2}$$

The coefficients a_j, $j = 1, 2, \ldots, N$ are the load influence factors and depend on the relative influence of the corresponding load $F_{i,j}$. Thus, a load $F_{i,j}$ from a jumper is more critical when it is applied mid-span on a plate than near a support. Therefore, the values of a_j are calculated from the relevant shape function $\Phi(x, y)$ with its maximum value normalized to unity. The loads $F_{i,j}$ are assumed to be distributed with a coefficient of variation V_{F_i} and correlation coefficients ρ_i. Values for ρ_i are given in Table 7.1. From this the coefficient of variation of the load effect X_i is deduced from statistics [2] as given in Eq. (7.2):

$$V_{X_i} = V_{F_i} \sqrt{\rho_i + \frac{1-\rho_i}{N}\eta} \tag{7.3}$$

where

$$\eta = \frac{\frac{1}{N} \sum_{j=1}^{N} a_j^2}{\left(\frac{1}{N} \sum_{j=1}^{N} a_j \right)^2} \tag{7.4}$$

In accordance with the definition of a_j, the factor η takes into account the type of load distribution on the specific construction, and thereby that the load effect from a person is dependent on the position of the person. As a special case, $\eta = \pi^2/8$ for load harmonic components, which are in resonance with the first natural frequency f_1 [11]. Based on this, the so-called "effective" number of persons contributing to the load effect can be defined as: $N_\mathrm{e} = N/\eta$, and therefore, from Eq. (7.3), the crowd reduction factor is defined in the following way:

$$\begin{aligned} C_i &= \sqrt{\rho_i + \frac{1-\rho_i}{N}\eta} \\ &= \sqrt{\rho_i + \frac{1-\rho_i}{N_\mathrm{e}}} \end{aligned} \tag{7.5}$$

When using the load model given by Eq. (7.1) together with the parameters given in the Danish National Annex, Table 7.1, the crowd reduction factor C_i and thereby also η must be determined for each load case. Results for this method is shown in Chapter 8.

In addition to the load model of Eq. (7.1), a simplified procedure is also described in the Danish National Annex. This simplified procedure can be used with a minimum knowledge about the dynamical properties of a given construction, and from this the response can be estimated. Application of the simplified procedure is described in Section 8.1. In the simplified Eurocode procedure only Scenario 1 is considered, but also with jumping frequencies at $f_\mathrm{p} = 2.77\,\mathrm{Hz}$ and $f_\mathrm{p} = 3.00\,\mathrm{Hz}$ besides $f_\mathrm{p} = 2.08\,\mathrm{Hz}$ as stated in Table 6.1. This is due to recommendations in the Danish National Annex for a full serviceability limit state control [11].

7.2 Ellis & Ji Load Model

The load model proposed by Ellis & Ji [8] is like the Eurocode load model based on representing the jumping load by means of a Fourier series. To get the Ellis & Ji load model on the same form as the general expression in Eq. (7.1), the derivation shown in Eq. (7.6) is performed.

$$\begin{aligned} F(t) &= G\left(1.0+\sum_{i=1}^{\infty} a_i \cos\left(\frac{2\pi i}{T_\mathrm{p}}t\right)+\sum_{i=1}^{\infty} b_i \sin\left(\frac{2\pi i}{T_\mathrm{p}}t\right)\right) \\ &= G\left(1.0+\sum_{i=1}^{\infty} \alpha_i C_i \sin\left(2\pi i f_\mathrm{p} t+\varphi_i\right)\right) \end{aligned} \tag{7.6}$$

where

- G Static load of person per unit area [kN/m^2].
- C_i Crowd reduction factor for the i^{th} harmonic jumping load component. The crowd reduction factor is not specifically defined for the Ellis & Ji model, as it originally is designed for a single person. Hence, the following is assumed, $C_i = 1$.
- α_i Fourier coefficient for the i^{th} harmonic jumping load component, given as $\alpha_i = \sqrt{a_i^2 + b_i^2}$.
- φ_i Phase lag for the i^{th} harmonic jumping load component. $\varphi_i = \tan^{-1}\left(\frac{a_i}{b_i}\right)$ if $b_i > 0$, and $\varphi_i = \tan^{-1}\left(\frac{a_i}{b_i}+\pi\right)$ if $b_i < 0$.
- f_p Jumping frequency of persons, $f_\mathrm{p} = 1/T_\mathrm{p}$.

Unlike the Eurocode load model, no fixed Fourier coefficients are given for the Ellis & Ji load model. Instead, the Fourier coefficients α_i and the phase lags φ_i are determined based on the contact ratio, see Eq. (7.7),

$$c_\mathrm{r} = \frac{t_\mathrm{c}}{T_\mathrm{p}} \tag{7.7}$$

The meaning of the contact ratio can be seen in Figure 7.1. When the contact ratio of a jumping human is determined, it is used in Eq. (7.8) from which the Fourier coefficients and phase lags can be found as seen in connection with Eq. (7.6).

$$\begin{aligned} &\text{when} \quad 2 i c_\mathrm{r} = 1 \qquad i = 1,2,3,\ldots \\ &\text{then} \quad a_i = 0 \\ &\qquad\quad b_i = \frac{\pi}{2} \\ &\text{otherwise} \\ &\qquad a_i = 0.5\left(\frac{\cos((2ic_\mathrm{r}-1)\pi-1)}{2ic_\mathrm{r}-1}-\frac{\cos((2ic_\mathrm{r}+1)\pi-1)}{2ic_\mathrm{r}+1}\right) \\ &\qquad b_i = 0.5\left(\frac{\sin((2ic_\mathrm{r}-1)\pi)}{2ic_\mathrm{r}-1}-\frac{\sin((2ic_\mathrm{r}+1)\pi)}{2ic_\mathrm{r}+1}\right) \end{aligned} \tag{7.8}$$

The load model by Ellis & Ji is not limited when it comes to the number of considered load components as seen from Eq. (7.8), where $i = 1,2,3,\ldots$. This is another difference compared to the Eurocode load model. Of course, the number of considered load components should be limited to a reasonable value in order to reduce the needed computations. However, the number of important load components is dependent on the contact ratio c_r. For example, different Fourier coefficients found from the Ellis & Ji model is seen in Figure 7.3 as a function of contact ratio.

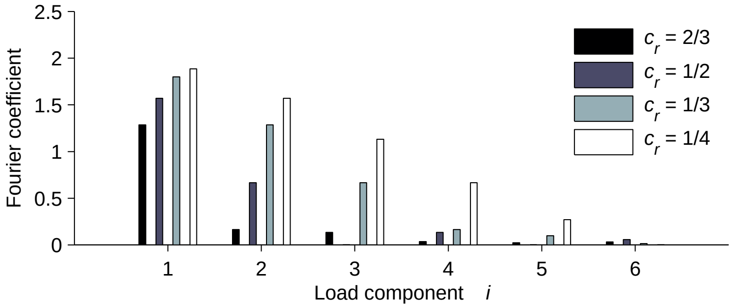

Figure 7.3: Fourier coefficients for Ellis & Ji load model.

A low contact ratio, e.g. $c_\mathrm{r} = 1/4$, means that more Fourier coefficients are relevant as their mutual magnitude is only slowly decreasing with the load component i. Also, lower contact ratios in general give higher Fourier coefficients, which from a physical point of view is obvious as the force from the jumper to the plate must be transferred in a shorter time interval. The situation is opposite at high contact ratios, where the few first Fourier coefficients are of importance, and afterwards a quick decrease in the magnitude is seen.

The matter of contact ratios is treated in an experiment with a single human jumping at different frequencies. A description and data treatment can be found in Appendix E.

In the following chapters 6 load components will be included for the Ellis & Ji load model.

7.2.1 Crowd Reduction Effect due to Modified Contact Ratio

When more persons are jumping simultaneously, the load amplitude will not scale linearly with the number of persons as they are not perfectly synchronized. The load amplitude per person can be reduced by increasing the contact ratio when the number of persons increase. An increase in the contact ratio c_r reflects that the persons do not have the exact same contact time, and hence the amplitude of one person is not scaled with the number of persons, but slightly reduced in comparison. Furthermore, as seen in Figure 7.3, a reduction in contact ratio also reduces the higher load components more than the first two load components. This difference in reduction for the different load components is also in agreement with reduction factor from the Eurocode load model.

To determine how to alter the contact ratio when the number of persons is changed, a Monte Carlo simulation has been conducted with the experimental results achieved in Appendix D and Appendix E. This means that both the accuracy of the jumping period T_p, and the contact ratio c_r are implemented as stochastic variables in the load calculation, where both variables are assumed normal distributed. To ease the computations, the two variables are assumed uncorrelated, which is probably unlikely to be true. The jumping frequency for the simulation is chosen to be $f_\mathrm{p} = 2\,\mathrm{Hz} \Rightarrow T_\mathrm{p} = 0.5\,\mathrm{s}$, and the standard deviation is found in Appendix D to be $S_{T_\mathrm{p}} = 0.037\,\mathrm{s}$. The simulation is run with the mean contact ratio of $c_\mathrm{r} = 0.46$ calculated in Appendix E with the corresponding standard deviation $S_{c_\mathrm{r}} = 0.03$.

To achieve replicable results for the $(N, c_\mathrm{r,eq})$ relation, it showed that it was necessary to make a simulation of $n = 10{,}000$ jumps for each N. The simulation was conducted with the MATLAB script `SimulationOfCrowds.m`. A comparison of the amplitude per person for 20 persons from the simulation and the reference for one person is seen in Figure 7.4.

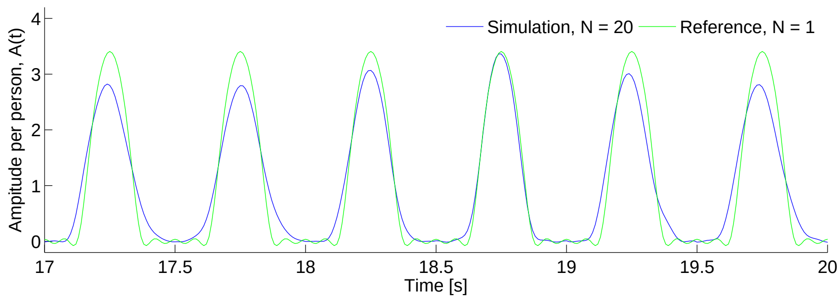

Figure 7.4: Comparison of average load amplitude per person for N = 20.

To calculate the amplitude per person, the amplitude functions from each person has been calculated, added to each other, and divided with the number of persons. The equivalent contact ratio is then calculated with the relation between contact ratio and the normalized maximum force ($K_p = F_{max}/G$) stated by Ellis & Ji [8], see Eq. (7.9).

$$c_r = \frac{\pi}{2K_p} \tag{7.9}$$

The resulting $(N, c_{r,eq})$ relation with a fitting curve for a contact ratio of $c_r = 0.46$ is seen in Figure 7.5.

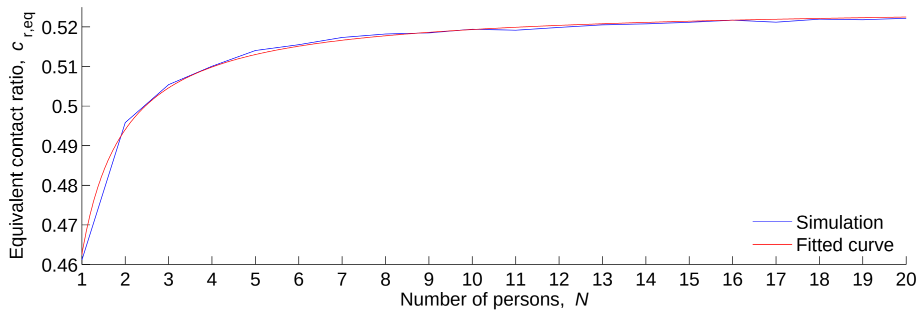

Figure 7.5: $(N, c_{r,eq})$ relation with fitting curve for a contact ratio of $c_r = 0.46$

The best fitting curve was found to be in the following form given by Eq. (7.10).

$$c_{r,eq} = c_{r,max} - \frac{1}{\beta \cdot N} \tag{7.10}$$

For a contact ratio of $c_r = 0.46$, the equivalent contact ratio can be calculated by Eq. (7.10) with $c_{r,max} = 8/7 \cdot c_r \approx 0.526$, and $\beta = 15.8$. The fitting curve is in good agreement with the simulation results as the square of the correlation coefficient is $R^2 = 0.9975$.

This means that for the number of persons used in the experiment, the equivalent contact ratios are as listed in Table 7.2.

PERSONS N	EQUIVALENT CONTACT RATIO $c_{r,eq}$
5	0.513
10	0.519
15	0.522
20	0.523

Table 7.2: Contact ratios for crowds.

As the crowd reduction is introduced through an increased contact ratio, the reduction factor in the load function in Eq. (7.6) is omitted, and the crowd reduction is implemented in the amplitude function $\alpha_i(c_{r,eq})$, so the load function becomes as seen in Eq. (7.11).

$$F(t) = G\left(1.0 + \sum_{i=1}^{\infty} \alpha_i(c_{r,eq}) \sin\left(2\pi i f_p t + \varphi_i\right)\right) \tag{7.11}$$

Although the load per person is reduced, it is still expected that the result of the simulation is overestimating the load. This is probably due to the fact that the simulation is based on the jumping accuracy of one person jumping alone on a steel plate, and may not represent the jumping accuracy at scenario with more persons jumping on a floor simultaneously. However, the values of the equivalent contact ratios found from this simulation will be used for the load calculation for the corresponding number of jumping persons in the following.

Chapter **8**

Response Analysis

Based on the preceding analyses of the dynamic properties of the construction and the two presented load models, the structural response can be analyzed. At first, a simple procedure from Eurocode for practical design purposes is applied. Hereafter an analytical solution to the governing differential equation of motion is used. Next, Newmark time integration is applied, which also makes it possible to model passive humans on the deck. Finally, the results from the ABAQUS *model is presented as this is the most advanced model as well as the experimental results.*

✦ ✦ ✦

8.1 Simplified Eurocode Procedure

When the response of a construction is wanted, the load model in Eq. (7.1) must be used together with a suitable dynamic model, which defines mass, stiffness, and damping properties of the construction. However, a simplified method is given in the Danish National Annex, which makes it possible to estimate an equivalent static load and structural acceleration to be used in practical design without having a complete dynamic model. In order to use this simplified method, the following should be fulfilled for the specific structure [13]:

1. The deflection due to static human loads has the same sign all over the structure.
2. Vibrations from one mode shape only.
3. The considered mode shape generally has vertical movements only, and they have the same sign all over the structure.
4. The considered mode shape is not coupled with any other shapes.
5. The structure has linear-elastic response behaviour.
6. Three load components are important.

Obviously, in the case of the TTD deck construction it is only reasonable to assume that assumption (5) is fulfilled in a general sense. If only the first mode shape is considered, also assumption (1), (2), and (3) is fulfilled, however, due to the closely spaced modes, more than the first mode shape are expected to influence the response for the deck, which cannot be considered in the simplified procedure.

Keeping these reservations in mind, the response of the deck is still estimated using the simplified method from the Danish National Annex to compare its result to more complicated approaches. The calculation is based on the first vibration mode. The simplified method is based on a spectral approach, and due to the findings in Hansen and Sørensen [13], an equivalent static load G_s can be estimated by:

$$G_s = G\,(1 + k_F) \tag{8.1}$$

where
$$k_F = a\sqrt{\sum_{i=1}^{3}(\alpha_i C_i H_i)^2} \tag{8.2}$$

Eq. (8.2) defines the load response factor k_F, where a is a response distribution factor depending on the number of dominating load components. When one load component dominates the response, $a = 1$, and otherwise, $a = 1.5$. H_i is the structural response factor for the i^{th} load component as given in Eq. (8.3):

$$H_i = \frac{1}{\sqrt{\left(1-\left(\frac{i f_p}{f_1}\right)^2\right)^2 + \left(\frac{\delta_s+\delta_p}{\pi}\frac{i f_p}{f_1}\right)^2}} \tag{8.3}$$

In Eq. (8.3) damping is introduced through the logarithmic decrement. According to the Danish National Annex, δ_s is the structural damping, and a value of $\delta_s \approx 0.05$ can be used for prestressed concrete. Likewise, δ_p is the human-induced logarithmic damping decrement, and a value of $\delta_p = 0.02$ can be used to make a conservative estimate [13]. The total logarithmic decrement is thus $\delta = 0.07$, which corresponds to a damping ratio of $\zeta = 1.114\,\%$. These values can be used, if no better suggestions are at hand. The relationships given in Eq.(8.4) exists between the logarithmic decrement and damping ratio [17].

$$\delta = 2\pi\frac{\zeta}{\sqrt{1-\zeta^2}} \qquad \zeta = \frac{\frac{\delta}{2\pi}}{\sqrt{1+\left(\frac{\delta}{2\pi}\right)^2}} \tag{8.4}$$

However, the damping ratio of the first mode has been estimated by measurements, where a value of $\zeta = 1.77\,\%$ was found, see Table 4.2, which corresponds to a logarithmic decrement of $\delta = 0.11$. Results for both values will be used in order to asses the influence of damping.

Besides the equivalent static load G_s, which can be used to asses the ultimate limit state, the acceleration of the structure is the most important parameter when it comes to assessing the serviceability limit state. According to the Danish National Annex [11], the standard deviation of the structural acceleration due to vertical dynamic loads can be determined as in Eq. (8.5). During vibration the numerical value of the acceleration is varying between 0 and a maximum value. Therefore, the magnitude of the acceleration can either be indicated by the maximum acceleration during an oscillation $a_{\max}$ or the standard deviation σ_a. According to the Danish National Annex [11], the standard deviation σ_a is used and this value should be compared with the limits given in Table 1.2.

$$\sigma_a = k_a\left(2\pi f_p\right)^2 u_p \tag{8.5}$$

u_p is the deflection due to the static human load G, and is thus found from a traditional static analysis. k_a is the acceleration response factor determined as:

$$k_a = \sqrt{\frac{1}{2}\sum_{i=1}^{3}\left(i^2\alpha_i C_i H_i\right)^2} \tag{8.6}$$

In the considered cases, where the simplified approach has been used, the deflection from static human load u_p is found using beam theory. A beam cross section according to half a TTD element including concrete topping is assumed, which is a conservative assumption as plate effects are disregarded. The load G in Table 7.1 on the assumed beam is recalculated from a area load to a line load by the width of half a TTD element.

The static deflection u_p is taken as the maximum deflection under static human loading. The principle of virtual work is utilized. A virtual point load $\delta Q = 1$ is applied at the position of the wanted deflection, and the product of load and deflection constitute the outer work. The inner work is found as the integral of the product of a virtual moment field $\delta M(x)$, and the real curvature given as $\kappa(x) = M(x)/EI$. The used expression is given in Eq. (8.7).

$$\delta Q \cdot u = \int_{\alpha} \frac{M(x)}{EI} \delta M(x) dx + \int_{\beta} \frac{M(x)}{EI} \delta M(x) dx + \int_{\gamma} \frac{M(x)}{EI} \delta M(x) dx \tag{8.7}$$

α, β, and γ are the lengths shown in Figure 8.1. A MATLAB-script, `Simplified_EC.m`, has been written, which calculates u at numerous positions along the length L_x and finds the maximum deflection u_p. In accordance with the predefined scenarios in Table 6.1, only Scenario 1 are examined for the simplified Eurocode model as only one mode can be addresses in this method. Acceleration values are taken from the midpoint of the deck, see Figure 8.2.

In both cases, $EI = 2.44 \times 10^9\,\mathrm{Nm}^2$ is used in the calculations according to the tuned values found in Chapter 5. In all calculations it is assumed that the weight of one human can be set to 0.75 kN. Three different jumping frequencies f_p have been used. The resonance frequency-case is defined so the third load component hits the natural frequency, $3 \cdot f_p = f_1$, whereas the maximum frequency-case is defined from the maximum allowable jumping frequency given in Table 7.1. These two cases are mandatory according to the Danish National Annex. The last situation, the reference frequency-case, is defined so the fourth load component would hit the natural frequency, $4 \cdot f_p = f_1$. However, as the fourth load component is disregarded in the Eurocode load model, the reference frequency-case serves merely as a reference situation.

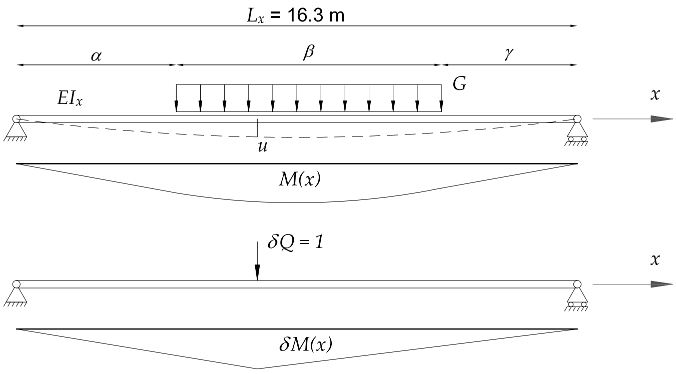

Figure 8.1: Beam problem when using principle of virtual work.

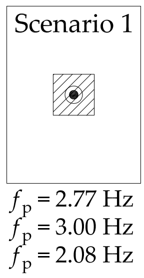

Figure 8.2: Load area and output point of acceleration values.

Results from the simplified procedure of the Danish National Annex are given in Table 8.1 for a logarithmic decrement of $\delta = 0.07$, and in Table 8.2 for a logarithmic decrement of $\delta = 0.11$. This corresponds to the suggested value in the Danish National Annex and the measured value, respectively.

The resonance situation is seen to be the most critical as the third load component hits the first natural frequency exactly, and therefore a large dynamic amplification is found. However, the acceleration is still found acceptable as $\sigma_a = 6.80$ % and $\sigma_a = 4.39$ % of g. The case with maximum jumping frequency is less critical. Finally, the reference situation using a jumping frequency at $f_p = 2.08\,\mathrm{Hz}$ is not critical at all according to this simplified model as the fourth load component is disregarded in the Eurocode model. The magnitude of the dynamic amplification is most easily seen from the load response factor k_F, and the acceleration response factor k_a.

The values in Table 8.1 and Table 8.2 are based on the static human load of $G = 600\,\mathrm{N/m}^2$. Therefore, the influence of a varying G, and thus number of humans, is examined in Figure 8.3 and Figure 8.4. The size of the load area is maintained. By comparison of the two graphs, it is

PARAMETERS $\alpha = \gamma = 5.65$ m, $\beta = 5.00$ m		RESONANCE FREQUENCY	MAXIMUM FREQUENCY	REFERENCE FREQUENCY
Lowest natural frequency	f_1 [Hz]	8.30	8.30	8.30
Static human load	G [kN/m^2]	0.60	0.60	0.60
Number of persons	N	20	20	20
Crowd reduction factor	C_i, $i = 1,2,3$	(1.00, 0.58, 0.30)	(1.00, 0.58, 0.28)	(1.00, 0.58, 0.28)
Structural response factor	H_i, $i = 1,2,3$	(1.13, 1.80, 44.9)	(1.15, 2.09, 5.64)	(1.07, 1.33, 2.28)
Deflection from static load	u_p [mm]	0.13	0.13	0.13
Jumping frequency	f_p [Hz]	2.77	3.00	2.08
Contribution from 1$^{\text{st}}$ component	$(\alpha_1 C_1 H_1)^2$	3.24	3.39	2.91
Contribution from 2$^{\text{nd}}$ component	$(\alpha_2 C_2 H_2)^2$	1.09	1.47	0.60
Contribution from 3$^{\text{rd}}$ component	$(\alpha_3 C_3 H_3)^2$	7.24	0.10	0.02
Response distribution factor	a	1.0	1.5	1.5
Load response factor	k_F	3.40	3.34	2.82
Equivalent static load	G_s [kN/m^2]	2.64	2.60	2.29
Contribution from 1$^{\text{st}}$ component	$\left(1^2 \alpha_1 C_1 H_1\right)^2$	3.24	3.39	2.91
Contribution from 2$^{\text{nd}}$ component	$\left(2^2 \alpha_2 C_2 H_2\right)^2$	17.36	23.49	9.56
Contribution from 3$^{\text{rd}}$ component	$\left(3^2 \alpha_3 C_3 H_3\right)^2$	586.30	8.09	1.35
Acceleration response factor	k_a	17.42	4.18	2.63
Stadard deviation of acceleration	σ_a [% of g]	6.80	1.92	0.58
Maximum acceleration	a_max [m/s^2]	0.94	0.27	0.08

Table 8.1: Results from simplified procedure, $\delta = 0.07$, Eurocode recommendation.

PARAMETERS $\alpha = \gamma = 5.65$ m, $\beta = 5.00$ m		RESONANCE FREQUENCY	MAXIMUM FREQUENCY	REFERENCE FREQUENCY
Lowest natural frequency	f_1 [Hz]	8.30	8.30	8.30
Static human load	G [kN/m^2]	0.60	0.60	0.60
Number of persons	N	20	20	20
Crowd reduction factor	C_i, $i = 1,2,3$	(1.00, 0.58, 0.30)	(1.00, 0.58, 0.28)	(1.00, 0.58, 0.28)
Structural response factor	H_i, $i = 1,2,3$	(1.12, 1.80, 28.2)	(1.15, 2.09, 5.56)	(1.07, 1.33, 2.28)
Deflection from static load	u_p [mm]	0.13	0.13	0.13
Jumping frequency	f_p [Hz]	2.77	3.00	2.08
Contribution from 1$^{\text{st}}$ component	$(\alpha_1 C_1 H_1)^2$	3.24	3.39	2.91
Contribution from 2$^{\text{nd}}$ component	$(\alpha_2 C_2 H_2)^2$	1.08	1.47	0.60
Contribution from 3$^{\text{rd}}$ component	$(\alpha_3 C_3 H_3)^2$	2.87	0.10	0.02
Response distribution factor	a	1.0	1.5	1.5
Load response factor	k_F	2.68	3.34	2.82
Equivalent static load	G_s [kN/m^2]	2.21	2.60	2.29
Contribution from 1$^{\text{st}}$ component	$\left(1^2 \alpha_1 C_1 H_1\right)^2$	3.24	3.39	2.91
Contribution from 2$^{\text{nd}}$ component	$\left(2^2 \alpha_2 C_2 H_2\right)^2$	17.34	23.45	9.53
Contribution from 3$^{\text{rd}}$ component	$\left(3^2 \alpha_3 C_3 H_3\right)^2$	232.20	7.87	1.33
Acceleration response factor	k_a	11.24	4.17	2.62
Standard deviation of acceleration	σ_a [% of g]	4.39	1.91	0.58
Maximum acceleration	a_max [m/s^2]	0.61	0.27	0.08

Table 8.2: Results from simplified procedure, $\delta = 0.11$, measured value.

seen that the damping is quite important. Due to this simplified procedure, the change in logarithmic decrement from $\delta = 0.07$ to $\delta = 0.11$ means that G can be increased from approximately $1\,\mathrm{kN/m^2}$ to $1.6\,\mathrm{kN/m^2}$, before a critical situation occur at $f_\mathrm{p} = 2.77\,\mathrm{Hz}$. Also, only the situation at $f_\mathrm{p} = 2.77\,\mathrm{Hz}$ is affected by the change in damping, while at the two remaining frequencies, the response is almost unchanged. This is also seen by comparing Figure 8.5 and Figure 8.6.

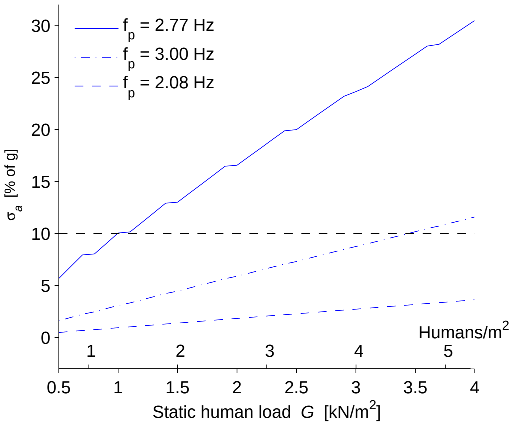

Figure 8.3: Variation of σ_a with G, $\delta = 0.07$.

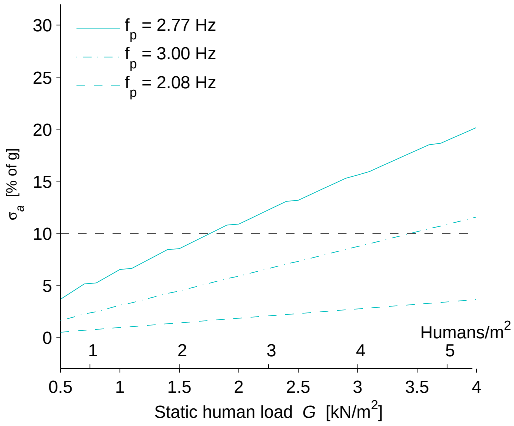

Figure 8.4: Variation of σ_a with G, $\delta = 0.11$.

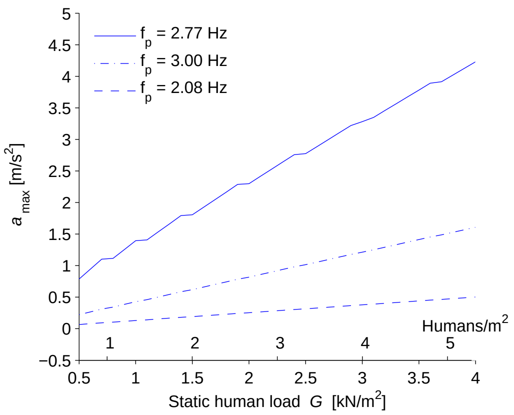

Figure 8.5: Variation of a_max with G, $\delta = 0.07$.

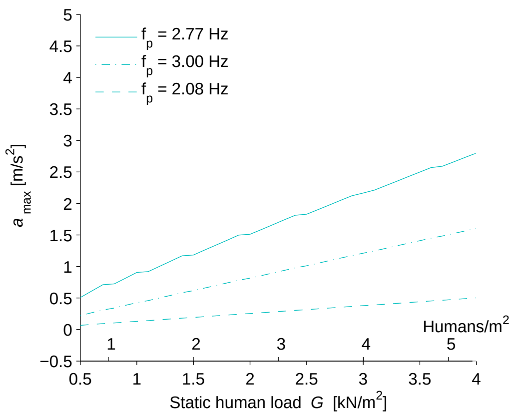

Figure 8.6: Variation of a_max with G, $\delta = 0.11$.

The figures reveal that if a jumping frequency at $f_\mathrm{p} = 2.77\,\mathrm{Hz}$ is chosen, large accelerations can be expected, but at other frequencies, where resonance is not achieved, the accelerations seem less critical unless for a very dense crowd. However, it should be mentioned that a natural boundary exist due to the number of people per square metre, and with a very dense crowd it must be expected that the synchronization between people suffers.

8.2 Analytical Solution of Differential Equation

The Eurocode load model and the load model by Ellis & Ji are used in connection with an analytical solution to the governing differential equation of a single degree of freedom system. In connection with the analytical solution, modal decomposition is utilized, and it is assumed that the response is governed by the three first modes of vibration of a plate model.

8.2.1 Modal Decomposition and General Solution

When assuming that the response is governed by the three first modes of vibration, the displacement $u(x, y, t)$ at an arbitrary point on the plate can be found as stated in Eq. (8.8) [18]. This principle also holds for the velocity $v(x, y, t) = \dot{u}(x, y, t)$ and the acceleration $a(x, y, t) = \ddot{u}(x, y, t)$.

$$u(x, y, t) = \sum_{n=1}^{3} \Phi_{1n}(x, y)\; q_n(t) \tag{8.8}$$

where

$\Phi_{1n}(x, y)$	Shape function of n^{th} mode. $\Phi_{1n} = \sin\left(\pi \frac{x}{L_x}\right) \sin\left(n\pi \frac{y}{L_y}\right)$.
$q_n(t)$	Modal coordinate.

The shape function $\Phi_{1n}(x, y)$ is used to specify a position, where the response is wanted. It should be noticed that in the formulation of the shape function, only variation of the sine term is possible in the y-direction, as the three first modes corresponds to one, two, and three half sine waves in this direction, e.g. see Figure 3.10. Each mode is considered as a single degree of freedom system (SDOF system) using the corresponding modal mass m_n, modal stiffness $k_n = \omega_n^2 m_n$, modal damping $c_n = 2\zeta_n \omega_n m_n$, and modal force $f_{1n}(t)$. Three SDOF oscillators have been depicted in Figure 8.7 representing the three first modes of vibration.

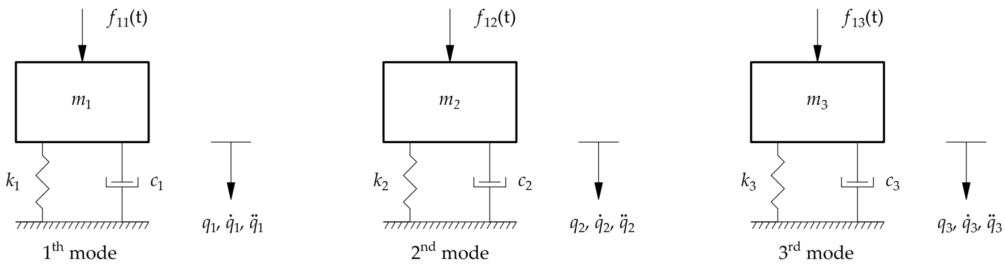

Figure 8.7: SDOF systems.

The modal coordinates $q_n(t)$ are found using a solution of the differential equation of a SDOF system. This differential equation is given in Eq. (8.9).

$$m_n \ddot{q}_n + 2\zeta_n \omega_n m_n \dot{q}_n + \omega_n^2 m_n q_n = f_{1n}(t) \tag{8.9}$$

where

q_n	Modal coordinate of the n^{th} mode.
m_n	Modal mass calculated from Eq. (A.7) in Appendix A.
ζ_n	Modal damping ratio. These are found in Chapter 4 from a measured acceleration signal.
ω_n	Natural frequency of the n^{th} mode, target values given in Table 5.1.
$f_{1n}(t)$	Modal load of time varying forcing function $F(t)$.

The time series of the modal load $f_{1n}(t)$ is calculated with Eq. (8.10a) and the stationary modal load g_{1n} from the physical static load G with Eq. (8.10b). By this, the modal load takes the position of the load on the deck in relation to the mode of interest into account.

$$f_{1n}(t) = \int_{L_x} \int_{L_y} \Phi_{1n}(x, y)\; F(t)\; dy dx \tag{8.10a}$$

$$g_{1n} = \int_{L_x} \int_{L_y} \Phi_{1n}(x, y)\; G\; dy dx \tag{8.10b}$$

The complete solution of Eq. (8.9) consists of the transient or complementary part, which is dependent on the initial conditions, as well as the stationary or particular solution, which is force dependent. According to Nielsen [17], the complementary and particular solution can be stated as in Eq. (8.11). Again, the solutions are stated in modal coordinates indicating one solution for each mode.

$$q_n(t) = q_{n,\mathrm{com}}(t) + q_{n,\mathrm{par}}(t) \qquad \text{is constituted of}$$
$$\begin{cases} q_{n,\mathrm{com}}(t) = A_{n,\mathrm{com}}\, e^{-\zeta_n \omega_n t} \cos\left(\left(\omega_n \sqrt{1-\zeta_n^2}\right) t - \Psi_{n,\mathrm{com}}\right) \\[2ex] q_{n,\mathrm{par}}(t) = \dfrac{g_{1n}}{k_n} + \displaystyle\sum_{i=1}^{I} \left|X_{n,i}\right| \cos\left(\omega_{\mathrm{p},i}\, t - \Psi_{n,i,\mathrm{par}}\right) \end{cases} \tag{8.11}$$

where

$A_{n,\mathrm{com}}$, $\Psi_{n,\mathrm{com}}$	Integration parameters found from initial conditions, see Eq. (8.12).
k_n	Modal stiffness, found as $k_n = \omega_n^2 m_n$ or alternatively as in Eq. (A.7) in Appendix A.
$\omega_{\mathrm{p},i}$	Circular forcing frequency for the i^{th} load component.
$\left\|X_{n,i}\right\|$	Force amplitude, see Eq. (8.13) and Eq. (8.14).
$\Psi_{n,i,\mathrm{par}}$	Phase, see Eq. (8.13) and Eq. (8.14).
i, I	Index of load component and total number of load components.

According to the considered load components in each load model, $I = 3$ for the Eurocode model, and $I = 6$ for the Ellis & Ji model. The integration parameters $A_{n,\mathrm{com}}$ and $\Psi_{n,\mathrm{com}}$ to use in the complementary solution is found from the initial conditions: $q_{0,n}(0) = \dot{q}_{0,n}(0) = 0$, see Eq. (8.12). As seen, Eq. (8.12) has two equations with two unknowns, and this system of equations is solved for each mode n. This problem is treated in the MATLAB-file `Newmark_analytical_3modes.m`.

$$\begin{aligned} q_{0,n} &= \frac{g_{1n}}{k_n} + \sum_{i=1}^{I} \left|X_{n,i}\right| \cos\left(\Psi_{n,i,\mathrm{par}}\right) + A_{n,\mathrm{com}} \cos\left(\Psi_{n,\mathrm{com}}\right) \\ \dot{q}_{0,n} &= \sum_{i=1}^{I} \left|X_{n,i}\right| \omega_{\mathrm{p},i} \sin\left(\Psi_{n,i,\mathrm{par}}\right) + A_{n,\mathrm{com}} \left(\omega_n \sqrt{1-\zeta_n^2}\right) \left(\sin\left(\Psi_{n,\mathrm{com}}\right) - \frac{\zeta_n}{\sqrt{1-\zeta_n^2}} \cos\left(\Psi_{n,\mathrm{com}}\right) \right) \end{aligned} \tag{8.12}$$

The force amplitude $\left|X_{n,i}\right|$ and phase $\Psi_{n,i,\mathrm{par}}$ in the particular solution are found as given in Eq. 8.13. Calculations can be found in `Newmark_analytical_3modes.m`.

$$\begin{aligned} \left|X_{n,i}\right| &= \frac{\left|F_{n,i}\right|}{m_n \sqrt{\left(\omega_n^2 - \omega_{\mathrm{p},i}\right)^2 + 4\zeta_n^2 \omega_n^2 \omega_{\mathrm{p},i}^2}} \\ \Psi_{n,i,\mathrm{par}} &= \tan^{-1}\left(\frac{2\zeta_n \omega_n \omega_{\mathrm{p},i}}{\omega_n^2 - \omega_{\mathrm{p},i}^2}\right) + \theta_i \end{aligned} \tag{8.13}$$

The parameters $\left|F_{n,i}\right|$ and θ_i are found from the two used load models. Here, it must be considered that Eq. (8.11) and Eq. (8.13) assume a forcing function $f_{\mathrm{orig}}(t)$ of the form given by Eq. (8.14). By rewriting the original form of the forcing function, $\left|F_{n,i}\right|$ and θ_i can be defined in relation to the two load models. It should be noticed that index i in Eq. (8.14) is shifted to index m, so this is not confused with the imaginary number i.

$$
\begin{aligned}
f_{\text{orig}}(t) &= g_{1n} + \sum_{m=1}^{I} \text{Re}\Big(\big|F_{n,m}\big|\; e^{-i\theta_m}\; e^{i\omega_{\text{p},m} t}\Big) \\
&= g_{1n} + \sum_{m=1}^{I} \text{Re}\Big(\big(\cos(\theta_m) - i\sin(\theta_m)\big)\big(\cos(\omega_{\text{p},m} t) - i\sin(\omega_{\text{p},m} t)\big)\Big) \\
&= g_{1n} + \sum_{m=1}^{I} \big|F_{n,m}\big|\big(\cos(\theta_m)\cos(\omega_{\text{p},m} t) + \sin(\theta_m)\sin(\omega_{\text{p},m} t)\big) \\
&= g_{1n} + \sum_{m=1}^{I} \big|F_{n,m}\big|\cos\big(\omega_{\text{p},m} t - \theta_m\big) \\
&= g_{1n}\left(1 + \sum_{m=1}^{I} \big|F_{n,m}\big|\sin\left(\omega_{\text{p},m} t + \left(\frac{\pi}{2} - \theta_m\right)\right)\right)
\end{aligned}
\tag{8.14}
$$

By comparing the last result of Eq. (8.14) with the general expression of the load model given by Eq. (7.1), the following identifications can be made: $\big|F_{n,i}\big| = g_{1n}\alpha_i C_i$ and $\theta_i = \frac{\pi}{2} - \varphi_i$, as the index is shifted back from m to i.

8.2.2 Results from Analytical Solution

The results of the analytical solution are presented for the two load models. In the analytical approach all scenarios defined in Table 6.1 have been considered except from the situations with passive persons. Therefore, this gives two main issues to be considered:

- Control of serviceability limit state with resonance jumping for three first modes.
- Parameter study of crowd reduction effect.

Only the stationary response is considered, as the transient response is quickly dissipated. To illustrate this, the transient response of Scenario 1 with 20 jumping humans is shown in Figure 8.8 for the Eurocode load model. The shown acceleration signal is taken from the middle of the plate, i.e. $\big(x, y\big) = \big(L_\text{x}/2, L_\text{y}/2\big)$.

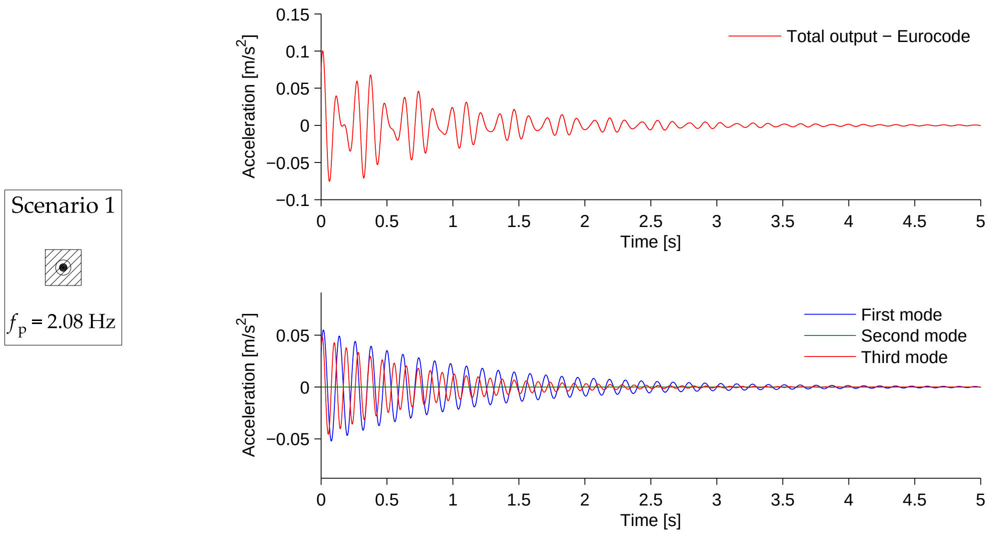

Figure 8.8: Transient motion calculation from Eurocode load model.

As seen, an initial impact on the floor will be almost totally dissipated within approximately 3 seconds, whereafter the stationary motion will be dominating. This situation is illustrated in Figure 8.9, where the complete solution with both the transient and stationary response included is compared against the stationary response. Again, the acceleration at $(x, y) = (L_x/2, L_y/2)$ in Scenario 1 with 20 jumping humans is used, but only for the Ellis & Ji load model.

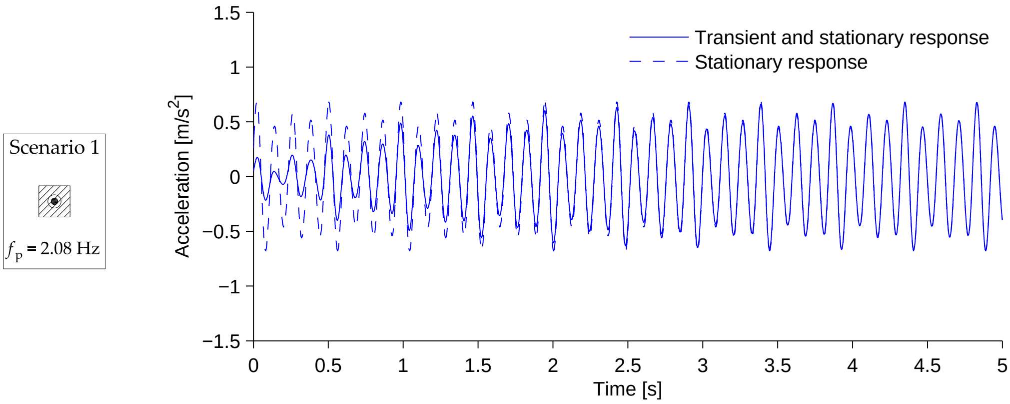

Figure 8.9: Comparison of solutions.

Obviously, the transient response is only of importance during the first few seconds of the time series, and becomes ignorable as the total time series lasts at least 30 seconds as in the experiments. Henceforth, the transient response is disregarded, and only values for the stationary response are shown.

Control of Serviceability Limit State

The calculated maximum acceleration values and root-mean-square values are plotted for the two load models in Figure 8.10 and Figure 8.11, respectively. These results can be used to evaluate the serviceability limit state.

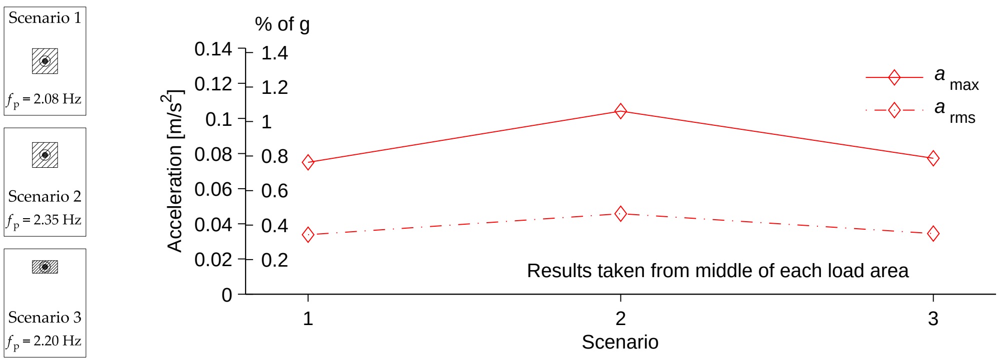

Figure 8.10: a_{max} and a_{rms} for the Eurocode model.

Here, it should be kept in mind that the Eurocode model takes the crowd reduction effect into account by the factor C_i, whereas in the original Ellis & Ji model, the load is not reduced due to the crowd reduction effect, and thus $C_i = 1$ for all load components. Therefore, in order to incorporate the crowd reduction effect in the model by Ellis & Ji, an equivalent contact ratio $c_{r,eq}$ is used as explained in Section 7.2.1. With 20 jumping humans, $N = 20$, an equivalent contact ratio of $c_{r,eq} = 0.52$ is found.

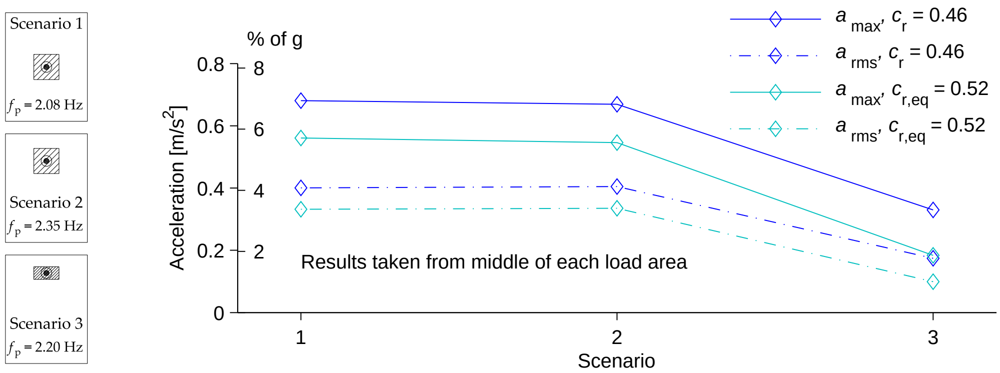

Figure 8.11: a_{max} and a_{rms} for the Ellis & Ji model.

The found acceleration response for the two load models are very different. The accelerations from the Eurocode model are in an approximate sense only 10 % of the accelerations from the Ellis & Ji load model. This pronounced difference is due to the fact that the Eurocode load model only takes the three first load components into account, whereas four is needed for the load to reach resonance for the chosen jumping frequenct. As seen from Figure 8.11, an equivalent contact ratio reduces the accelerations with approximately 18 % for the two first scenarios, and with 40 % for the third scenario.

Parameter Study of Crowd Reduction Effect

The acceleration response as a function of weight of jumpers is shown in Figure 8.12. The weight corresponding to the number of jumpers in Table 6.1 is marked with a square. Again, two sets of results have been shown for the Ellis & Ji load model, as one of them uses the equivalent contact ratio given in Eq. (7.10).

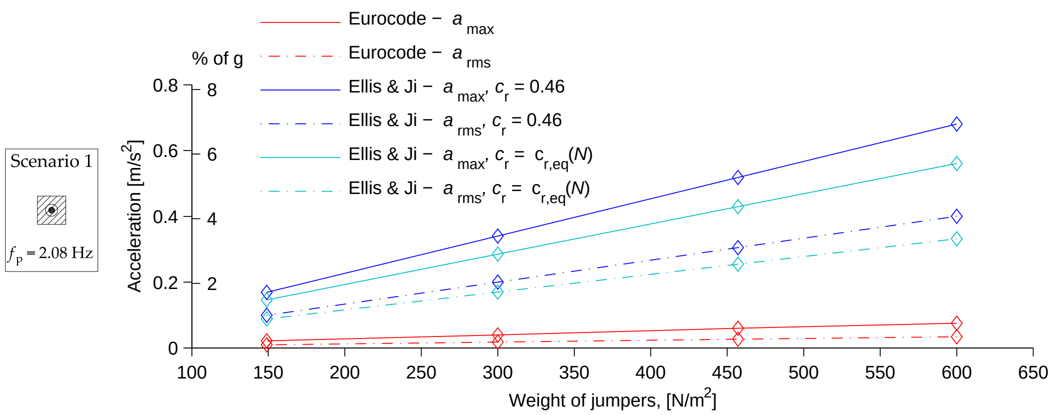

Figure 8.12: Scenario 1, response with varying number of humans jumping.

In Figure 8.13 the acceleration signals for 20 and 5 jumping humans are shown using the Ellis & Ji model with an equivalent contact ratio. Comparing the maximum accelerations at 0.15 m/s^2 and 0.56 m/s^2, respectively, it is obvious that the increase in acceleration is not linearly proportional with the number of people. Although, the reduction at 20 jumping humans is not significant as a value of 0.60 m/s^2 could be expected without taking the crowd size into consideration.

In all presented results, the relatively large difference between the Eurocode results and the Ellis & Ji results is noticeable. A comparison of the displacement plots shown in Figure 8.14 for Scenario 1 illustrates the situation.

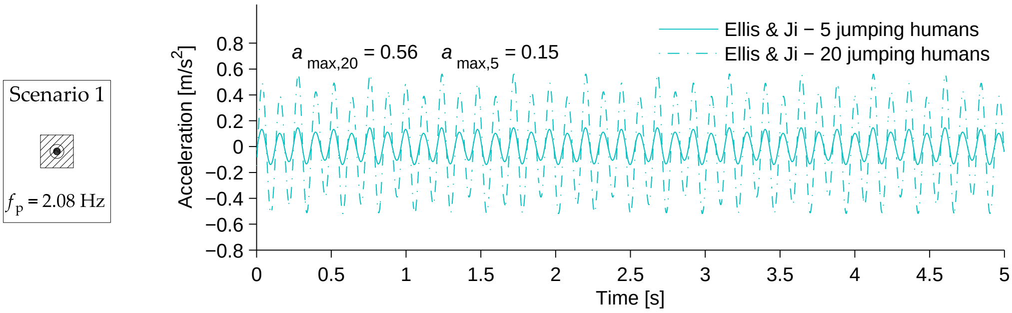

Figure 8.13: Comparison of accelerations.

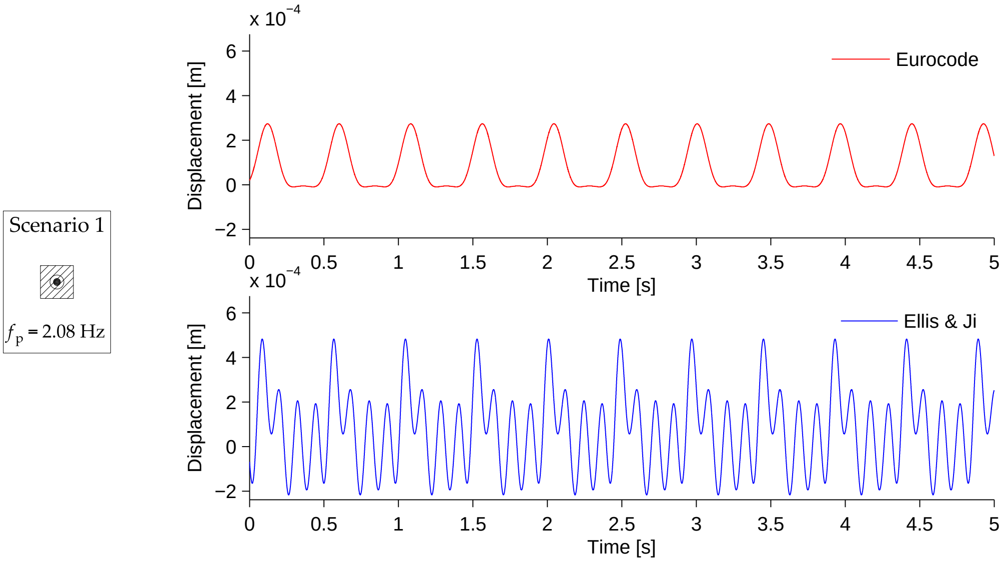

Figure 8.14: Comparison of displacement plots.

For the displacements calculated with the Eurocode load model, no dynamic effects can be observed. Instead, the displacement curve has the same shape as the load curve, where each "bump" corresponds to the humans hitting the deck. On the contrary, the displacement curve calculated with the Ellis & Ji load model shows clear dynamic effects, as oscillations are performed between each load impact.

8.3 Newmark Time Integration

Newmark time integration is used as a supplement to the analytical solution of the differential equation. Again, modal decomposition is assumed as described in Section 8.2.1, and Newmark time integration is used to solve the equation of motion in modal coordinates, Eq. (8.9). However, as the results for the analytical solution and Newmark time integration are completely similar, when making calculation for control of the serviceability limit state and the parameter study of crowd reduction effect, these results are not presented again. Instead, the Newmark time integration will focus on: Parameter study of human damping effect.

Passive persons can be modelled in various ways. In the literature numerous suggestions are given, for example rigid mass attachment, mass-spring systems, and mass-spring-damper systems have been suggested to model the presence of passive humans on a construction. It is now accepted that a mass-spring-damper model is the most appropriate model [22]. Based on this, SDOF systems are added on top of the structural systems shown in Figure 8.7. The principle is shown in Figure 8.15, where each extra system models a passive human.

A dynamic description of the passive human system must be applied, and here a model by Zheng and Brownjohn [22] is used. They state approximate parameters of the fundamental frequency and damping ratio of a human to $f_\mathrm{h} = 5.24\,\mathrm{Hz}$ and $\zeta_\mathrm{h} = 39\,\%$. The modal mass of a passive human is calculated from the assumed mass of a single person $G_1 = 75\,\mathrm{kg}$. By use of the shape function $\Phi_{1n}(x, y)$, the position of the passive human can be chosen freely over the floor, see Eq. (8.15).

$$m_{\mathrm{h}n} = \Phi_{1n}(x,y)G_1 \tag{8.15}$$

The modal stiffness $k_{\mathrm{h}n}$ and modal damping coefficients $c_{\mathrm{h}n}$ for the human SDOF model can be determined from Eq. (8.16).

$$k_{\mathrm{h}n} = \left(2\pi f_\mathrm{h}\right)^2 m_{\mathrm{h}n} \tag{8.16a}$$

$$c_{\mathrm{h}n} = 2\zeta_\mathrm{h}\left(2\pi f_\mathrm{h}\right) m_{\mathrm{h}n} \tag{8.16b}$$

When more passive people are present on the floor, the dynamic model can be expanded correspondingly by adding more SDOF systems, see Figure 8.15.

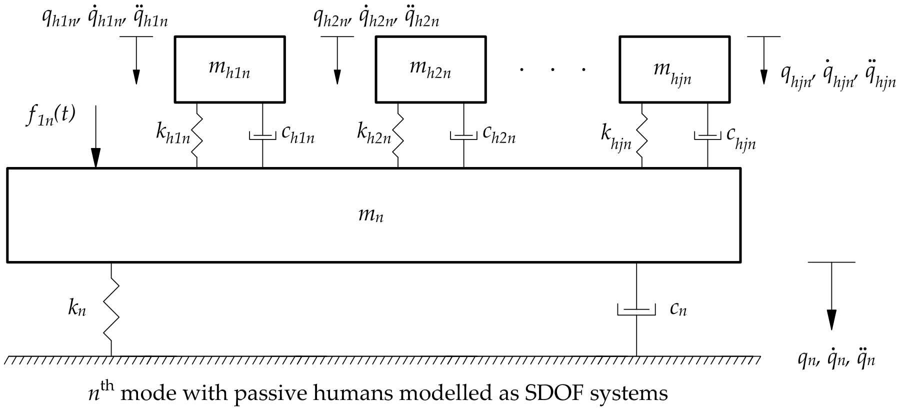

Figure 8.15: First vibration mode with passive humans.

As indicated in Figure 8.15, each passive human can have its own set of dynamic parameters, which are not only dependent on their position on the floor, as in reality the weight, frequency and damping ratio will vary from person to person. These parameters can be a complex study to identify, why the weight of a single person is assumed to be constant at $G_1 = 75\,\mathrm{kg}$, and the parameters suggested by Zheng and Brownjohn are assumed to apply for all persons. With the dynamic models put up, the system can be described by the matrix formulation:

$$\mathbf{M}_n\ddot{\mathbf{q}}_n + \mathbf{C}_n\dot{\mathbf{q}}_n + \mathbf{K}_n\mathbf{q}_n = \mathbf{f}_{1n}(t) \tag{8.17}$$

For the n^{th} of the three first modes, and with j passive humans, the matrices of Eq. (8.17) are given as:

$$\mathbf{M}_n = \begin{bmatrix} m_n & 0 & \cdots & 0 \\ 0 & m_{\mathrm{h}1n} & \cdots & 0 \\ \vdots & \vdots & \ddots & \vdots \\ 0 & 0 & \cdots & m_{\mathrm{h}jn} \end{bmatrix} \qquad \mathbf{C}_n = \begin{bmatrix} c_n + c_{\mathrm{h}1n} + \cdots + c_{\mathrm{h}jn} & -c_{\mathrm{h}1n} & -c_{\mathrm{h}2n} & \cdots & -c_{\mathrm{h}jn} \\ -c_{\mathrm{h}1n} & c_{\mathrm{h}1n} & 0 & \ddots & 0 \\ -c_{\mathrm{h}2n} & 0 & c_{\mathrm{h}2n} & \ddots & \vdots \\ \vdots & \ddots & \ddots & \ddots & 0 \\ -c_{\mathrm{h}jn} & 0 & 0 & 0 & c_{\mathrm{h}jn} \end{bmatrix}$$

$$\mathbf{K}_n = \begin{bmatrix} k_n + k_{\mathrm{h}1n} + \cdots + k_{\mathrm{h}jn} & -k_{\mathrm{h}1n} & -k_{\mathrm{h}2n} & \cdots & -k_{\mathrm{h}jn} \\ -k_{\mathrm{h}1n} & k_{\mathrm{h}1n} & 0 & \ddots & 0 \\ -k_{\mathrm{h}2n} & 0 & k_{\mathrm{h}2n} & \ddots & \vdots \\ \vdots & \ddots & \ddots & \ddots & 0 \\ -k_{\mathrm{h}jn} & 0 & 0 & 0 & k_{\mathrm{h}jn} \end{bmatrix} \quad \mathbf{f}_{1n}(t) = \begin{bmatrix} f_{1n}(t) \\ 0 \\ 0 \\ \vdots \\ 0 \end{bmatrix} \quad \mathbf{q}_n = \begin{bmatrix} q_n \\ q_{\mathrm{h}1n} \\ q_{\mathrm{h}2n} \\ \vdots \\ q_{\mathrm{h}jn} \end{bmatrix}$$

The motion of the system can now be solved using Newmark time integration which is described in more detail in Appendix F. It should be noticed that only the modal coordinate q_n, which describes the motion of the structure, is used in the modal superposition given by Eq. (8.8) to find the response of the deck. The other degrees of freedom, which describes the motion of each individual person, serves merely as auxiliary degrees of freedom.

For the sake of simplicity, it is assumed that all passive humans are placed at the same point. This means that for Scenario 1, all passive humans are assumed to be placed in the middle of the deck, and therefore, the shape function $\Phi_{1n}\left(L_{\mathrm{x}}/2, L_{\mathrm{y}}/2\right)$ is used to calculate the modal mass of all passive humans according to Eq. (8.15).

8.3.1 Results from Newmark Time Integration

The time step is chosen to $\Delta t = 1/5500$ in order to minimize period elongation, and the parameters of the Newmark algorithm (γ,β) are set to $\left(\frac{1}{2},\frac{1}{4}\right)$, thus introducing no numerical damping [18], see Appendix F.

Parameter Study of Human Damping Effect

The calculated maximum and root-mean-square accelerations with passive humans on the floor can be seen in Figure 8.16. The calculations are based on 5 jumping humans, while the passive humans are varied according to 0, 5, 10, and 15. As seen in the figure, attenuation of the acceleration level is not seen for the Eurocode load model, but is present for the Ellis & Ji load model. Here, the acceleration level with 15 passive humans is only ≈ 83 % of the value with 0 passive human. The results from the Eurocode load model is not affected, as no appreciable dynamic effects are present, see also Figure 8.14. As a consequence, the added damping from the passive humans is not influencing the response, which is primarily governed by the stiffness properties rather than the inertial and damping properties.

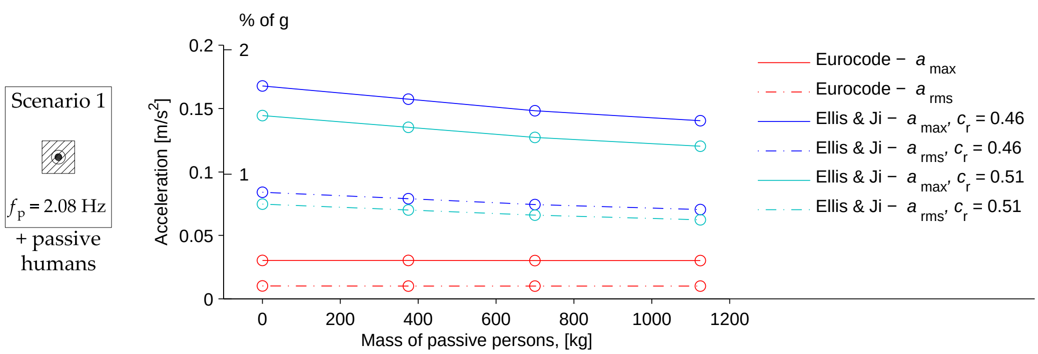

Figure 8.16: Acceleration with passive humans, 5 jumping humans.

The modal damping ratios have been calculated with passive humans present on the deck. An impact load is assumed to excite the system, and the logarithmic decrement method is applied to the free decay for each mode, respectively. The modal damping ratios calculated from the

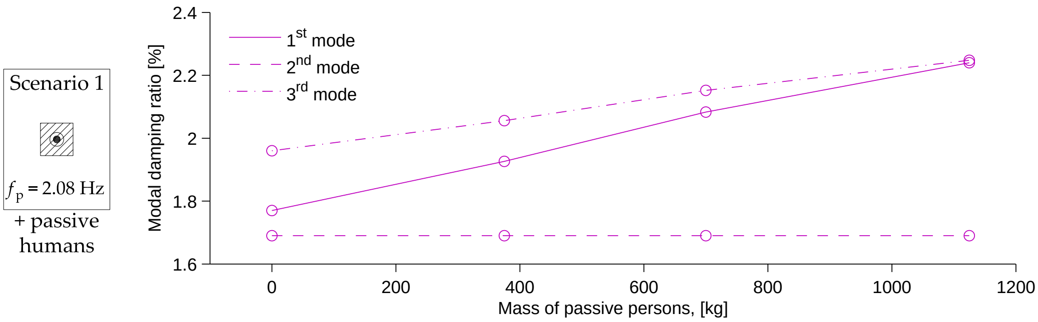

Figure 8.17: Variation of modal damping ratio.

logarithmic decrement method can be seen in Figure 8.17. The position of the passive humans is reflected in the increase in modal damping ratio.

Figure 8.18 shows two examples of acceleration signals with a free decays for the first mode with 0 and 15 passive humans. The decay is seen to be more rapid for 15 passive persons than for 0 passive persons.

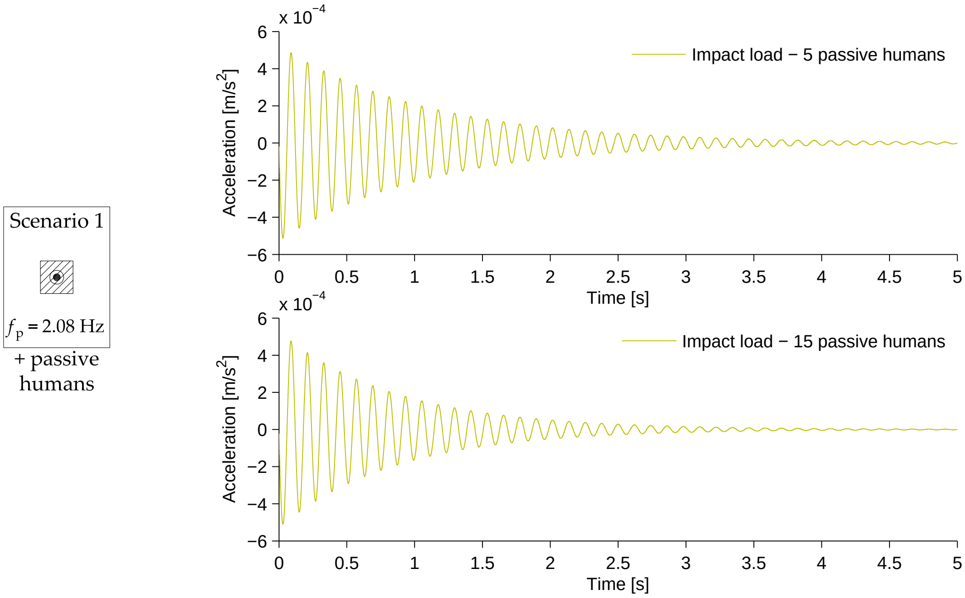

Figure 8.18: Examples of acceleration signal with free decay.

8.4 Response Analysis in ABAQUS

A response analysis in ABAQUS can give very useful results if it can be validated that the model has the same dynamic behaviour as the floor behaves in reality. Therefore, the scenarios described in Chapter 6 has been modelled in this section to compare the results from ABAQUS with the experiments, albeit the analyses with passive humans have been omitted from this analysis. All scenarios have been analyzed with loads according to both Ellis & Ji and Eurocode.

Besides the material properties determined in Chapter 5 after tuning, damping is also used as a material parameter. The mean damping ratio found in Section 4.4 to be $\zeta = 1.8\,\%$ is used in ABAQUS for all modes as structural damping for the materials. *Abaqus* uses direct integration of the equations of motion at specific time steps. The integration is performed in physical coordinates opposed to the modal coordinates used in the model decomposition method. The ABAQUS file for the response analyses is found on the Appendix CD as `ShellExcite.cae`.

8.4.1 Load and Time Series

The jumping load according to Ellis & Ji can be applied in ABAQUS as a periodic Fourier series. The Fourier series is defined by a load magnitude and direction $F(x, y, z)$, and a time varying amplitude function $Q(t)$. As the load is applied only in the vertical direction, the load can be expressed as stated in Eq. (8.18).

$$F(z,t) = F(z) \cdot Q(t) \tag{8.18}$$

In ABAQUS, the shell model is assembled by means of merging the meshes of both shell elements and beam elements. Therefore, the load must be applied to elements. This means that the elements which are closest to the regions defined in Chapter 6 are selected. The load is then applied in the load module as a pressure corresponding to the load distributed on the area of the chosen elements as stated in Eq. (8.19).

$$F(z) = \frac{\sum_{j=1}^{N} G_j}{A} \tag{8.19}$$

where

G_j Weight [N] of human number j.
A Area of the chosen elements in ABAQUS [m^2].

As an example, the elements chosen for Scenario 2 are shown in Figure 8.19.

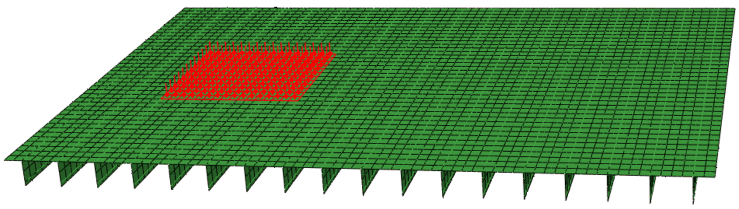

Figure 8.19: Chosen elements for Scenario 2.

When comparing the load series with the Ellis & Ji model in Eq. (7.6), G is the magnitude declared in the load module, and the rest of the expression is the amplitude time series. The amplitude time series is defined in ABAQUS as shown in Eq. (8.20).

$$Q(t) = a_0 + \sum_{i=1}^{I} a_i \cos(i\omega_p t) + b_i \sin(i\omega_p t) \qquad i = 1, 2, \ldots, I \tag{8.20}$$

It is seen from Eq. (7.6) that $a_0 = 1$, and since $\omega_\mathrm{p} = 2\pi / T_\mathrm{p}$, the coefficients a_i and b_i are equal to the coefficients in Eq. (7.8):

$$\begin{aligned} a_0 = 1 \quad , \qquad a_i &= \left(\frac{\cos\left((2ic_\mathrm{r}-1)\pi - 1\right)}{2ic_\mathrm{r}-1} - \frac{\cos\left((2ic_\mathrm{r}+1)\pi - 1\right)}{2ic_\mathrm{r}+1} \right) \\ b_i &= \left(\frac{\sin\left((2ic_\mathrm{r}-1)\pi\right)}{2ic_\mathrm{r}-1} - \frac{\sin\left((2ic_\mathrm{r}+1)\pi\right)}{2ic_\mathrm{r}+1} \right) \end{aligned} \tag{8.21}$$

In ABAQUS, a_0 is called the initial amplitude, and the coefficients a_i and b_i must be typed into a table with the calculated values. With a jumping frequency of 2.08 Hz, the coefficients and corresponding amplitudes α_i for 1 person ($c_r = 0.46$) and for 20 persons ($c_r = 0.52$) are compared in Table 8.3:

	1 PERSON ($c_r = 0.46$)			20 PERSONS ($c_r = 0.52$)		
i	a_i	b_i	α_i	a_i	b_i	α_i
1	0.2054	1.6191	1.6319	−0.1086	1.5310	1.5341
2	−0.7865	0.2019	0.8120	−0.5818	−0.0830	0.5862
3	−0.0410	−0.1034	0.1113	−0.0101	0.0467	0.0486
4	−0.1225	0.0673	0.1397	−0.1119	−0.0326	0.1161
5	−0.0343	−0.0472	0.0583	−0.0091	0.0247	0.0268
6	−0.0361	0.0339	0.0495	−0.0433	−0.0196	0.0473

Table 8.3: Fourier coefficients for 1 person and 20 persons.

The jumping load according to Eurocode has been calculated as a time series according to Chapter 7 in MATLAB with `ftEurocodeAbaqus.m` and imported as tabular data in ABAQUS as the amplitude function, $Q(t)$.

A comparison of how well a certain time step describes the jumping load has been used to choose the time step. To simulate a sufficiently accurate load, the smoothness of a plot of the load amplitude calculation is considered. A comparison of plots of the load amplitude with time steps of 0.1 s and 0.01 s can be seen in Figure 8.20, where it is seen that a time step of 0.1 s does not yield an accurate load time series.

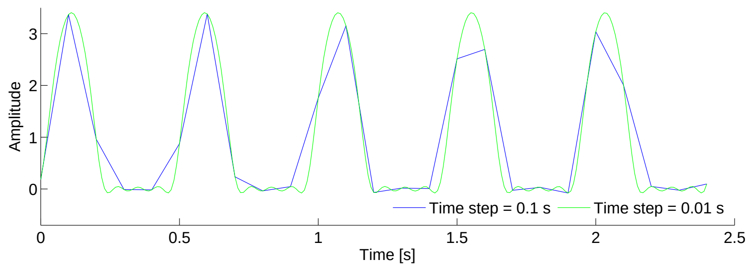

Figure 8.20: Comparison of load plots for time steps of 0.1 s and 0.01 s.

From a comparison of different time steps, it has been chosen that the response analysis will be performed with a time step of $\Delta t = 0.02$ s, which equals a sampling frequency of 50 Hz.

To choose the total time for analysis, the response seen in the analytical solution in Figure 8.9 has been considered. When the initial conditions have damped out, the motion becomes harmonic with the same frequency as the load. This means that the results can be considered representative when the initial condition are damped out, and the response motion reaches a steady state. From the analytical solution, a total time of $t_{tot} = 5$ s has been chosen.

To be able to compare the results with the experiments, data is collected from the bottom side of each rib at $x = L_x/2$. This provides the acceleration time history on the mid-span of each rib, i.e. 18 acceleration time histories.

8.4.2 Results from ABAQUS

Before the maximum and root-mean-square accelerations are determined, the acceleration time history is considered. It is consistent that large accelerations occur immediately after the load is applied. These large accelerations are most probably due to too large time steps, as this actually is the build-up period. As these accelerations are not expected to be representative for the scenario, these initial data are omitted. The principle is shown for the acceleration at rib 9 in Scenario 1 in Figure 8.21.

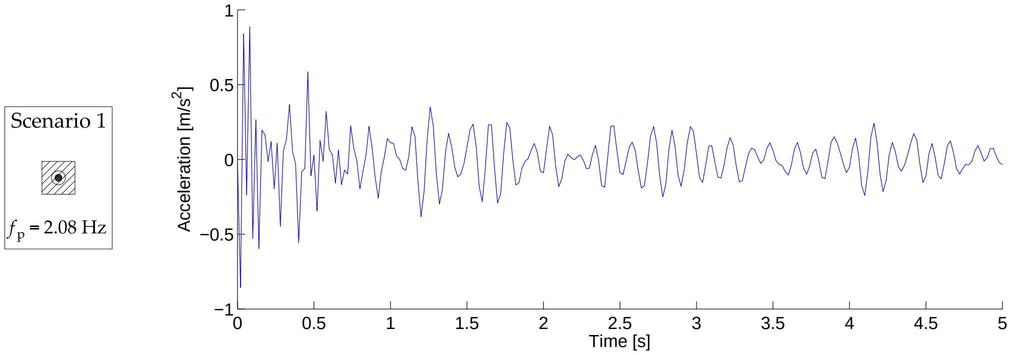

Figure 8.21: Acceleration at rib 9 in Scenario 1.

The accelerations are seen to be consistent after approximately 2 s with a more smooth signal, and therefore it is chosen that the maximum and root-mean-square accelerations will be found for the time period $2\,\mathrm{s} \le t \le 5\,\mathrm{s}$, which corresponds to considering the stationary response only.

Control of Serviceability Limit State

The result data from ABAQUS has been treated with `HistoryData.m` to calculate the accelerations at the 18 ribs. The largest $a_{\max}$ and a_{rms} accelerations for all of the 18 ribs are shown in Figure 8.22, and therefore no specific position for the output is stated. Generally, the largest value of $a_{\max}$ and a_{rms} is found underneath each load area using the Eurocode load model, but this is not necessarily true for the Ellis & Ji model. An equivalent contact ratio $c_{r,\mathrm{eq}}$ are used in the Ellis & Ji load model.

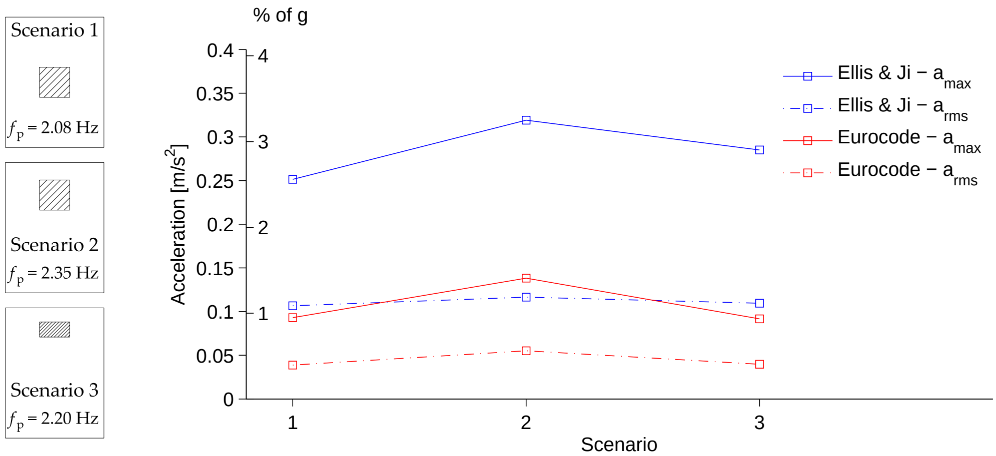

Figure 8.22: Acceleration results for Scenarios 1–3.

The maximum acceleration and maximum root-mean-square acceleration, which is found in Scenario 2 with the Ellis & Ji load model, are $a_{\max} = 0.32\,\mathrm{m/s^2}$ and $a_{\mathrm{rms}} = 0.12\,\mathrm{m/s^2}$, corresponding to 3.3 % and 1.2 % of g, respectively.

As the above-mentioned results are maximum values for all 18 measuring points in the model, it is not certain that these results can be compared directly with the analytical solution and experiments. Therefore, the maximum accelerations and root-mean-square accelerations for Scenario 1, measured at the measure point at rib 4, have been found. These are seen Figure 8.23.

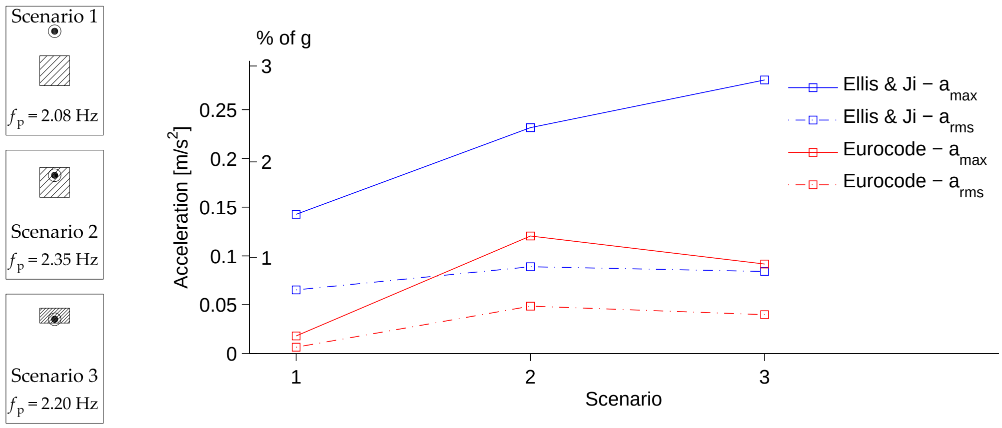

Figure 8.23: Acceleration results measured at rib 4.

The results shown in Figure 8.23 are the accelerations which are to be compared with the results from the analytical solutions and experiments. The acceleration results from rib 4 are therefore listed in Table 8.4.

a [m/s^2]		Ellis & Ji	Eurocode
Scenario 1	a_{max}	0.14	0.02
	a_{rms}	0.07	0.01
Scenario 2	a_{max}	0.23	0.12
	a_{rms}	0.09	0.05
Scenario 3	a_{max}	0.28	0.09
	a_{rms}	0.08	0.04

Table 8.4: Acceleration results at rib 4.

Parameter Study of Crowd Reduction Effect

Also the cases where different number of persons are jumping in the jumping area from Scenario 1 have been analyzed. The maximum and root-mean-square accelerations for $N = 5$, 10, 15, and 20 persons in load area 1 are seen in Figure 8.24. The results using the Ellis & Ji load model show

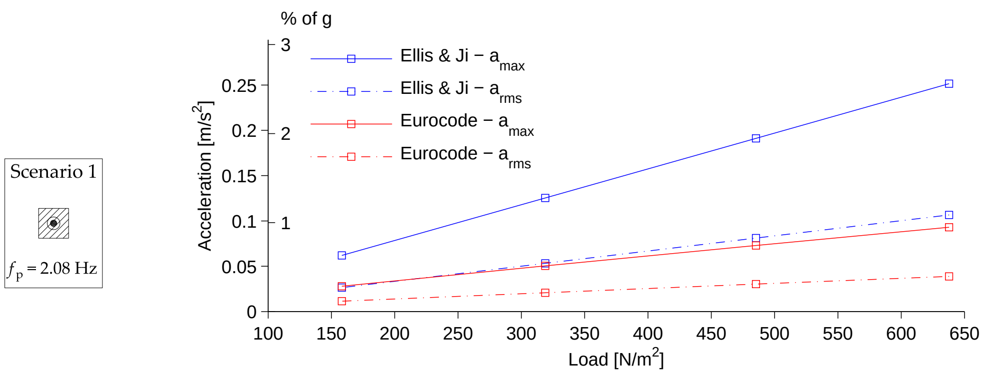

Figure 8.24: Acceleration results for different number of jumping persons.

that the accelerations increase proportionally with the load inside the same area. If calculations had been included for e.g. one and two persons, the slope of the graph in Figure 8.24 is expected to be steeper for fewer persons, but as the equivalent contact ratio is almost equal for N = 5,10,15, and 20, the results show an almost linear increase. As for Scenario 1–3, the maximum accelerations calculated with the load model from Eurocode are approximately of the same magnitude as the maximum root-mean-square acceleration calculated with the Ellis & Ji load model.

8.5 Response from Experiments

In connection with the assessment of the floor response when subjected to human jumping loads, a third series of experiments was performed at Nordkraft. The tests were laid out to fit the scenarios described in Table 6.1 and in total 36 experiments were planned:

- Control of serviceability limit state: 3×5 tests, Scenario 1, 2, and 3 with 20 jumpers.
- Parameter study on crowd reduction effect: 4×3 tests with 5, 10, 15, and 20 jumpers.
- Parameter study on human damping effect: 3×3 tests with 5, 10, 15, passive humans and 5 jumpers.

8.5.1 Preperation of Measurements

The set-up used for the experiments was the same as used for the second tests series, in the sense that the measurements were done from underneath the floor and with the same equipment. The accelerometer position were varied as indicated in Figure 6.1 where "Pos. A" is sometimes mentioned as "4th rib" and "Pos. B" can be referred to as "Midpoint" or "9th rib".

The actual data treatment was taken a bit further as the measured signal was run through a Butterworth lowpass filter of order 8 with a cut-off frequency of 20 Hz. The Butterworth filter passes through lower signal frequencies, while it at a specific frequency starts to scale and eventually fully remove remaining frequency contributions. The effect of the filter is shown in Figure 8.25, where a signal with integer frequency components of equal magnitude is generated and its frequency components shown. In the underlying figure, the signal has been filtered and its frequency components are shown.

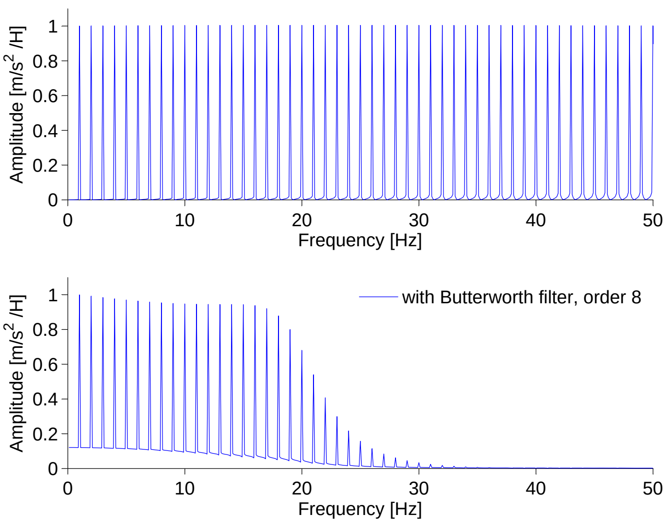

Figure 8.25: FFT plots showing frequency passing, scaling, and cut-off.

From Figure 8.25 it can be seen that frequency components up until approximately 17 Hz passes through the filter nearly untouched. On same note frequency components over 30 Hz are fully removed. This was found suitable for the treatment of the data as no scaling of the first three vibration mode components was wanted and the high frequency components are eliminated. Figure 8.26 shows the effect of the filter order.

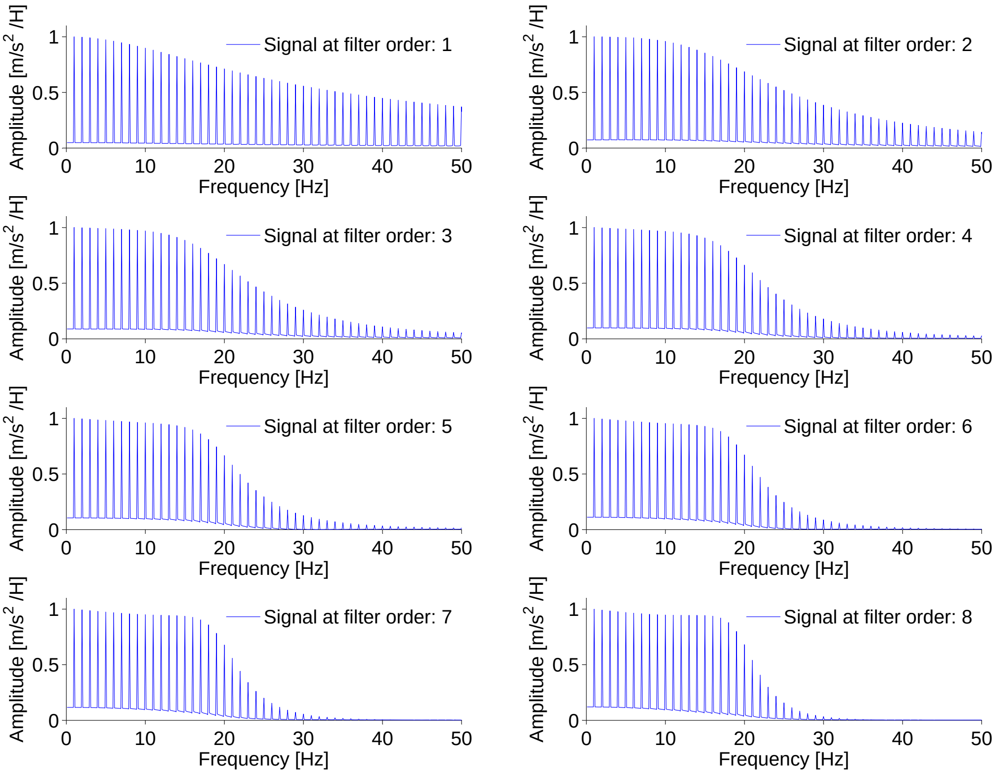

Figure 8.26: Effect of filter order.

It is evident that the removal of higher frequency components can reduce the magnitude of the measured maximum accelerations, but as it was chosen to focus on the first three modes, the filtering was initialized for better comparison possibilities with the other analysis methods. This means that all presented FFT plots are generated from filtered signals, whereas in many acceleration plots the unfiltered values are also included to illustrate the effect of the filter and the acceleration contributions from high frequency components. An example of a measured signal is shown in Figure 8.27 where two zoom-ins are also shown to illustrate the effect of the Butterworth filter.

When analysing the measurement signals, the used time windows are dependent on the individual signal. For every signal a matching time window is specified, so that the output values are calculated from a steady state response only. In the MATLAB-files which processes the data, it can be chosen whether to use the specified time windows or full signals.

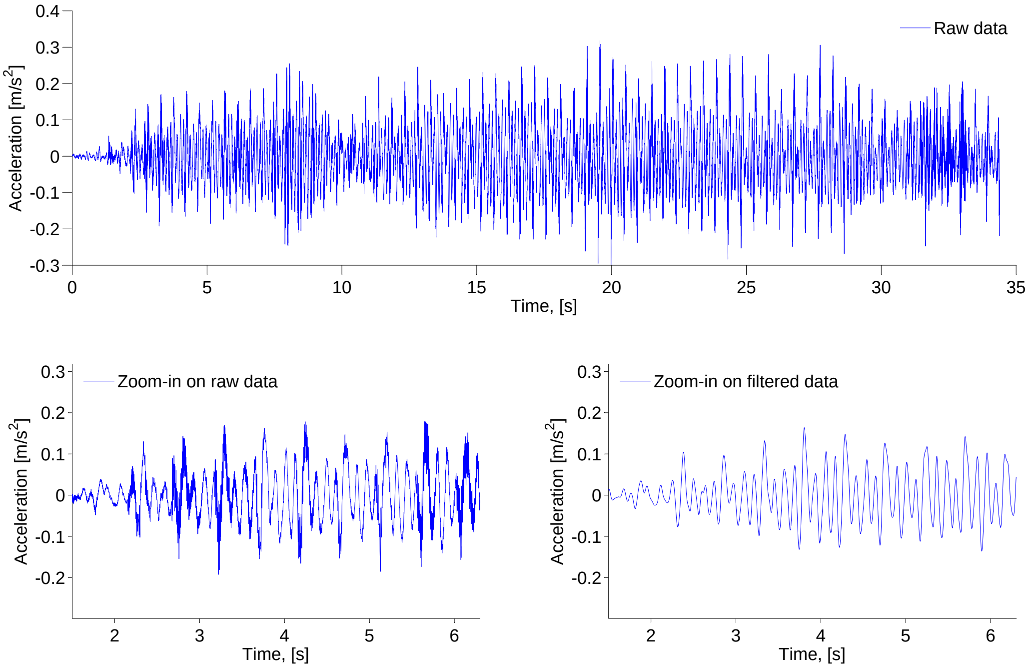

Figure 8.27: Full measurement signal, zoom-in on both raw and filtered signal.

8.5.2 Results from Experiments

In the following, the results from the experimental response analysis is presented. Firstly the control of serviceability limit state experiment results are presented where after the results from the two parameter studies are shown.

Control of Serviceability Limit State

The main purpose of the third round of experiments was to investigate if the deck construction in fact was able to conflict with the limits of the serviceability in the mentioned scenarios. This meant that the measurements had to be taken from a position where all modes were detectable. For this reason the accelerometer was attached to the midpoint of the fourth rib from the northern side, marked “Pos. A” in Figure 6.1. From the illustration of the assumed vibration mode shapes of the first three modes, it is seen, that this position provides measurements close to the maximum of the second and third mode, whereas accelerations caused by the first mode only enters with a value of, $\Phi_{L_y}(4.2\text{m}) = 0.57\%$ compared to its maximum value. If the vibrations measured in connection with Scenario 1 are dominated by vibrations at the first mode, a scaling with this value could perhaps correspond to measurements taken at “Pos. B”. However, this scaling is not likely to be possible when looking at a full signal containing vibrations caused by several vibration modes.

The three test scenarios were planned so each would focus on a worst case exciting frequency and position of the load. The tests were conducted with 20 jumpers and five repetitions for each scenario. The data is treated in `Cases.m`. In Figure 8.28 the results are presented. For each scenario six kinds of data points are marked. The a_{max} and $a_{\text{But,max}}$ values represent the absolute maximum acceleration value measured throughout both the measured and the filtered signal, respectively. $\overline{X}(a_{\text{max}})$ and $\overline{X}(a_{\text{But,max}})$ show the average peak acceleration values while the a_{rms} and $a_{\text{But,rms}}$ show the calculated root-mean-square values.

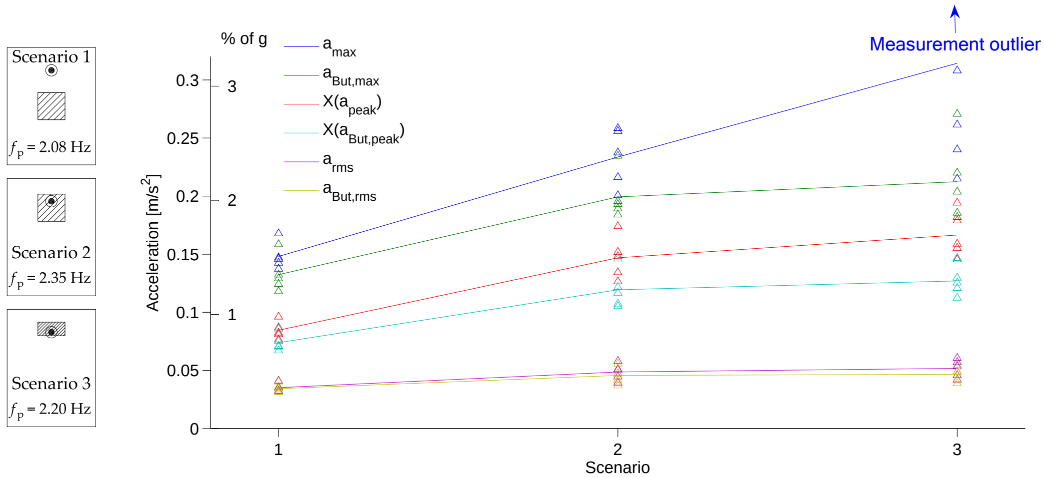

Figure 8.28: Measured accelerations from Scenarios 1, 2, and 3.

To study the contents of the signals in more detail, FFT analysis is also applied to the measurements. The resulting plots can be seen in Figures 8.29 to Figure 8.31.

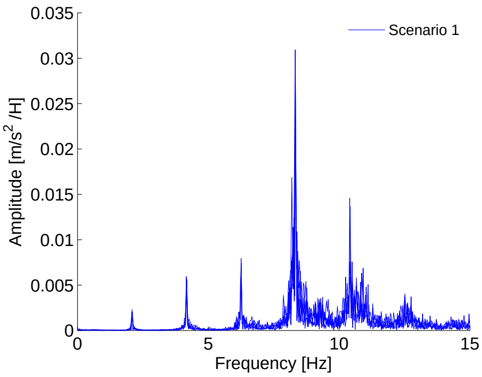

Figure 8.29: FFT plot of Scenario 1 tests.

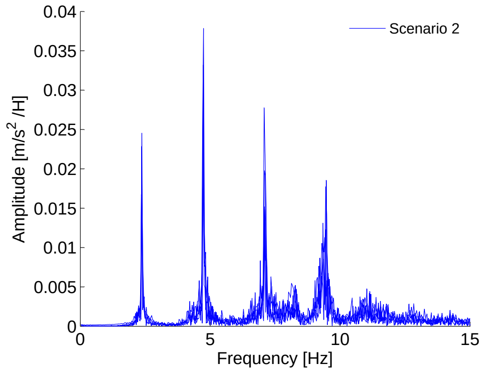

Figure 8.30: FFT plot of Scenario 2 tests.

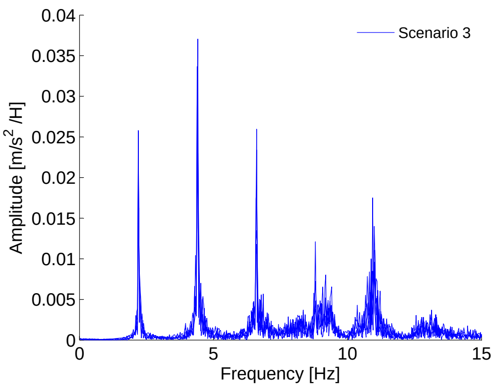

Figure 8.31: FFT plot of Scenario 3 tests.

From the plots, it can be seen that the largest contributor to the accelerations measured in Scenario 1 is the vibrations at the first natural frequency, 8.3 Hz. Furthermore it can be noted, that the fifth load component is able to hit in the outer rim of the third mode. For Scenario 2 and 3, the

FFT analysis reveals that the accelerations originate more from the first three load components, rather than being dominated by resonance contributions, as it was sought by applying jumping frequencies which at integer multipliers would match the modes frequencies. It is suspected that since the measurements were taken almost directly under the load area for Scenario 2 and 3, the data reflect some local deformation effects due to the orthotropic nature of the deck. The local deformations might interfere with the assumption of how the deck reacts to the human jumping loads in the analytical methods, where it is only able to deform corresponding to the chosen vibration modes. For this reason, the FFT plot of the Scenario 1 tests is compared with a corresponding FFT plot of a test series with the accelerometer position placed under the jumpers, “Pos. B”, see Figure 6.1.

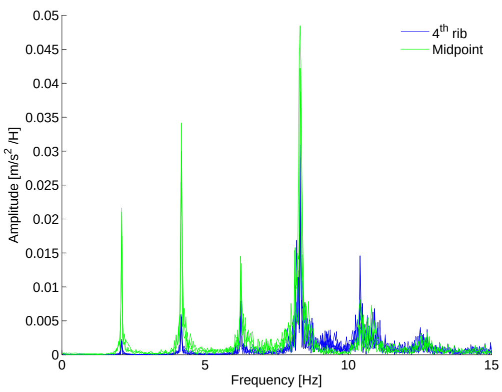

Figure 8.32: Scenario 1, influence of measurement position.

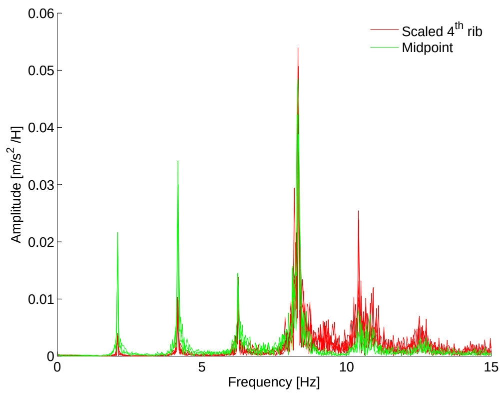

Figure 8.33: Scenario 1, scaled influence of measurement position.

Figure 8.32 clearly shows that when taking measurements from directly beneath the jumpers, the amplitude of the lower harmonics are much higher than when measured at the 4$^{\text{th}}$ rib. To compare the data further, the signals measured at the 4$^{\text{th}}$ rib are scaled by the use of the assumed half sine mode shape to be of same magnitude as if measured at the midpoint. The resulting FFT comparison plot can be seen in Figure 8.33. Here it is seen that the magnitude of the accelerations generated at 8.3 Hz are now of similar magnitude, whereas the contributions from the lower harmonics are still much lower than if taken from “Pos. B”.

For the sake of completeness the values at 8.3 Hz are listed in Table 8.5, where it can be seen that the vibrations at 8.3 Hz can be scaled using the assumed mode shape to quite good agreement.

ACCELERATION [m/s^2/H]		4$^{\text{th}}$ rib	4$^{\text{th}}$ rib scaled	Midpoint
	1	0.0279	0.0487	0.0420
	2	0.0291	0.0507	0.0388
Test repetitions	3	0.0234	0.0408	0.0485
	4	0.0232	0.0405	
	5	0.0309	0.0539	
Mean value		**0.0269**	**0.0469**	**0.0432**

Table 8.5: Comparison of 8.3 Hz FFT acceleration values.

Parameter Study of Crowd Reduction Effect

The first of the parameter studies to be performed was on the effect of adding additional jumpers. The jumping area was the same as for the Scenario 1 tests and the measurements were taken from "Pos. B". Four series, with 5, 10, 15, and 20 jumpers, were performed with three tests in each. The tests are done in order to assess the crowd reduction factor as stated in the Eurocode model and the one derived by the authors. The measurements are treated with `Npersons.m` and are visualized in Figure 8.34. From the figure it can be seen that the accelerations increase as more jumpers are added, an the magnitude of the slope of increase in accelerations, can be commented through a comparison with the other analysis methods. It can be noted, that it seems that the three tests with 10 jumpers seem to have a good coordination compared to the succeeding 15 jumpers, who do not attain a significant increase in accelerations, if any.

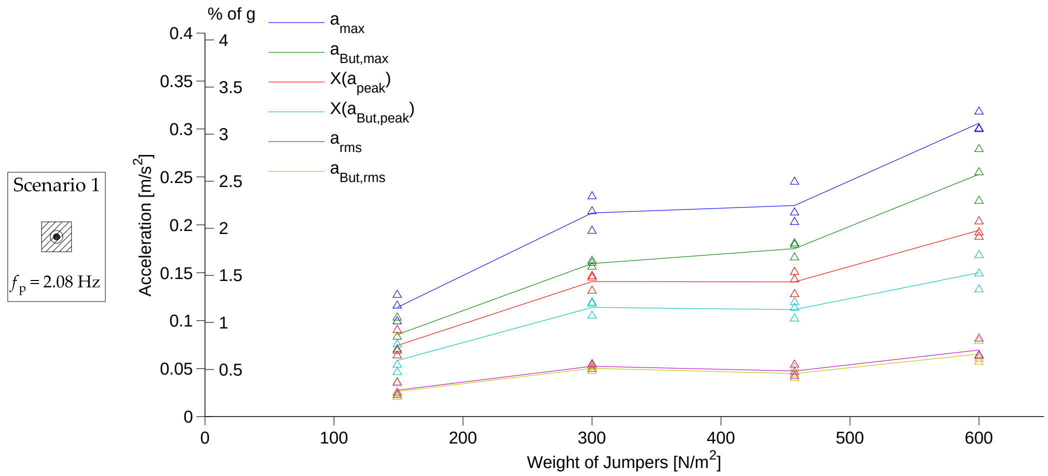

Figure 8.34: Accelerations when adding jumpers.

Parameter Study of Human Damping Effect

The second parameter study was on the effect of passive humans. The data is treated with `Passive.m` and the results are shown in Figure 8.35, where a slight reduction in accelerations is seen from the root-mean-square values as more passive humans are added. For further comments, these results will be compared in Chapter 9 with the assessments done numerically.

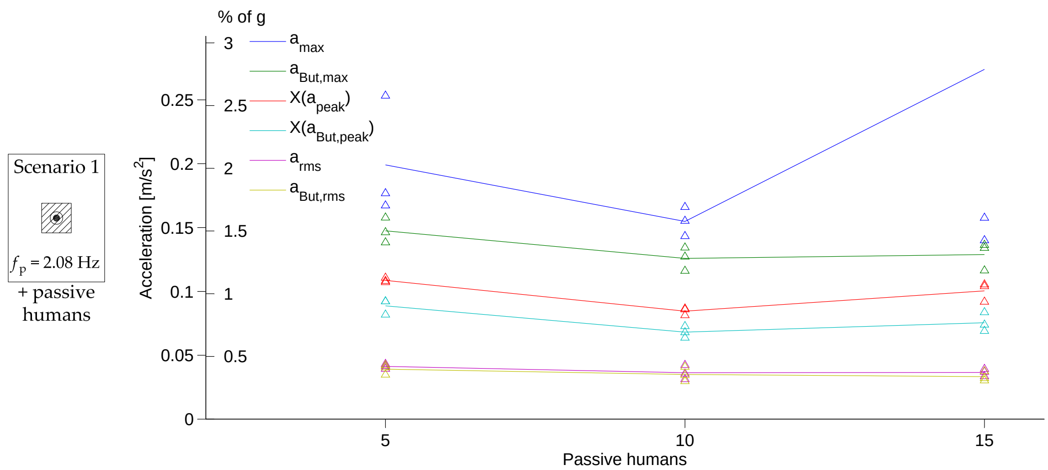

Figure 8.35: Accelerations when adding passive humans.

It can be concluded that there is a significant difference between the filtered signals and the raw signal when it comes to maximum values. As it is not obvious to determine what causes the higher frequency contributions, it is for the further comparisons and conclusions chosen to use the filtered signal values to ensure that only the modelled vibration modes contribute. However, it is seen that the root-mean-square values are not very sensitive to the filtering, indicating that the average amplitude of acceleration is caused by the lower vibration modes. Also it is noted that there is quite a significant difference on the acceleration magnitude throughout the signals, making the average peak values much lower than the absolute peaks. This indicates that the coordination in between the jumpers varies a lot throughout the jumping session.

As an elaborating experiment, an additional test were done in a slightly different manner compared to the previous tests. The test scenario consisted of five jumpers who jumped continuously throughout the duration of the test. Present on the deck were also five passive humans who, one by one and in an even interval left the deck. The filtered, measured acceleration signal can be seen in Figure 8.36.

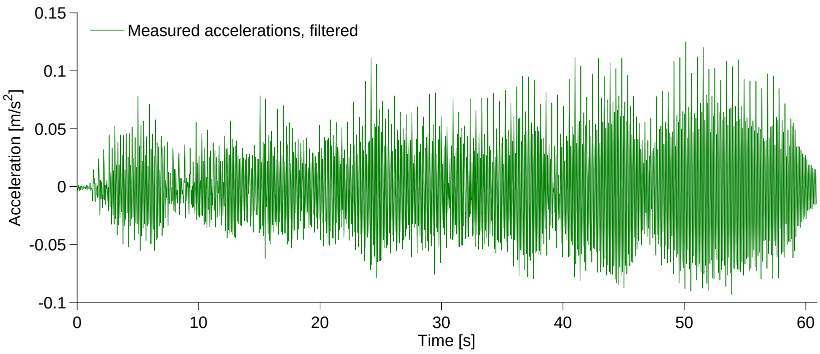

Figure 8.36: Measured acceleration signal from extra experiment.

From Figure 8.36 several things can be noted. First off, the magnitude of the acceleration amplitude seems to generally increase throughout the test duration. This is expected as damping is removed whenever a passive human leaves the load area. Secondly, the peak accelerations are seen to vary a lot over the signal, and individual maximum peaks at e.g. 4 passive humans, around 25 seconds in, reach similar magnitudes as peaks after all passive humans have left the deck at approximately 50 seconds in. This underlines the effect of synchronization of jumpers. The precise timing on when each passive human left the deck is not fully known, but in Figure 8.37 the signal is cut at 9 seconds where the jumpers are assumed to have found the rhythm and the deck has had time to build up response. From here, one passive human leaves the deck every 9 seconds whereafter the jumpers continue to jump for another 9 seconds without any passive humans present on the deck.

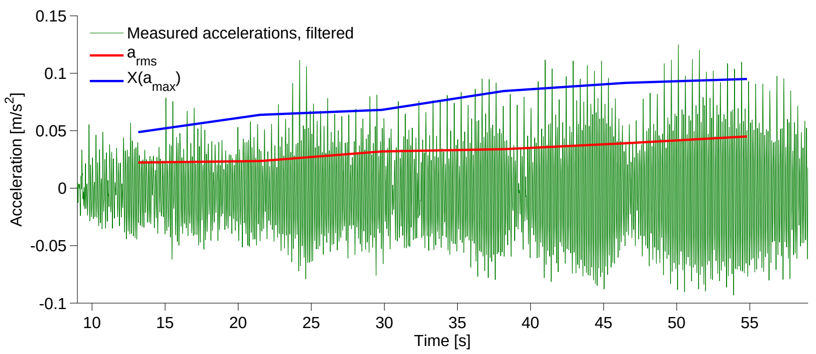

Figure 8.37: Measured acceleration signal from extra experiment.

In every interval a value of the average a_{rms} is calculated together with the average of the acceleration peaks $\overline{X}(a_{\text{peak}})$ and a line is drawn though the points to illustrate the increase in acceleration magnitude during the experiment. This is illustrated in Figure 8.37. The processing of the extra test is carried out in `Extra.m`.

Chapter 9

Comparison of Response Analysis Methods

In the following chapter, results from the presented methods are compared and assessed. The comparison of the results is based on the three different aspects defined in Table 6.1.

✦ ✦ ✦

As not all methods consider all three aspects, the methods defined in Table 9.1 are compared for each of the three aspects, respectively.

ASPECT	METHOD
Control of serviceability limit state	Simplified Eurocode Procedure Analytical Solution of Differential Equation ABAQUS Experiments
Parameter study of crowd reduction effect	Analytical Solution of Differential Equation ABAQUS Experiments
Parameter study of human damping effect	Newmark Time Integration Experiments

Table 9.1: Plan of results comparison.

It should be kept in mind that the analytical solution of the differential equation and Newmark time integration gives completely similar results for the two first aspects, and therefore, Newmark time integration is not mentioned here. Plots for the following three sections are made by the MATLAB-script `Comparison_response_methods.m`.

9.1 Control of Serviceability Limit State

Comparisons are done for output values and measurements at the mid-point of the deck, $(x, y) = (L_x/2, L_y/2)$, and at the 4th rib, where the accelerometer was attached during some experiments, $(x, y) = (L_x/2, 17.4\text{ m})$. For all experimental results, the previously described Butterworth filter has been applied. The filtered results are used instead of the unfiltered values, as high frequency contributions are not present in the calculation models, only in the experimental results.

Comparisons of a_{max} and a_{rms} values taken at the mid-point are shown in Figure 9.1 and Figure 9.2, respectively. Results for the simple Eurocode procedure is shown only in connection with Scenario 1 as the two remaining scenarios are not considered in this method. Likewise, only direct measurements from the experiments are available at the mid-point is found for Scenario 1, where the results of the five test series are plotted.

Results obtained from the Eurocode load model are significantly lower than the experimental results for Scenario 1. This indicates that resonance has not been achieved. Furthermore, good agreement can be seen between the analytical solution and the ABAQUS solution when using the Eurocode load model. This agreement is remarkable when comparing the analytical solution and ABAQUS solution for the Ellis & Ji load model, where considerable deviation is seen. As previously touched upon, the Eurocode model gives merely a static response without dynamic effects for this deck construction, and this might explain the good agreement between the analytical solution and ABAQUS solution, because the two models predict static response in the same way. On the contrary, the dynamic effects are calculated very differently in the analytical solution and ABAQUS solution.

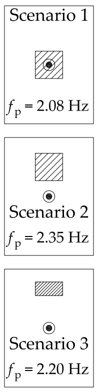

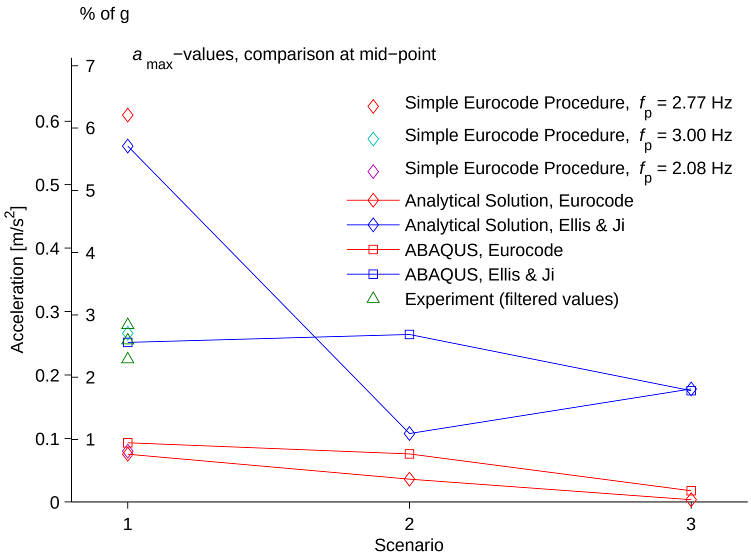

Figure 9.1: Comparison of a_{max} values at mid-point, $(x, y) = (L_x/2, L_y/2)$.

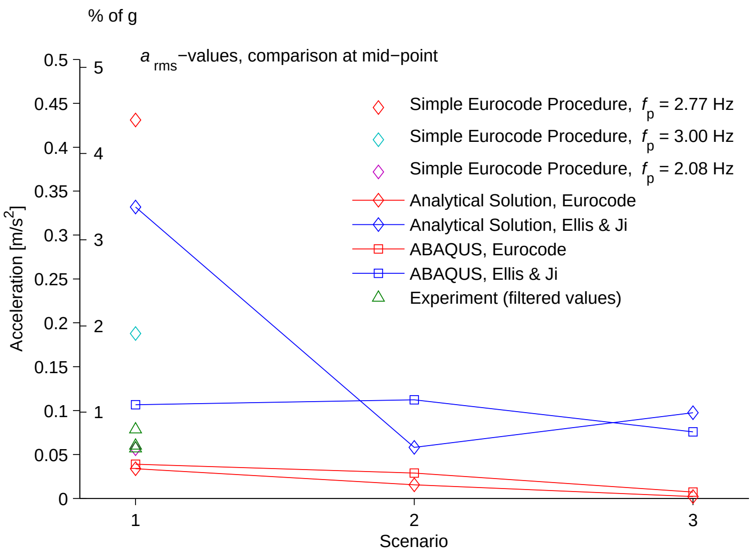

Figure 9.2: Comparison of a_{rms} values at mid-point, $(x, y) = (L_x/2, L_y/2)$.

It is noticeable that for Scenario 2, the analytical solution yields quite low accelerations. This is due to the shape function of the second mode used in the modal decomposition, which is zero at the mid-point. Therefore, the second mode, which is excited in Scenario 2, cannot be measured at the mid-point.

The results of the simple Eurocode procedure are relatively scattered. The accelerations found for $f_p = 2.08\,\mathrm{Hz}$, which is the jumping frequency used in the other methods in Scenario 1, are in good agreement with the analytical solution and ABAQUS solution using the Eurocode model, and hence underestimates the accelerations compared to the experimental results. The accelerations for the jumping frequencies $f_p = 2.77\,\text{Hz}$ and $f_p = 3.00\,\text{Hz}$ are shown for the sake of completeness, as they are not directly comparable with the remaining results.

Comparison of a_{max} and a_{rms} values taken for the 4th rib is shown in Figure 9.3 and Figure 9.4, respectively. Opposite at the mid-point, experimental results is present for all three scenarios, with five results for each scenario.

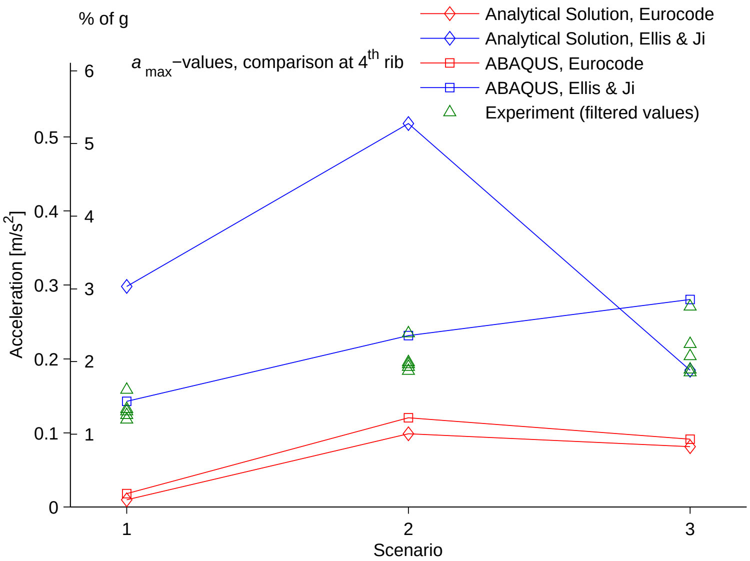

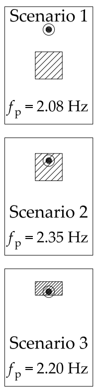

Figure 9.3: Comparison of a_{max} values at 4th rib, $(x, y) = (L_x/2, 17.4\text{ m})$.

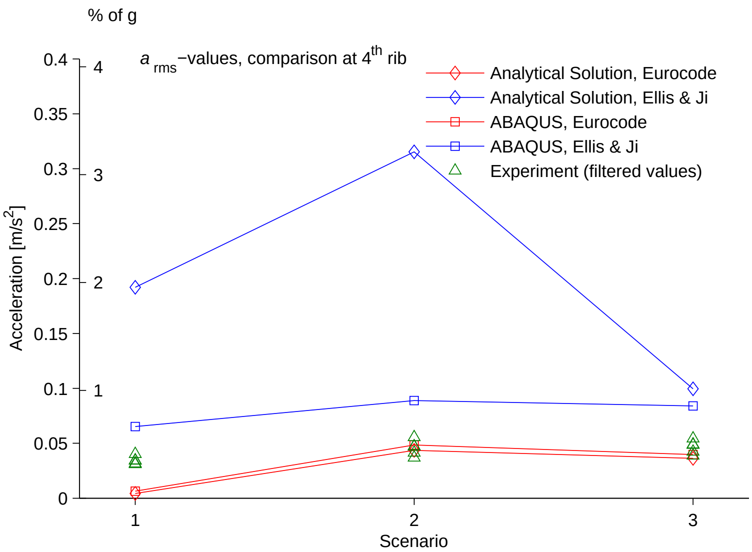

Figure 9.4: Comparison of a_{rms} values at 4th rib, $(x, y) = (L_x/2, 17.4\text{ m})$.

Again, results using the Eurocode load model are similar for the analytical solution and ABAQUS solution, and the previously mentioned argument is assumed to apply as well. The ABAQUS solution with the Ellis & Ji load model seems to be in good agreement with the experimental results, especially for the a_{max} values.

By comparison of the two graphs it seems likely that the Eurocode load model gives the closest fit to the experimental results, when the a_{rms} values are wanted, whereas the Ellis & Ji load model is preferable when estimating a_{max} values.

9.2 Parameter Study of Crowd Reduction Effect

Comparison of a_{max} and a_{rms} values for analyses regarding the crowd reduction effect are shown in Figure 9.5 and Figure 9.6. For the experimental results, both absolute maximum values are shown as well as mean values of the peak values during a time series. The absolute maximum values are in relatively good agreement with the ABAQUS solution using the Ellis & Ji load model. Gradually, as more humans participate in the jumping, a more gentle slope of the graphs would

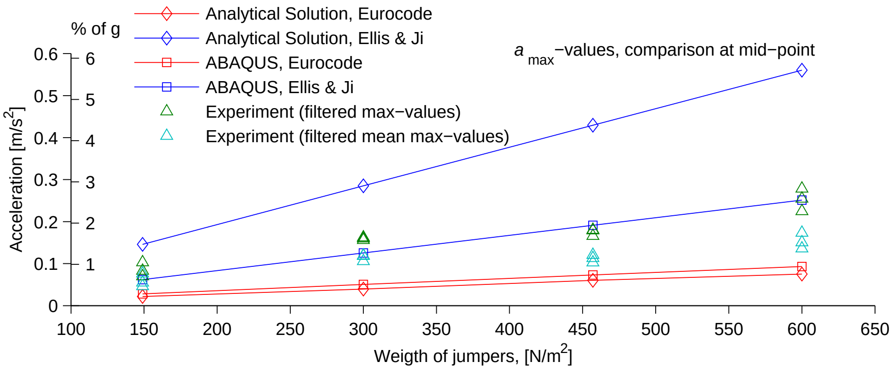

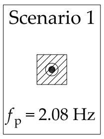

Figure 9.5: Comparison of a_{max} values at mid-point, $(x, y) = (L_x/2, L_y/2)$.

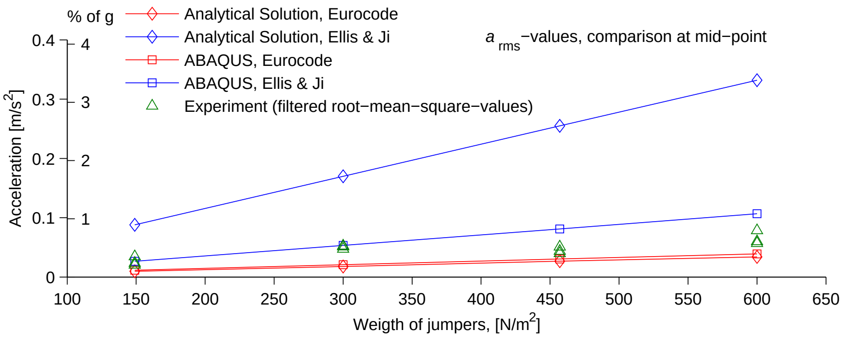

Figure 9.6: Comparison of a_{rms} values at mid-point, $(x, y) = (L_x/2, L_y/2)$.

be expected due to the crowd reduction effect. However, this trend is not pronounced in any case, only for the solutions using the Eurocode load model and the experimental results, the slope is slightly falling. Results from the Ellis & Ji load model seem to form a straight line and hence, the used equivalent contact ratio $c_{\text{r,eq}}$ takes the crowd reduction effect into account in a quite conservative manner. Also, the conclusion from the crowd reduction effect study might be that a greater number of humans should be used in the investigation if used for tuning. The experimental results, which contains measurements with 5 to 20 jumping humans, are not clear enough to suggest a general expression for the crowd reduction factor.

9.3 Parameter Study of Human Damping Effect

A comparison of a_{max} and a_{rms} values for results regarding the human damping effect is shown in Figure 9.7 and Figure 9.8. The results are obtained with 5 jumping humans and with 0, 5, 10, and 15 passive humans.

The damping effect of humans is evident for results using the Ellis & Ji load model due to the negative slope, whereas no damping effect can be observed for results from the Eurocode model. As previously mentioned, resonance is not achieved using the Eurocode model, and the

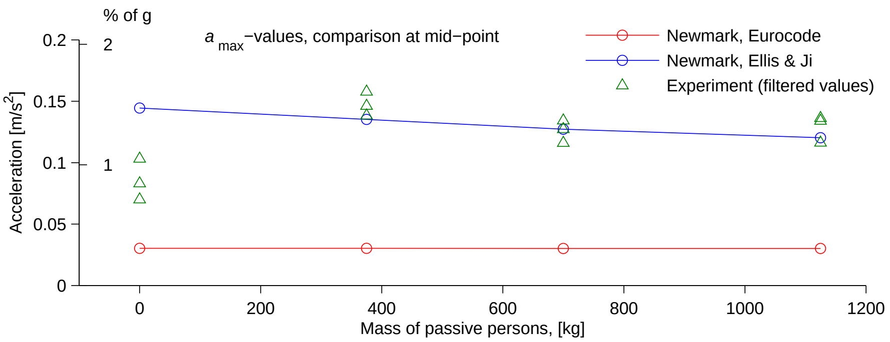

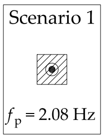

Figure 9.7: Comparison of a_{max} values at mid-point, $(x, y) = (L_x/2, L_y/2)$.

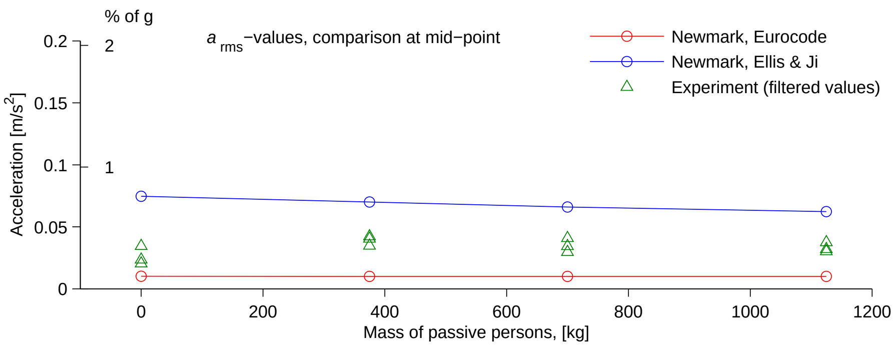

Figure 9.8: Comparison of a_{rms} values at mid-point, $(x, y) = (L_x/2, L_y/2)$.

acceleration is merely a result of a static reaction. Therefore, added damping will not have any influence.

The characteristic "jump" in the experimental results from 0 to 5 passive humans is due to different jumping humans in two different test series. The results for 0 passive jumping humans are the same as for the parameter study of the crowd reduction effect. As such, the results are not directly comparable, but the relatively large difference illustrates that very different results might be obtained with different groups of jumping humans. As the weight of the two jumping crowds were approximately the same, it is obvious that the jumping crowd, where passive humans are present, achieved a significantly better synchronization.

Besides the results for 0 passive humans, good agreement between the Newmark solution and experimental results is seen. This is opposite other results obtained from the analytical solution, and hence Newmark solution, where these seem to overestimate the accelerations. This might be explained from the number of jumping humans. Also in the study of the crowd reduction effect, the analytical solution was in closer agreement with the experimental results for a few jumping humans than for more jumping humans. This might indicate an amplitude dependency, which is not taken into account by the analytical solution and Newmark solution.

9.4 Limitations of Modal Decomposition Method

From the comparison of maximum and root-mean-square accelerations in the preceding sections, it is obvious that results from the analytical solution (and Newmark solution) deviates significantly from the ABAQUS solution when using the Ellis & Ji model. This observation is treated in the following two sections.

9.4.1 Changed Jumping Frequency

A comment is made on the modal decomposition method, which is used in connection with the analytical solution of the differential equation and Newmark time integration. In both methods, it is assumed that a load component of the forcing frequency f_p hits the resonance frequency exactly, i.e. $i f_\mathrm{p} = f_{1n}$. For the first and second mode, $n = 1$ and $n = 2$, the jumping frequency f_p is adjusted so the fourth load component hits resonance, $i = 4$, while for the third mode, $n = 3$, the jumping frequency is adjusted, so the fifth load component hits resonance, $i = 5$. This is a conservative assumption, which is particular pronounced when the damping is low.

The calculated response is very sensitive with respect to the used jumping frequency, which is illustrated in Figure 9.9. Here, the dynamic amplification factor D is plotted for the three first modes, which have been considered in the modal decomposition technique. The dynamic am-

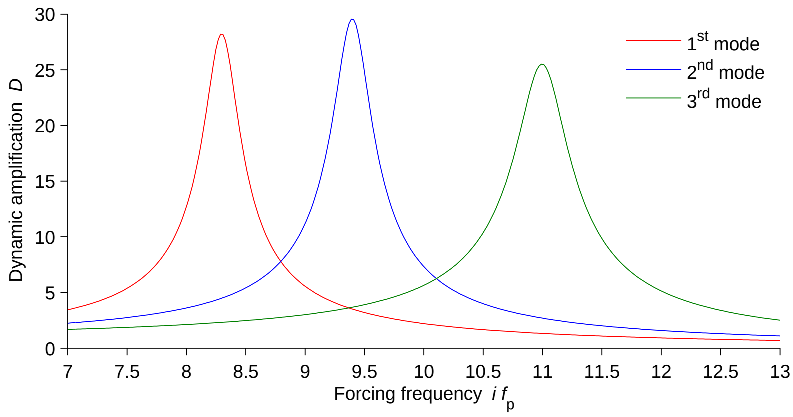

Figure 9.9: Dynamic amplification.

plification factor D is given by Eq. (9.1) and represents the amplification of response due to dynamical effects compared to the pure static response [17]. The dynamic amplification factor D is equivalent to the structural response factor H_i defined in Eq. (8.3) for the simplified Eurocode procedure.

$$D\left(\zeta_n, i f_\mathrm{p}, f_{1n}\right) = \frac{1}{\sqrt{\left(1-\left(\frac{2\pi i f_\mathrm{p}}{2\pi f_{1n}}\right)^2\right)^2 + 4\zeta_n^2\left(\frac{2\pi i f_\mathrm{p}}{2\pi f_{1n}}\right)^2}} \tag{9.1}$$

As seen from Figure 9.9, just small deviations from the resonance frequencies give a significantly smaller dynamic amplification factor and thereby acceleration. To illustrate the sensitivity in the analytical solution and Newmark time integration with respect to the forcing frequency, this parameter is slightly changed away from resonance.

According to Appendix D, it is assumed that the standard deviation of a human's jumping frequency within a time series can be set to $S_{f_\mathrm{p}} = 0.15$. Using this value, the jumping frequency f_p is increased by $\frac{1}{2} S_{f_\mathrm{p}}$ for each scenario. A reduction could as well be used, but due to the symmetry of the dynamic amplification curves in Figure 9.9, the results are approximately the same. The increased jumping frequencies are shown in Table 9.2 in comparison with the original jumping frequencies. Obviously, even a small change in the jumping frequency f_p will accumulate on the higher load components. The change in acceleration level due to the change in forcing frequency is illustrated in Figure 9.10. This graph corresponds to Figure 9.4 from the comparison of results, where only the analytical solution and ABAQUS solution using the Ellis & Ji load model is shown.

Obviously, a slight change of forcing frequency away from resonance gives a significant drop in response for Scenario 1 and Scenario 2, but a small increase for Scenario 3. This increase is

MODE	ORIGINAL/INCREASED JUMPING FREQUENCY	LOAD COMPONENT	ORIGINAL/INCREASED RESONANCE FREQUENCY
n	f_p	i	$i\,f_p$
1	2.08 Hz / 2.16 Hz	4	8.30 Hz / 8.62 Hz
2	2.35 Hz / 2.43 Hz	4	9.40 Hz / 9.70 Hz
3	2.20 Hz / 2.28 Hz	5	11.0 Hz / 11.38 Hz

Table 9.2: Original and increased jumping frequencies.

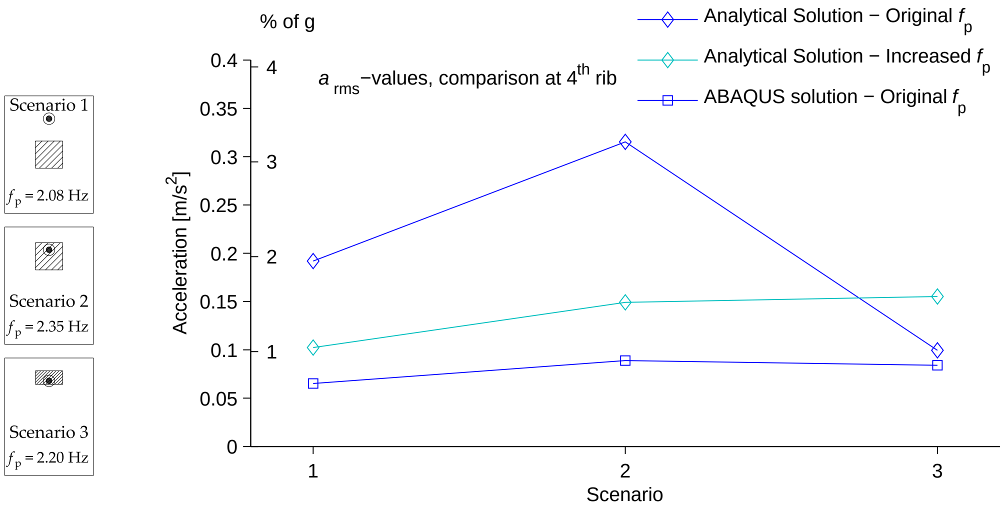

Figure 9.10: Comparison of acceleration from original and increased jumping frequency.

probably due to the fact that the fourth load component of the increased jumping frequency at $i\,f_p = 4 \cdot 2.28$ Hz $= 9.12$ Hz is closer to resonance for the second mode at 9.4 Hz than the fourth load component of the original jumping frequency.

In relation to this, it might be of importance that the chosen jumping frequencies f_p of the three scenarios in Table 6.1 have been adjusted due to the target natural frequencies shown in Table 5.1, and these values have also been adopted in the modal decomposition method. However, the natural frequencies found from the ABAQUS model deviates slightly from the target values, see Table 5.4, and hence resonance is not as pronounced in the ABAQUS model compared to the analytical solution using modal decomposition. The same arguments might apply to the experimental results as well in case that the natural frequencies have not been estimated totally correct, which is very likely.

9.4.2 Effect of Calculation Scheme

Differences in the actual natural frequencies between the used models in connection with the chosen jumping frequencies can potentially change the obtained results significantly. Nevertheless, this might not be the only reason for the deviating results obtained by the analytical solution and ABAQUS solution with Ellis & Ji, as the same force input has been used in the two methods.

Searching for another reason, an erroneous formulation of the modal decomposition technique used in the analytical solution and Newmark time integration could also explain the deviations. Therefore, in order to exclude this option, an analysis is run in ABAQUS, where modal decomposition is assumed as in the analytical solution and Newmark time integration. The ABAQUS solutions, which have been obtained so far, have used so-called direct integration of the equations of motion for each time step. This means that the equation of motions are solved for each time step. A comparison is shown in Figure 9.11, which is equivalent to Figure 9.3 and Figure 9.4 excluding experimental results.

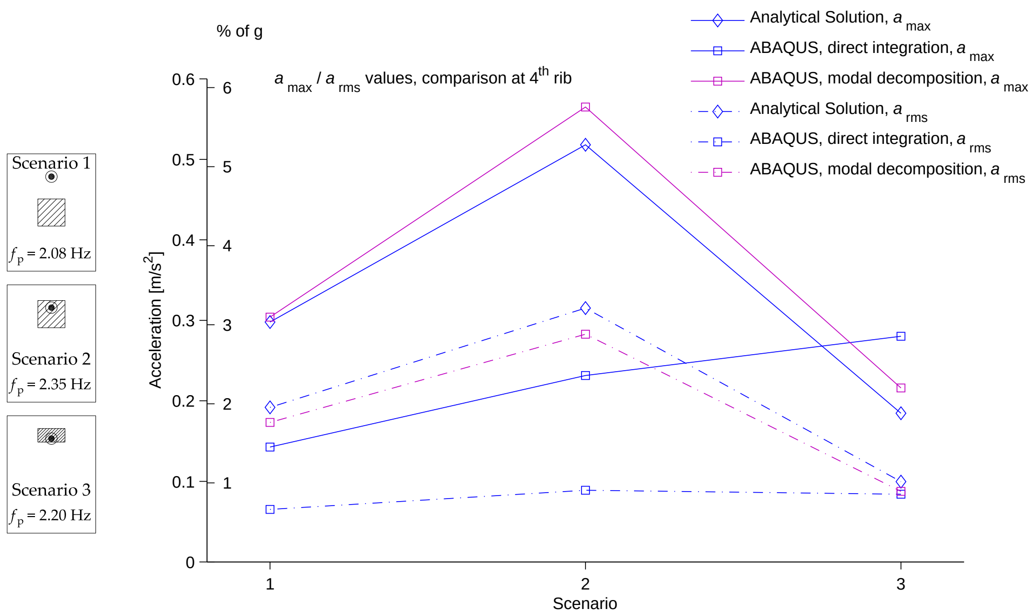

Figure 9.11: Comparison of modal decomposition techniques.

As seen from Figure 9.11 close agreement is found between the ABAQUS solution with modal decomposition and the analytical solution indicating a correct formulation of the analytical solution. Hence, the differences might instead be explained due to limitations in the modal decomposition technique compared to the more advanced direct integration. This can be supported by [5] in which it is stated that modal decomposition techniques generally yields inaccurate results if used in connection with shock loading. Human jumping loads might be considered as a series of shock impacts.

Chapter **10**

Critical Serviceability Scenarios

In this chapter it is examined whether the chosen load scenarios will cause acceleration levels which exceed the limits given in Eurocode. As stated in Chapter 9, it is found that ABAQUS *yields the best results and is therefore used in the following to evaluate the acceleration levels. Also the acoustic problem from the vibrations in the theatre hall is brought up for discussion with regard to a possible solution proposal.*

✦ ✦ ✦

10.1 Prediction of Acceleration Levels

The human perception of different acceleration levels is, as explained in Section 1.4, different from person to person, and no detailed list of acceleration limits is available. Therefore, the limits proposed in Eurocode are considered. The acceleration limits given in Eurocode state, that for the purpose of the floor in this project, the root-mean-square acceleration should be kept under 10 % of g.

As the data available for extrapolation is based on the chosen load scenarios in Chapter 6, it is merely investigated whether scenarios with the same jumping frequencies f_p = 2.08, 2.20, and 2.35 Hz can give rise to a serviceability problem.

The ABAQUS model using the Ellis & Ji load model is used for the analysis. This model has shown to yield quite accurate results for the a_{max}. However, the a_{rms}-values seem to be overestimated by this model. As the a_{max} results match the results of the experiments and the a_{rms} results are underestimated, it is assumed that the model is correct but that the synchronization of the jumpers in the experiments was of varying quality, which was also observed visually during the experiments.

To produce a method to predict possible critical serviceability scenarios, an examination of the a_{rms} for different load areas and load per unit area has been performed, where the load area is centered on the floor. The principle of the analyses is seen in Figure 10.1.

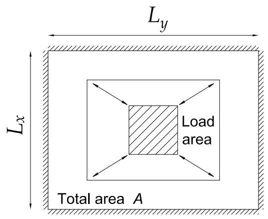

Figure 10.1: Principle of analyses with different load areas.

It was found in Section 8.4 that the largest acceleration at the 18 ribs was found in Scenario 2, i.e. with a jumping frequency of f_p = 2.35 Hz, which has its fourth load component to coincide with the second eigenmode of the deck. This is also the case when the jumpers are placed centered at the mid-point of the floor, which is probably due to the fact that the ABAQUS model predicts that the third eigenmode is present at 11.79 Hz ≈ 4·2.35 Hz. Hence, the analyses regarding possible critical serviceability scenarios are conducted with this jumping frequency.

As shown in Section 8.4, the a_{rms} results will scale linearly with the load per unit area in ABAQUS for five persons or more, as the equivalent contact ratio approach a maximum quickly in the conducted simulation, see Figure 7.5. This will add uncertainty to the extrapolation, however the linearity is accepted in the following, as scenarios involving less than five persons are not expected to be critical. Besides that, it is unknown how the equivalent contact ratio will change for large areas, i.e. it is not known whether the visual contact with larger groups will improve or worsen the ability to keep the same synchronization. Hence, this load model is used, keeping the uncertainties in mind.

Also the load area has been altered with its center at the mid-point of the floor. The a_{rms} will not scale linearly with the load area as loads near the boundary conditions will have smaller influence than loads at the mid-point. Therefore, several ABAQUS analyses have been run at the same load per unit area with the ABAQUS file `AccLimit.cae`. The dependency of the maximum a_{rms} of the deck with the load area as a percentage of the total area A with $940\,\text{N/m}^2$ is seen in Figure 10.2.

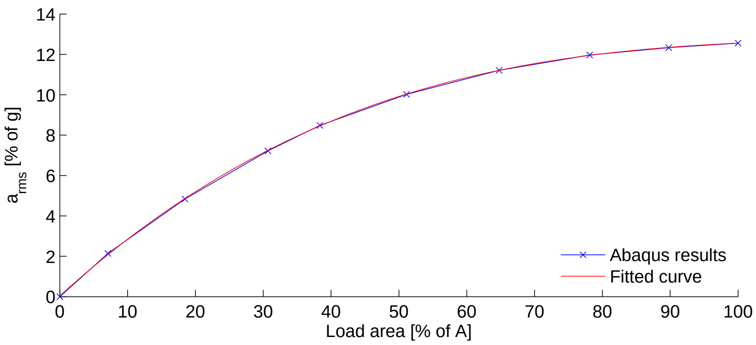

Figure 10.2: a_{rms} for different load areas with $940\,\text{N/m}^2$.

With the linearity between a_{rms} and load per unit area, and the fitted curve in Figure 10.2, a 3D plot has been made to present a visual representation of possible critical serviceability scenarios. The calculation for the prediction of acceleration levels is found in `LimitPrediction.m`. The plot is seen in Figure 10.3, where points that exceed the Eurocode a_{rms}-limit are marked with brown colour.

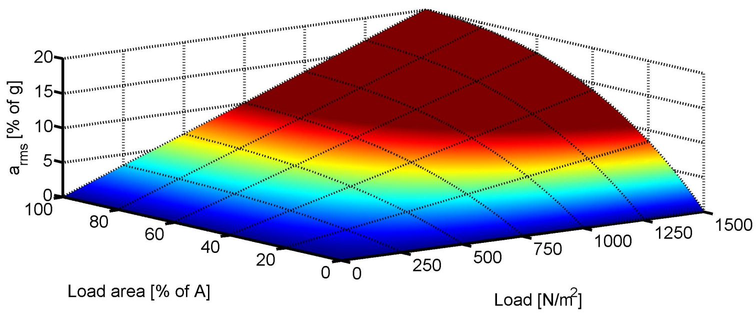

Figure 10.3: a_{rms} as a function of load area and load per unit area.

As seen in Figure 10.3, a dense crowd on a large area of the floor will most probably result in accelerations that exceed the limit stated in the Danish National Annex. E.g. if the whole floor is occupied with one person per m^2, or 2 persons per m^2 on an area of 25 % of the total floor area, it is likely that the acceleration limit is exceeded. However, it must be kept in mind that that this model might overestimate the a_{rms} for larger crowds.

To stress the importance of which load model is used, an analysis has been performed with the Eurocode load model with 1500 N/m^2 on the whole floor, which corresponds to the maximum a_{rms} in Figure 10.3. The result of the analysis was $a_{\text{rms}} = 5.46\,\%$ of g, which is approximately 27 % of the result using the Ellis & Ji load model, and would not mean that the acceleration limit in Eurocode is reached.

Although the results in Figure 10.3 give rise to the conclusion that the serviceability limits can be exceeded at scenarios that might occur in the sports hall, the results are based on extrapolations that induce great uncertainties to the prediction. Therefore, no final conclusion can be deduced, besides that there are possible serviceability problems with regard to the vibrations of the deck. To verify whether the results in this section are in agreement with the real response of the floor, further experiments should be performed with larger crowds, so a better understanding of the crowd reduction factor can be achieved.

10.2 Acoustics Solution Proposal

Though it was found in the previous matter, that an overstepping of the serviceability acceleration values is not very likely to happen during daily uses, two issues regarding the acoustics in the theatre hall were in fact observed during the experiments. Bearing in mind, that the cause of the authors' interest in the floor construction, which the project has revolved around, was awaken due to these noise issues in the theatre, a solution proposal with regard to the acoustics in the theatre is given in the following. It was concluded, that a TMD solution had to be designed based on ABAQUS modelling as to much uncertainties on the evaluated effect of the TMD were associated with using the modal decomposition method. Also it could be concluded that probably at least three modes had to be damped by TMDs, making the design even more complicated. Due to this fact, it was chosen to accept the vibrations of the deck and try to remove the sources of the noise by other means. The acoustic issues are:

- Transmission of impact sounds straight through the floor construction.
- Noise generation in lighting equipment caused by vibrations in the deck.

Even though the authors are not educated as acoustics experts, the two problems are assessed. The transmission of sound straight through the floor caused by impacts such as jumping humans or balls being hammered into the floor is assumed to be reduced by applying an additional ceiling solution. Several firms provide ceiling sheets solutions, which both reduces transmission through the sheets and reflections from within the room. This kind of ceiling solution in combination with sound insulation between the ribs is assumed to be able to limit the direct sound transmission, see Figure 10.4.

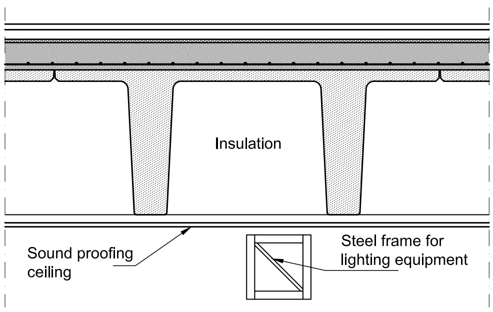

Figure 10.4: Sketch of sound proofing solution proposal.

Both the suggested new ceiling solution and the fact that the noise generated from the lighting equipment is caused by vibrations in the TTD elements indicates that the steel frames, from which the lighting hangs, need to be detached from the ribs. At the moment the steel frames are able to be attached to any given rib, giving the users of the theatre high flexibility when it comes to design of the lighting set-up. This is also taken into account in the suggested solution.

As the ribs will no longer be available for attaching the steel frames, an alternative method where abutments are built into the wall is suggested. The idea is to extend the steel frames so they span the 16.3 m across the theatre hall and support them on wheels, making the position of the frame customizable throughout the length of the hall. Alternatively, if the steel frames are not able to span 16.3 m from a load bearing point of view, a HEB 300 steel beam has been estimated to be able to carry the lighting rig in the same manner as the ribs do at this moment. The advantage of the set-up with only the steel frames is an increase in elevation of the lighting equipment, which was a concern of the theatre management when regarding a new ceiling design. A sketch of the proposed solution is shown in Figure 10.5.

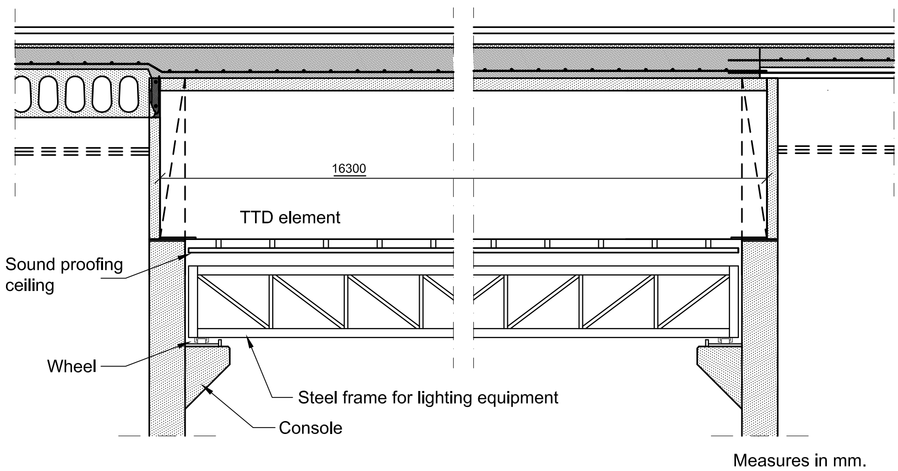

Figure 10.5: Sketch of lighting rig attachment solution proposal.

Chapter 11

Conclusion

The dynamic analysis of the deck in Nordkraft has been divided into two parts. At first a frequency analysis is performed in order to describe the dynamic properties of the structure. Thereafter a response analysis has been performed, where the vibrational response is found due to human-induced jumping loads and compared to the limit values given in the Danish National Annex to Eurocode. In both parts, analytical, numerical, and experimental methods are compared.

Frequency Analysis

Regarding analytical methods, plate models seem to be preferable in comparison with beam models for determination of natural frequencies as well as mode shapes. Beam models are only able to model the first vibration mode with sufficient precision, but are generally not good at predicting more vibration modes. This is due to the fact that the natural frequencies of the deck are spaced relatively close, and this is best modelled with a plate model. The deck has clear orthotropic stiffness properties due to the ribs of the TTD elements, and this should be incorporated in the used plate models. Also, modelling of the boundary conditions of the deck should be considered carefully as these have vital influence of the found natural frequencies.

In numerical modelling of the deck, plate models are also preferable compared to beam models, but also the distinction between a shell model and a solid model should be considered. Results for the two element types are relatively alike, but due to the heavy computations in relation to solid elements, the shell model seems to be sufficient in most cases.

In order to estimate the natural frequencies of the construction, experimental measurements have been performed on the deck by means of an accelerometer. A Fast Fourier Transform analysis of the measured acceleration signal has been used to find distribution of accelerations with respect to frequency. From the measurements, the natural frequencies seem to be detectable with relative good accuracy, whereas the obtained damping properties are more uncertain. Both the half-band width method and the logarithmic decrement method have been used to estimate damping properties of the deck structure.

Young's modulus of concrete E_c is relatively uncertain when used in dynamic calculations. Comparing with experimental measurements, a value of $E_c = 48\,\text{GPa}$ gives the best agreement with respect to natural frequencies when used in the numerical model. Young's modulus must be even bigger when used in an analytical model to get comparable natural frequencies. This is probably due to the fact that boundary conditions and plate effects not are modelled equally in numerical and analytical plate models. In the same manner, the stiffness of various kinds of reinforcement being prestressed cables or ordinary rebar should be included in a calculation model.

Response Analysis

The acceleration response has been assessed using two different load models for human-induced jumping loads. The simplest load model is the codified Danish load model, Eurocode-model, where three load components are included considering the energy content at integer multiplier frequencies of the jumping frequency. The other load model suggested by Ellis & Ji is used with six load components included. To establish realistic scenarios for the loading, three different load areas are defined on the deck in which humans are supposed to jump.

The two load models are used in connection with analytical solutions of the equations of motions, where modal decomposition is assumed to apply. In the modal decomposition technique, the three first vibration modes are used as these are the most relevant in connection with resonance from load components achieved with the chosen jumping frequencies at approximately 2.0 Hz. The load models are also used in a numerical shell model similar to the one used in the frequency analysis.

By comparing results from analytical and numerical methods with the experimental measurements, the numerical model using the Ellis & Ji load model gives the best agreement with the experimental results. Generally, it is observed that the Eurocode-model is less precise in the investigated load scenarios in this report. This can be explained by the number of included load components in the load model as resonance cannot be achieved for any of the first three load components for the chosen jumping frequencies. As a comment to this, due to the guidelines in connection with the Eurocode-model, a jumping frequency higher than $f_\mathrm{p} = 3.0\,\mathrm{Hz}$ should not be investigated, and hence resonance cannot be achieved for constructions with a fundamental frequency higher than 9.0 Hz. For this specific construction it is obvious that a load model with only three load components is not suitable for most of the normal jumping frequencies and more load components should be considered to investigate possible resonance phenomena.

Experimental results reveal that synchronization between the jumping humans is very important for the magnitude of the applied jumping load and hence acceleration response. A suitable way of taking this crowd reduction effect into account in the Ellis & Ji-model for six load components has been sought for, however total success has not been achieved. The Eurocode-model already suggests one method for reducing the total load due to the crowd reduction effect, but this is only applicable for the three first load components. Nevertheless, the crowd reduction effect should in some manner be addressed in a calculation model.

Finally, by using the numerical method together with the Ellis & Ji load model, it is found that unacceptable accelerations can be generated by human jumping loads. E.g. assuming the deck fully occupied by humans with a intensity of minimum $750\,\mathrm{N/m^2}$, corresponding to approximately one human per square metre, the limit acceleration may be exceeded. Here, uncertainty of the crowd reduction effect should be kept in mind, as this seems to be quite conservatively estimated. On the contrary, using the same jumping frequency and intensity of jumping humans with the Eurocode-model, the magnitude of vibrations are found acceptable.

In all performed analyses it is found crucial to consider the used input parameters carefully. The calculated acceleration is dependent on relatively many assumptions, which makes the final results quite sensitive towards choices made throughout the analysis process. In addition to this, it is important to remember that the accelerations measured in the experiments are measured from the underside of the deck. Therefore, these accelerations are not necessarily representing what is felt by humans on top of the deck.

Appendices

Appendix **A**

Energy Methods

In this appendix, the application of two related approximative procedures is described. First, Rayleigh's fraction for estimating frequencies of a structure is touched upon. Hereafter, an extension of this method, the Rayleigh-Ritz method, is briefly described. Generally the Rayleigh fraction only determines the natural frequency for the chosen mode shape, whereas also other frequencies can be estimated by the Rayleigh-Ritz method. The methods are so-called energy methods, where the results rely on the formulation of potential and kinetic energy of the system.

Both methods are applicable to both single degree of freedom systems, discrete systems, and continuous systems. The starting point of the methods is Rayleigh's principle, which can be formulated in the following way [21]:

> "*The frequency of vibration of a conservative system vibrating about an equilibrium position has a stationary value in the neighbourhood of a natural mode. This stationary value, in fact, is a minimum value in the neighbourhood of the fundamental natural mode.*"

In other words, the result of Rayleigh's fraction and the Rayleigh-Ritz method will always yield a frequency, which represents an upper bound to the natural frequency, which is estimated.

A.1 Rayleigh's Fraction

Because the deck considered in this project is a continuous system, the properties of Rayleigh's fraction will be explained based on a general continuous system. However, the arguments and approximations related to Rayleigh's fraction are the same no matter the number of degrees of freedoms in the system. When using Rayleigh's fraction, the first step is to assume a shape function to describe the mode of vibration, which is designated $u(x, y, t)$. The assumed mode of vibration can be stated as shown in Eq. (A.1).

$$u(x, y, t) = \Phi(x, y)\cos(\omega t) \tag{A.1}$$

The function $\Phi(x, y)$ is the mode shape of the evaluated mode, and if for instance the plate is simply supported, the mode shape for mode m in the x-direction and n in the y-direction might be stated as:

$$\Phi(x, y) = \sin\left(m\pi\frac{x}{L_\mathrm{x}}\right)\sin\left(n\pi\frac{y}{L_\mathrm{y}}\right) \tag{A.2}$$

Hereafter, the potential energy U and the kinetic energy T are formulated for the considered structure. The expressions for the energies of beams, isotropic plates, and orthotropic plates are given in Eq. (A.3a), (A.3b), and (A.3c), respectively [4, 27, 6].

Beam:

$$U = \frac{1}{2} EI \int_{L_x} \left(\frac{\partial^2 u}{\partial x^2} \right)^2 dx \qquad T = \frac{1}{2} \rho A \int_{L_x} \dot{u}^2 dx \tag{A.3a}$$

Isotropic plate:

$$U = \frac{1}{2} D \iint_A \left[\left(\frac{\partial^2}{\partial x^2} \right)^2 + \left(\frac{\partial^2 u}{\partial y^2} \right)^2 + 2\nu \frac{\partial^2 u}{\partial x^2} \frac{\partial^2 u}{\partial y^2} + 2(1-\nu) \left(\frac{\partial^2 u}{\partial x \partial y} \right)^2 \right] dx dy$$

$$T = \frac{1}{2} \rho t \iint_A \dot{u}^2 dx dy \tag{A.3b}$$

Orthotropic plate:

$$U = \frac{1}{2} \iint_A \left[D_x \left(\frac{\partial^2 u}{\partial x^2} \right)^2 + 2\nu D_y \frac{\partial^2 u}{\partial x^2} \frac{\partial^2 u}{\partial y^2} + D_y \left(\frac{\partial^2 u}{\partial y^2} \right)^2 + 4 D_{xy} \left(\frac{\partial^2 u}{\partial x \partial y} \right)^2 \right] dx dy$$

$$T = \frac{1}{2} \rho t \iint_A \dot{u}^2 dx dy \tag{A.3c}$$

If beams, which is the simplest case, are considered, the second sine function in Eq. (A.2) can be disregarded. To evaluate the maximum energies, the expressions for energy levels for a beam, Eq. (A.3a), are considered:

$$U = \frac{1}{2} EI \int_{L_x} \left(\frac{\partial^2 u}{\partial x^2} \right)^2 dx = \frac{1}{2} EI \int_{L_x} \left(\frac{\partial^2}{\partial x^2} \Phi(x,y) \cos(\omega t) \right)^2 dx$$

$$\Rightarrow \quad U_{\max} = \frac{1}{2} EI \int_{L_x} \left(\frac{\partial^2 \Phi}{\partial x^2} \right)^2 dx \tag{A.4}$$

$$T = \frac{1}{2} \rho A \int_{L_x} \dot{u}^2 dx = \frac{1}{2} \rho A \int_{L_x} \left(\frac{\partial}{\partial t} \Phi(x,y) \cos(\omega t) \right)^2 dx = \frac{1}{2} \rho A \int_{L_x} \Phi^2(x,y) \omega^2 \sin^2(\omega t) dx$$

$$\Rightarrow \quad T_{\max} = \frac{1}{2} \omega^2 \rho A \int_{L_x} \Phi^2 dx \tag{A.5}$$

Assuming that no energy is lost, the maximum potential energy $U_{\max}$ and kinetic energy $T_{\max}$ can be equated, and hence derive an expression for the circular frequency for the chosen mode shape:

$$U_{\max} = T_{\max} \quad \Rightarrow \quad \omega = \sqrt{\frac{EI \int_{L_x} \left(\frac{\partial^2 \Phi}{\partial x^2} \right)^2 dx}{\rho A \int_{L_x} \Phi^2 dx}} \quad \Rightarrow \quad \omega = \sqrt{\frac{k}{m}} \tag{A.6}$$

As the $\frac{1}{2}$ from the energies cancels out, this fraction is also recognized as the ratio between modal stiffness and modal mass. This procedure also applies to plates.

The assessed deck in the report can be considered to consist of both a plate and stiffening beams. Therefore, the modal stiffnesses and modal masses are summed for the beams, $i = 1, 2, \ldots 18$, and the plate, and the shape function in Eq. (A.2) is used. The calculation of the natural frequencies is presented in Eq. (A.7).

$$
\begin{aligned}
k_{mn} =& D\iint_A \left[\left(\frac{\partial^2\Phi}{\partial x^2}\right)^2 + \left(\frac{\partial^2\Phi}{\partial y^2}\right)^2 + 2\nu\frac{\partial^2\Phi}{\partial x^2}\frac{\partial^2\Phi}{\partial y^2} + 2(1-\nu)\left(\frac{\partial^2\Phi}{\partial x\partial y}\right)^2\right] dxdy \\
&+ EI\sum_i \int_{L_x}\left(\frac{\partial^2\Phi(x,y_i)}{\partial x^2}\right)^2 dx \\
=& \frac{\pi^4 D}{4L_x^3L_y^3}\left(n^2L_x^2 + m^2L_y^2\right)^2 + \frac{\pi^4 m^4 EI}{2L_x^3}\sum_i \sin^2\left(n\pi\frac{y_i}{L_y}\right) \\
m_{mn} =& \rho t\iint_A \Phi^2 dxdy + \rho A\sum_i\int_{L_x}\Phi^2 dx \\
=& \frac{1}{4}\rho t L_x L_y + \frac{1}{2}\rho A L_x \sum_i \sin^2\left(n\pi\frac{y_i}{L_y}\right)
\end{aligned}
$$

$$
\omega_{mn} = \sqrt{\frac{k_{mn}}{m_{mn}}} = \frac{\pi^2}{L_x^2}\sqrt{\frac{\frac{D}{2L_y^3}\left(n^2L_x^2 + m^2L_y^2\right)^2 + m^4 EI\sum_i \sin^2\left(n\pi\frac{y_i}{L_y}\right)}{\frac{1}{2}\rho t L_y + \rho A\sum_i \sin^2\left(n\pi\frac{y_i}{L_y}\right)}} \tag{A.7}
$$

A.2 Rayleigh-Ritz's Method

Rayleigh's fraction can be extended into the Rayleigh-Ritz method by choosing several shape functions instead of just one and performing a minimization process of the natural frequency. Therefore, the displacement field of the Rayleigh-Ritz method can generally be stated as in Eq. (A.8).

$$
\Phi(x,y) = a_1\phi_1 + a_2\phi_2 + a_3\phi_3 + \ldots + a_p\phi_p + \ldots + a_P\phi_P \tag{A.8}
$$

The functions ϕ_1, ϕ_2, $\phi_3,\ldots,\phi_P$ should be linear independent functions, and each term must satisfy the boundary conditions of the plate problem. The constants a_1, a_2, $a_3,\ldots,a_P$ must be determined such that the expression in Eq. (A.8) reassembles the wanted modes as closely as possible.

When a linear combination of shape functions have been proposed as in Eq. (A.8), this expression is substituted into Rayleigh's fraction, Eq. (A.6). Then, the problem is solved by differentiating the squared circular frequency ($\omega^2 = k/m$) with respect to each of the unknown constants a_1, a_2, $a_3,\ldots,a_P$ and equating each term to zero, Eq. (A.9).

$$
\frac{\partial\omega^2}{\partial a_p} = \frac{m\frac{\partial k}{\partial a_p} - k\frac{\partial m}{\partial a_p}}{m^2} = 0 \qquad p = 1,2,\ldots,P \tag{A.9}
$$

The system of equations may be rewritten as stated in Eq. (A.10).

$$
\frac{\partial k}{\partial a_p} - \frac{k}{m}\frac{\partial m}{\partial a_p} = \frac{\partial k}{\partial a_p} - \omega^2\frac{\partial m}{\partial a_p} = 0 \qquad p = 1,2,\ldots,P \tag{A.10}
$$

By using Eq. (A.8) in the expressions for modal mass m and modal stiffness k and substituting this into Eq. (A.10), these equations can be reformulated as a classic eigenvalue problem as shown in

Eq. (A.11).

$$\mathbf{\Omega}\,\mathbf{a} = \mathbf{0} \qquad \Leftrightarrow \qquad \begin{bmatrix} \Omega_1\left(\omega^2, a_1\right) & \dots & \Omega_1\left(\omega^2, a_P\right) \\ \vdots & \ddots & \vdots \\ \Omega_P\left(\omega^2, a_1\right) & \dots & \Omega_P\left(\omega^2, a_P\right) \end{bmatrix} \begin{bmatrix} a_1 \\ \vdots \\ a_P \end{bmatrix} = \begin{bmatrix} 0 \\ \vdots \\ 0 \end{bmatrix} \tag{A.11}$$

The entries of each row in $\mathbf{\Omega}$ are obtained by ordering the terms of Eq. (A.10). The natural frequencies are then found by setting $\det(\mathbf{\Omega}) = 0$. It is obvious, when looking at the dimension of the matrix $\mathbf{\Omega}$ in Eq. (A.11), that the number of natural frequencies that can be determined is limited by the number of functions ϕ_p chosen for the shape function Φ, and therefore, at most the P lowest modes can be estimated from the Rayleigh-Ritz method.

For both procedures described, it is evident that the accuracy of the estimated frequencies is improved by using shape functions, which are very close to the exact vibration shape of the structure. However, simple functions like polynomials and trigonometric series, which are used here, are preferable in order to minimize the complexity of the calculations.

Appendix **B**

Determination of Plate Rigidities

In this appendix the determination of the necessary plate rigidities entering the governing differential equation and various energy methods is described as well as other constants, which must be found in order to treat the plate vibration problem by analytical methods.

In order to solve the 4^{th} order differential equation of a vibrating orthotropic plate, the following plate rigidities, densities and moment of inertias must be found at first:

D_{x}	Flexural stiffness in the x-direction.
D_{y}	Flexural stiffness in the y-direction.
D_{xy}	Torsional stiffness of an orthotropic plate.
H	Effective torsional stiffness given by $H = \nu D + 2D_{\mathrm{xy}}$.
$\overline{\rho}$	Equivalent mass per unit area of orthotropic plate.
J_{x}	Mass moment of inertia per unit area, in x-direction.
J_{y}	Mass moment of inertia per unit area, in y-direction.

Using a method described by Iyengar [14], the plate rigidities and equivalent mass are found via an approximate approach. In this method, the boundary conditions and mode shapes are taken into account by use of beam eigenfunctions, i.e. functions describing the mode shape of the plate in two perpendicular directions, and naturally the choice of functions must reflect the given boundary conditions. Using beam eigenfunctions instead of plate eigenfunctions is an approximation, thus, by a good choice of beam eigenfunctions, the error should be of minimum importance [14]. An illustration of the orthotropic plate with designation of parameters is shown in Figure B.1.

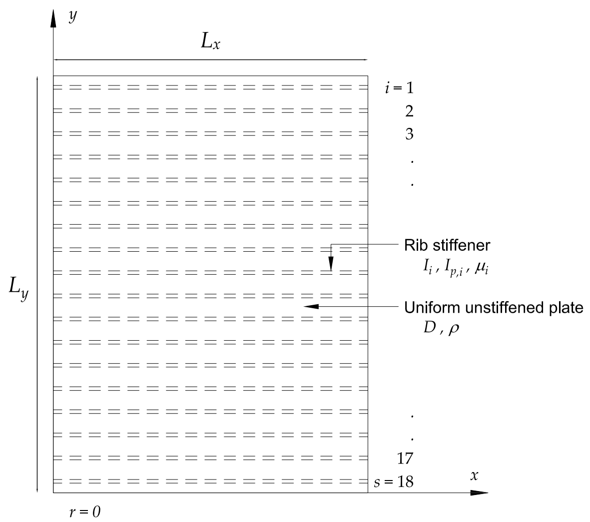

Figure B.1: Plate with stiffeners.

Generally speaking, the plate deflection in a given mode is assumed on the form given by Eq. (B.1), where a beam eigenfunction $\Phi_m(x)$ describes the shape of the plate in the x-direction, while a beam eigenfunction $\Phi_n(y)$ describes the shape in the y-direction. A_{mn} is a constant. m

and n refers to the mode of interest, and designates the number of half-sine waves in the x- and y-direction, respectively.

$$u(x,y) = A_{mn}\Phi_m(x)\Phi_n(y) \tag{B.1}$$

The individual plate rigidities are obtained from the following formulae, Eq. (B.2). s and r are the numbers of stiffeners in the x- and y-direction, respectively. Therefore, as only stiffeners in the x-direction are present for the deck, $s = 18$ due to two stiffeners per TTD element, while $r = 0$. y_i and x_j should be understood as the coordinate value at stiffener i and j, respectively.

$$\begin{aligned}
D_\mathrm{x} &= D + \frac{E}{L_\mathrm{y}}\sum_{i=1}^{s} I_i \Phi_n(y_i)^2 \\
D_\mathrm{y} &= D + \frac{E}{L_\mathrm{x}}\sum_{j=1}^{r} I_j \Phi_m(x_j)^2 \\
D_\mathrm{xy} &= \frac{D(1-\nu)}{2} + \frac{G}{4}\left(\frac{\sum_{i=1}^{s} I_{\mathrm{p},i}\left(\Phi'_n(y_i)\right)^2}{\int_0^{L_\mathrm{y}} \Phi'_n(y)dy} + \frac{\sum_{j=1}^{r} I_{\mathrm{p},j}\left(\Phi'_m(x_j)\right)^2}{\int_0^{L_\mathrm{x}} \Phi'_m(x)dx} \right) \\
\bar{\rho} &= \rho t + \frac{1}{L_\mathrm{y}}\sum_{i=1}^{s} \mu_i \Phi_n(y_i)^2 + \frac{1}{L_\mathrm{x}}\sum_{j=1}^{r} \mu_j \Phi_m(x_j)^2
\end{aligned} \tag{B.2}$$

where

D	Flexural stiffness of uniform unstiffened plate, $D = Et^3/(12(1-\nu^2))$.
t	Thickness of uniform plate, $t = 220\,\mathrm{mm}$.
E, G	Young's modulus and shear modulus, respectively.
ν	Poisson's ratio, taken as $\nu = 0.2$ for concrete.
I_i, I_j	Moment of inertia of stiffeners in x- and y-direction.
$I_{\mathrm{p},i}, I_{\mathrm{p},j}$	Polar moment of stiffeners in x- and y-direction. As there are only stiffeners in the x-direction, only $I_{\mathrm{p},i}$ is relevant, which is calculated as $I_{\mathrm{p},i} = I_i + I_{i,\mathrm{weak}}$, where $I_{i,\mathrm{weak}}$ is the moment of inertia about an axis running through 0 on the x-axis in Figure B.3 [16].
μ_i, μ_j	Mass per unit length of stiffeners in x- and y-direction.
ρ	Density.

The application of these formulae is of course dependent of the chosen beam eigenfunctions entering Eq. (B.1), which must reflect the considered boundary conditions. Likewise, the output of the formulae is very dependent on the used moment of inertia. To illustrate this, two different moment of inertias are used in the calculation of the plate rigidities, which are calculated using the script `Transformed_I.m`. In Case 1, the moment of inertia is calculated taking into account the prestressed lines in the TTD element. The area of the prestressed cables are multiplied by $\epsilon = E_\mathrm{s}/E_\mathrm{c}$, where $E_\mathrm{s} = 200\,\mathrm{GPa}$ is Young's modulus of steel, while $E_\mathrm{c} = 40\,\mathrm{GPa}$ is Young's modulus of concrete. By this, an attempt is made to take into account the increased stiffness from the prestressed cables. In Case 2, the prestressed cables in the rib stiffener are disregarded. In both cases, the moment of inertia is calculated with respect to the combined neutral axis of the TTD cross section plus 150 mm concrete topping. The two different cases are shown in Figure B.2 and Figure B.3, respectively. The shown moment of inertia will be used in the following calculations whenever necessary. For an orthotropic plate, simply supported on all its boundaries, the beam eigenfunctions shown in Eq. (B.3) might be used in accordance with Eq. (B.1).

$$\Phi_m(x) = \sin\left(m\pi\frac{x}{L_\mathrm{x}}\right) \qquad \Phi_n(y) = \sin\left(n\pi\frac{y}{L_\mathrm{y}}\right) \tag{B.3}$$

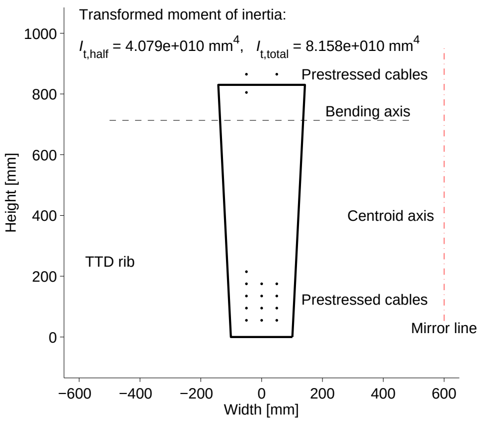

Figure B.2: Case 1.

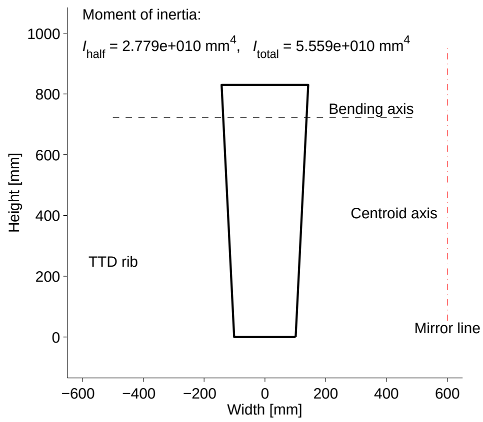

Figure B.3: Case 2.

The calculations of the plate rigidities are performed in `Determine_plate_par.m` and the results are shown for the two different cases of moment of inertia in Table B.1.

	Case 1	Case 2	
D_x	7.17×10^8	5.00×10^8	Nm
D_y	3.70×10^7	3.70×10^7	Nm
D_{xy}	1.60×10^8	1.15×10^8	Nm
H	3.27×10^8	2.37×10^8	Nm
$\bar{\rho}$	922.11	922.11	kg/m^2

Table B.1: Plate rigidities, 1st vibration mode ($m = 1$, $n = 1$).

The mass moment of inertia is found using the expressions of Eq. (B.4) and Eq. (B.5). In the calculations, a density of $\rho = 2400\,\mathrm{kg/m^3}$ is used for the whole cross section.

$$J_x = \frac{\rho}{b_c + 2b_s}\left[\frac{b_c t^3}{12} + \frac{t b_c^3}{12} + b_c t\left(d - \frac{t}{2}\right)^2 + \frac{2b_s h_s^3}{12} + \frac{2h_s b_s^3}{12} + 2b_s h_s\left(d - \frac{h_s}{2}\right)^2 + 2b_s h_s\left(\frac{b_s + b_c}{2}\right)^2\right]$$
$$\text{in which} \qquad d = \frac{b_c t^2 + 2b_s h_s^2}{2\,(b_c t + 2b_s h_s)} \tag{B.4}$$

$$J_y = \frac{\rho}{w}\left[\frac{1}{12}h\left(6a\eta^2 + 6\eta^2 b + ah^2 + 3bh^2 - 4a\eta h - 8\eta bh\right) + \frac{1}{12}wt^3 + wt\left(h_s - \eta - \frac{t}{2}\right)^2\right]$$
$$\text{in which} \qquad \eta = \frac{\frac{1}{6}h^2(a+2b) + wt\left(h + \frac{t}{2}\right)}{\frac{1}{2}(a+b)h + wt} \tag{B.5}$$

It should be noted that J_x is found using an expression from [28] assuming that the rib stiffeners have a rectangular cross section instead of an trapezoidal cross section. Averaging over the width from top to bottom of the rib, the following geometric measures are defined: $b_c = 956.50\,\mathrm{mm}$ and $b_s = 121.75\,\mathrm{mm}$. The parameters used to determine the second moment of masses are defined in Figure B.4.

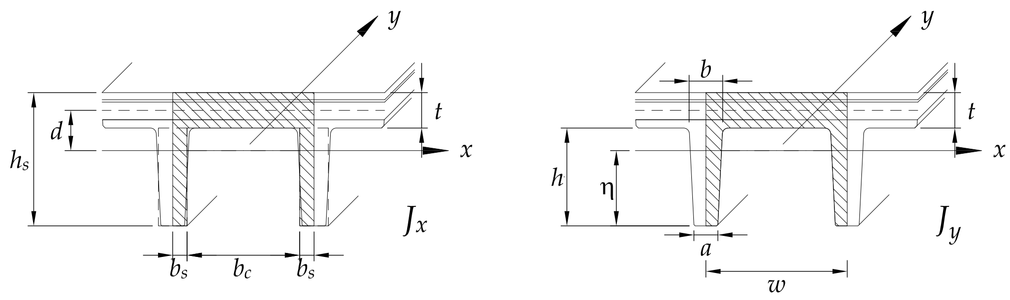

Figure B.4: Definition of parameters.

As earlier mentioned, the thickness of the plate t is taken as all layers until the floor layer when calculating parameters regarding mass. Therefore, the mass moment of inertia is calculated with a thickness of $t = 300\,\mathrm{mm}$. The calculations of the second moment of masses per unit area can be seen in `Analytical_frequency_of_plate_model.xmcd`, and the results are:

$$J_\mathrm{x} = 315.6\,\frac{\mathrm{kg\,m^2}}{\mathrm{m^2}} \qquad\qquad J_\mathrm{y} = 104.3\,\frac{\mathrm{kg\,m^2}}{\mathrm{m^2}}$$

Appendix **C**

Fast Fourier Transformation

In this appendix the Fast Fourier Transform analysis method used for evaluation of the measured acceleration response of the deck is described. The matter of the appendix is based on [1].

Consider any measured or generated response signal $X(t)$. It is presumed that the signal is periodic in the interval T_0, see Figure C.1.

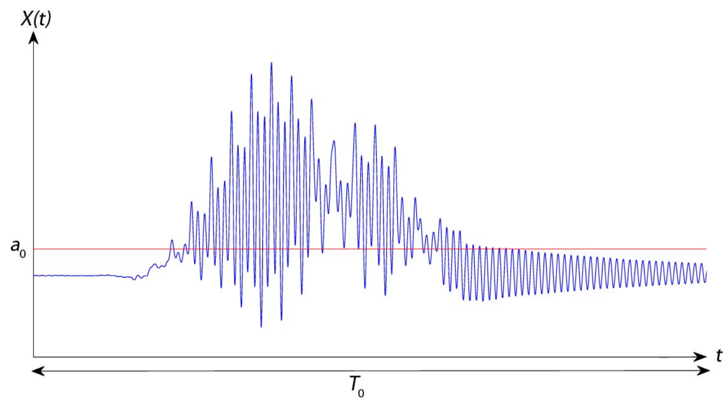

Figure C.1: Arbitrary response function of time.

Any continuous periodic function can be decomposed into a number of harmonic components by means of a Fourier series expansion, see Eq. (C.1).

$$\begin{aligned} X(t) &= a_0 + 2\sum_{i=1}^{H}\left(a_i \cos\left(\frac{2\pi i}{T_0}t\right) + b_i \sin\left(\frac{2\pi i}{T_0}t\right)\right) \\ &= a_0 + 2\sum_{i=1}^{H}\left(a_i \cos(\omega_i t) + b_i \sin(\omega_i t)\right) \end{aligned} \tag{C.1}$$

Here a_i and b_i are Fourier coefficients given by Equation C.2.

$$\begin{aligned} a_i &= \frac{1}{T_0}\int_0^{T_0} x(t)\cos(\omega_i t)\,dt \\ b_i &= \frac{1}{T_0}\int_0^{T_0} x(t)\sin(\omega_i t)\,dt \\ &\text{for} \quad i = 0, 1, \ldots, H-1 \end{aligned} \tag{C.2}$$

An alternative way of writing the i^{th} component of the signal is:

$$X(t) = A_i \sin(\omega_i t + \phi_i) \tag{C.3}$$

Here the estimation of the Fourier series terms is made by:

Amplitude	$A_i = \sqrt{a_i^2 + b_i^2}$
Phase angle	$\phi_i = \tan^{-1}\left(\frac{a_i}{b_i}\right)$
Angular frequency	$\omega_i = \frac{2\pi i}{T_0}$
Period	$T_i = \frac{2\pi i}{\omega_i}$
Frequency	$f_i = \frac{1}{T_i}$

for $\quad i = 0, 1, \ldots, H-1$

Therefore, having a series of response values with the sampling frequency f_s, a discrete time series is obtained. The total number of values $H = T_0 f_s$ is equal to the number of Fourier coefficients. The Fourier coefficients are obtained by the use of the Fast Fourier Transform (FFT) function in MATLAB. After determining the necessary parameters, an amplitude spectrum is presented in Figure C.2.

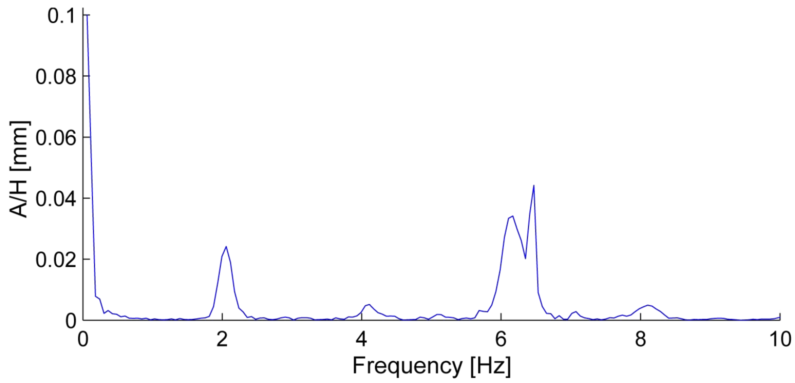

Figure C.2: Amplitude spectrum corresponding to the signal $X(t)$.

It should be noted that the presented spectrum has to be cut with the Nyquist frequency f_N. The Nyquist frequency is the frequency corresponding to where the first half of the total number of values are present. The reason for this is that the determined coefficients (a_i,b_i) contains two parts. The first half from 1 to H/2-1 is estimating the true components and the second part from H/2 to H-1 is the aliasing components. The explained procedure can be found in the MATLAB-script `FFT.m`.

Appendix **D**

Test of Jumping Accuracy

A series of jumping tests has been performed in order to test how precise a person can jump when listening to a specific music beat. In this appendix, a statistical description of a person's jumping frequency is sought for. A person's ability to follow a specific beat is of interest, for example in connection with an experiment, where human-induced jumping loads are used. The results from this appendix is used in a Monte Carlo simulation, which treats the synchronization between numerous jumping people.

This question is tested with two persons, designated P1 and P2, via the set-up seen in Figure D.1. The experiment set-up consists of a steel plate, which is placed on two wooden supports. An accelerometer is placed on the plate by means of a magnet, and the output from the accelerometer is sampled by a computer.

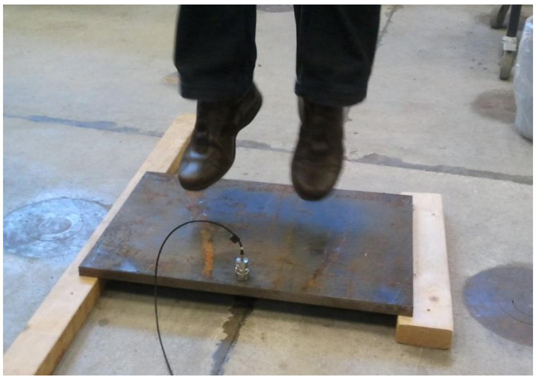

Figure D.1: Experiment set-up.

During the sampling of data, a piece of music was playing with a known overall beat frequency, and for each frequency, P1 and P2 jumped on the plate in time with the music. It is assumed that the beat frequency of the used music pieces is constant, otherwise variations in the beat frequency of the music will influence the results. On the other hand, small variations in the beat frequency might serve as a very realistic situation. It was attempted to find music pieces with a very constant beat. For each frequency, the experiment was repeated 5 times for both P1 and P2. The tested frequencies are shown in Table D.1.

Beat frequencies [Hz]					
P1 / P2	1.5	1.9	2.0	2.1	2.5

Table D.1: Tested beat frequencies.

An example of a signal can be seen in Figure D.2. The signal exhibits a characteristic peak each time the person hits the plate, and from the distance between these peaks, the period T_p of the jumping cycle is calculated. Finally, the jumping frequency is found as $f_\mathrm{p} = \frac{1}{T_\mathrm{p}}$. Thereby, a value of the jumping frequency f_p is found for each jump.

It should be noted that only peaks higher than a certain threshold have been used in the analysis, so noise does not affect the results. This data treatment is done in the file `Chi2goodness_`

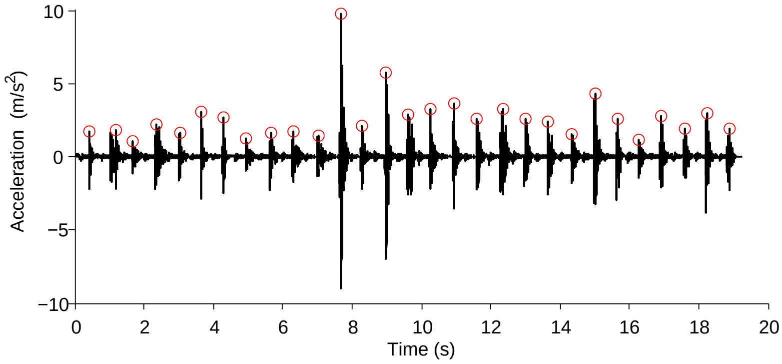

Figure D.2: Example of acceleration signal from 1.5 Hz jumping test.

`fit.m`. For each test, a number of jumping frequencies are obtained, and one sample will be regarded as the combination of the five test results within each frequency for each person. This gives 10 samples in total. The total number of data values N_{tot}, the mean value $\overline{X}$, and standard deviation S for each of the 10 samples are shown in Table D.2.

BEAT FREQUENCY	P1			P2		
[Hz]	N_{tot} [-]	$\overline{X}$ [Hz]	S [Hz]	N_{tot} [-]	$\overline{X}$ [Hz]	S [Hz]
1.5	77	1.54	0.13	114	1.54	0.15
1.9	141	1.90	0.10	139	1.90	0.16
2.0	184	2.02	0.14	145	2.01	0.14
2.1	162	2.13	0.16	150	2.11	0.21
2.5	138	2.53	0.20	170	2.51	0.22

Table D.2: Characteristics of test samples.

Besides from describing the data by the mean value and the standard deviation, a chi-square test for goodness of fit is performed [2]. This is done in order to estimate the statistical distribution of the population from which the jumping samples are drawn. Before the chi-square test is performed, the data samples must be defined specifically. By this is meant that some of the jumping frequencies obtained from the data sampling might be erroneous, e.g. due to sampled jumps in the start and end of each test, which were not in time with the music. It is not totally clear how to define a limit, over which a data sample should be rejected. However, two different cases are considered to illustrate this circumstance as illustrated by the two histograms shown in Figure D.3 and Figure D.4 from the jumping test at 2.0 Hz of person P2. In Figure D.3 all data samples within the region of: $\overline{X} \pm 4 \cdot S$ are used, whereas in Figure D.4 only data within the region: $\overline{X} \pm 2 \cdot S$ is used. $\overline{X}$ is the sample mean value, and S is the standard deviation of the total sample.

These two limits are applied on all of the 10 samples, and the chi-square test for goodness of fit is performed. Two distributions are tested for, namely the normal distribution and lognormal distribution. The steps in the chi-square test can be summarized in the following way.

1. The null hypothesis H_0 and the alternative hypothesis H_A are defined for both the test of the normal distribution and the lognormal distribution. The null and alternative hypothesis should be defined in such a way that if the null hypothesis must be rejected, the alternative hypothesis must be accepted. The null and alternative hypothesis for the test of the normal distribution are formulated as follow:

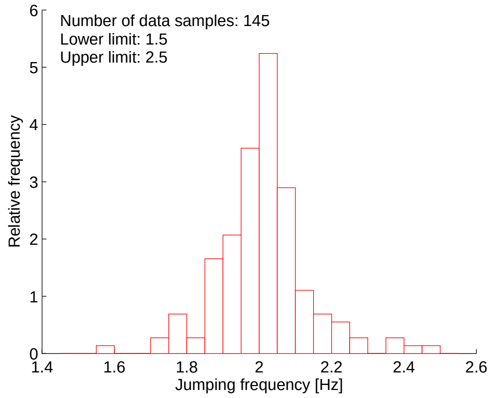

Figure D.3: Histogram from 2.0 Hz jumping test for P2, limit: $\overline{X} \pm 4 \cdot S$.

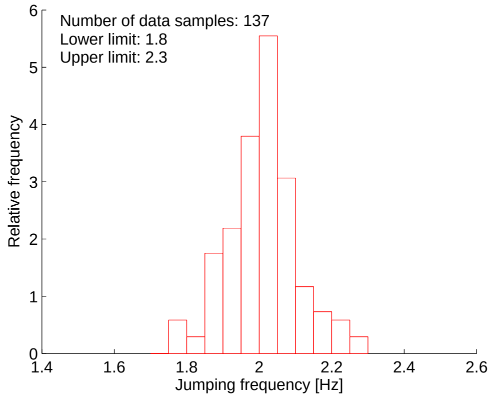

Figure D.4: Histogram from 2.0 Hz jumping test for P2, limit: $\overline{X} \pm 2 \cdot S$.

H_0 The jumping frequencies can be characterized by a normal distribution, $X \sim N(\mu_N, \sigma_N^2)$, where μ_N and σ_N are estimated by means of maximum likelihood from the sample data.

H_A The jumping frequencies cannot be characterized by a normal distribution, $X \sim N(\mu_N, \sigma_N^2)$.

The null and alternative hypothesis for the test of the lognormal distribution are formulated in a similar way:

H_0 The jumping frequencies can be characterized by a lognormal distribution, $X \sim LN(\mu_{LN}, \sigma_{LN}^2)$, where μ_{LN} and σ_{LN} are estimated by means of maximum likelihood from the sample data.

H_A The jumping frequencies cannot be characterized by a lognormal distribution, $X \sim LN(\mu_{LN}, \sigma_{LN}^2)$.

The two pairs of hypotheses are tested on all of the 10 samples. It should be noticed that rejection of the null hypothesis does not necessarily imply that the jumping frequencies are not normal or lognormal distributed, but it could also be due to the fact that μ_N and σ_N or μ_{LN} and σ_{LN} are incorrectly estimated. The maximum likelihood estimations of the distribution parameters are obtained from a built-in MATLAB function.

2. The chi-square test is based on a comparison of the expected count E_i and the observed count O_i within each interval of the tested histogram, see for example Figure D.3 or Figure D.4. The expected count is calculated from the assumed distribution function in the null hypothesis, while the observed count naturally is given by the data sample. In the chi-square test, the following test statistic is used:

$$\chi^2 = \sum_{i=1}^{k} \frac{(O_i - E_i)^2}{E_i}$$

The value of the test statistic χ^2 is compared with the critical value of the chi-square distribution $\chi^2_{\alpha,k-j}$. α is the level of significance, and $k-j$ is the degrees of freedom. k is the number of discrete intervals in the tested histogram, and j is in this case 3. One degree of freedom is lost because the data sample is used to find the expected count, and furthermore two degrees of freedom are lost because μ_N and σ_N or μ_{LN} and σ_{LN} are estimated from the data sample.

3. The level of significance is chosen to 5 %.

4. When the level of significance is determined, the test statistic χ^2 and the critical value $\chi^2_{\alpha,k-j}$ can be calculated. The null hypothesis is accepted, if the test statistic χ^2 is smaller than the critical value $\chi^2_{\alpha,k-j}$. Otherwise, the alternative hypothesis must be accepted.

In total, 40 chi-square tests for goodness of fit have been performed as two distributions have been tested and for two different filtering cases of the samples as explained in relation to Figure D.3 and Figure D.4. The calculations are performed in `Chi2goodness_fit.m` and the results are summarized in Table D.3 for person P1, and in Table D.4 for person P2. In the tables, the designations $\overline{X}_r$ and S_r are used for the mean value and standard deviation of the filtered samples, i.e. after applying $\overline{X} \pm 4 \cdot S$ or $\overline{X} \pm 2 \cdot S$ to the total sample.

Frequency 1.5 Hz (Data points, intervals)	Distribution	$\overline{X}_r$ [Hz]	S_r [Hz]	Accepted hypothesis
$\overline{X} \pm 4 \cdot S$, (76,8)	$N(1.54, 0.11^2)$ $LN(0.43, 0.07^2)$	1.54	0.11	H_0 H_0
$\overline{X} \pm 2 \cdot S$, (74,7)	$N(1.53, 0.10^2)$ $LN(0.42, 0.06^2)$	1.53	0.10	H_0 H_0
Frequency 1.9 Hz (Data points, intervals)	Distribution	$\overline{X}_r$ [Hz]	S_r [Hz]	Accepted hypothesis
$\overline{X} \pm 4 \cdot S$, (141,8)	$N(1.90, 0.10^2)$ $LN(0.64, 0.05^2)$	1.90	0.10	H_0 H_0
$\overline{X} \pm 2 \cdot S$, (134,7)	$N(1.90, 0.08^2)$ $LN(0.64, 0.04^2)$	1.90	0.08	H_0 H_0
Frequency 2.0 Hz (Data points, intervals)	Distribution	$\overline{X}_r$ [Hz]	S_r [Hz]	Accepted hypothesis
$\overline{X} \pm 4 \cdot S$, (183,11)	$N(2.02, 0.13^2)$ $LN(0.70, 0.06^2)$	2.02	0.13	H_A H_A
$\overline{X} \pm 2 \cdot S$, (172,8)	$N(2.00, 0.10^2)$ $LN(0.69, 0.05^2)$	2.00	0.10	H_0 H_0
Frequency 2.1 Hz (Data points, intervals)	Distribution	$\overline{X}_r$ [Hz]	S_r [Hz]	Accepted hypothesis
$\overline{X} \pm 4 \cdot S$, (161,11)	$N(2.11, 0.13^2)$ $LN(0.75, 0.06^2)$	2.11	0.13	H_0 H_0
$\overline{X} \pm 2 \cdot S$, (155,9)	$N(2.11, 0.11^2)$ $LN(0.74, 0.05^2)$	2.11	0.11	H_0 H_0
Frequency 2.5 Hz (Data points, intervals)	Distribution	$\overline{X}_r$ [Hz]	S_r [Hz]	Accepted hypothesis
$\overline{X} \pm 4 \cdot S$, (137,12)	$N(2.52, 0.17^2)$ $LN(0.92, 0.08^2)$	2.52	0.17	H_A H_A
$\overline{X} \pm 2 \cdot S$, (135,12)	$N(2.51, 0.15^2)$ $LN(0.92, 0.06^2)$	2.51	0.15	H_0 H_0

Table D.3: Results of jumping tests for person P1.

The results shown in Table D.3 and Table D.4 are somewhat ambiguous. The mean values of the samples are in all cases very close to the tested beat frequency. This shows that in an

Frequency 1.5 Hz (Data points, intervals)	Distribution	$\bar{X}_r$ [Hz]	S_r [Hz]	Accepted hypothesis
$\bar{X} \pm 4 \cdot S$, (112,9)	$N(1.52, 0.11^2)$ $LN(0.42, 0.07^2)$	1.52	0.11	H_0 H_0
$\bar{X} \pm 2 \cdot S$, (110,8)	$N(1.52, 0.10^2)$ $LN(0.41, 0.07^2)$	1.52	0.10	H_0 H_0
Frequency 1.9 Hz (Data points, intervals)	Distribution	$\bar{X}_r$ [Hz]	S_r [Hz]	Accepted hypothesis
$\bar{X} \pm 4 \cdot S$, (138,11)	$N(1.89, 0.14^2)$ $LN(0.64, 0.07^2)$	1.89	0.14	H_A H_A
$\bar{X} \pm 2 \cdot S$, (132,9)	$N(1.89, 0.11^2)$ $LN(0.64, 0.06^2)$	1.89	0.11	H_A H_0
Frequency 2.0 Hz (Data points, intervals)	Distribution	$\bar{X}_r$ [Hz]	S_r [Hz]	Accepted hypothesis
$\bar{X} \pm 4 \cdot S$, (145,10)	$N(2.01, 0.13^2)$ $LN(0.70, 0.06^2)$	2.01	0.13	H_A H_A
$\bar{X} \pm 2 \cdot S$, (137,8)	$N(2.01, 0.10^2)$ $LN(0.70, 0.05^2)$	2.01	0.10	H_0 H_0
Frequency 2.1 Hz (Data points, intervals)	Distribution	$\bar{X}_r$ [Hz]	S_r [Hz]	Accepted hypothesis
$\bar{X} \pm 4 \cdot S$, (148,12)	$N(2.09, 0.16^2)$ $LN(0.74, 0.08^2)$	2.09	0.16	H_0 H_0
$\bar{X} \pm 2 \cdot S$, (144,9)	$N(2.09, 0.15^2)$ $LN(0.74, 0.07^2)$	2.09	0.15	H_0 H_0
Frequency 2.5 Hz (Data points, intervals)	Distribution	$\bar{X}_r$ [Hz]	S_r [Hz]	Accepted hypothesis
$\bar{X} \pm 4 \cdot S$, (169,14)	$N(2.50, 0.19^2)$ $LN(0.92, 0.08^2)$	2.50	0.19	H_0 H_0
$\bar{X} \pm 2 \cdot S$, (163,13)	$N(2.49, 0.16^2)$ $LN(0.91, 0.06^2)$	2.49	0.16	H_0 H_0

Table D.4: Results of jumping tests for person P2.

average sense, person P1 and P2 are able to jump with the same frequency, which they hear from the music. Also, the standard deviations are fairly low, and naturally, the standard deviations are lower for the $(\bar{X} \pm 2 \cdot S)$-cases compared to the $(\bar{X} \pm 4 \cdot S)$-cases due to the limited data. For a frequency of 2.5 Hz, especially for person P2, the highest standard deviation is found. Despite that it is not obvious from the results of the 1.5 Hz tests, it seemed more natural to jump at a frequency around 2.0 Hz, while the frequencies at 1.5 Hz and 2.5 Hz required more concentration jumpers to keep in time with the beat.

When it comes to the results of the chi-square test for goodness of fit, it is harder to draw a general conclusion. In some tests, the normal distribution seems to be the best fit, yet in other tests the lognormal distribution exhibits the best fit. No tendency can be found. In this regard, it should be mentioned that the outcome of the tests is very dependent on the chosen number of intervals in the histogram as well as the limiting case $(\bar{X} \pm 4 \cdot S)$ or $(\bar{X} \pm 2 \cdot S)$, and as a consequence no final conclusion can be drawn from the chi-square test towards the statistical distribution of the jumping frequencies.

Two different cases of the tests results are shown in Figure D.5 and Figure D.6. For Figure D.5, good agreement between the fitted lognormal distribution and the sample data is obtained. This is obviously due the fact that there are no "outliers" in the data set as seen from the histogram and the standard deviation is relatively low. Conversely for Figure D.6, the fitted normal distribution is distorted by a quite broad histogram on both sides of the mode of the sample. A comparison of these two cases underlines the sensitivity of the chi-square test for goodness of fit.

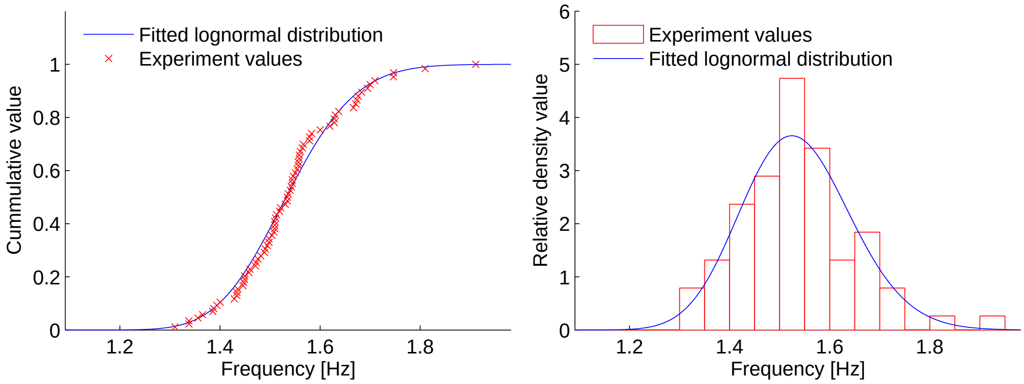

Figure D.5: Person P1, 1.5 Hz, $(\bar{X} \pm 4 \cdot S)$, $LN(0.43, 0.07^2)$.

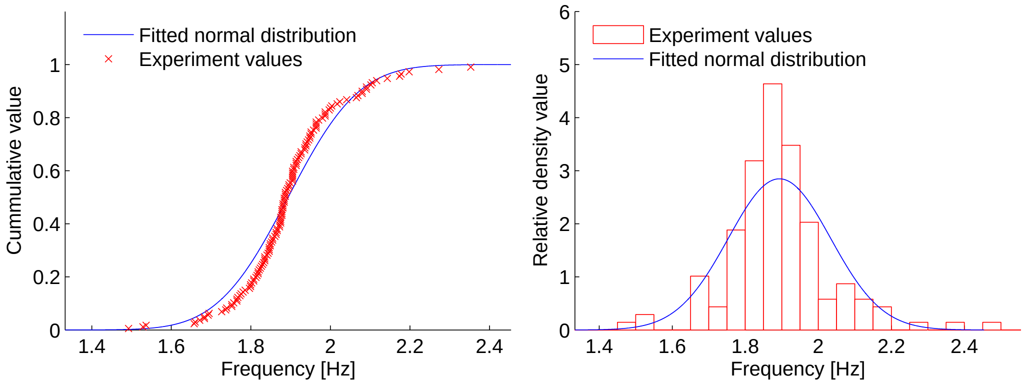

Figure D.6: Person P2, 1.9 Hz, $(\bar{X} \pm 4 \cdot S)$, $N(1.89, 0.14^2)$.

To obtain a better estimate of the distribution of jumping loads than achieved in this case, longer jumping series should measured, and probably also different pieces of music should be used. Nevertheless, the results show that a person is able to jump in time with a known frequency from a piece of music, but in this process it should be expected that jumps, which are both of a higher and lower frequency than the target frequency, occur. In relation to load modelling this means that human jumping at e.g. 2.0 Hz in reality consists of a narrow band of frequencies in the neighbourhood of 2.0 Hz.

Appendix **E**

Load Model Validation

In order to comment on the validity of the load models simulating the load generated by jumping humans as suggested by Eurocode 1 [11] and Ellis & Ji [8], tests were performed in the laboratory. The tests are used to investigate the contact ratio as described by Ellis & Ji and compare the Fourier coefficients and phases corresponding to each load component.

A set-up consisting of three force transducers with a very stiff steel plate on top was used for the tests as seen in Figure E.1. The force transducers used for the tests are model C2 10 kN produced by HBM capable of measuring up to 150 kN with a nominal force of 10 kN. The purpose of the steel plate is to distribute the force from the jump to the transducers without any absorption of force within the plate itself. Jumping on the set-up can be seen in Figure E.2.

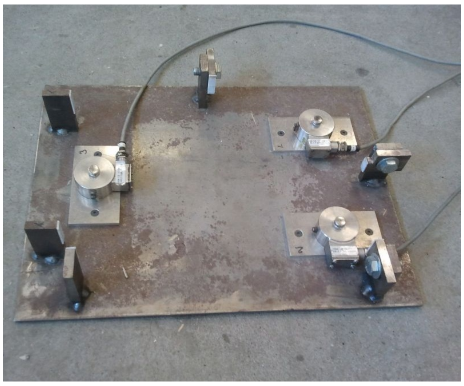

Figure E.1: Set-up used for measuring jumping force.

Figure E.2: Jumping on experiment set-up.

This tripod-like support condition makes the plate quite likely to tilt when the jumper hits its outer positions. A tilt of the steel plate results in loss of connection to one of the transducers and makes the plate slam back at the transducer subsequently, making the data signal quality suffer. A full data signal can be seen in Figure E.3, and a zoom in on the signal after a small plate impact can be seen in Figure E.4 to visualize the effect. All data from this study is treated in `Load_Validation.m`.

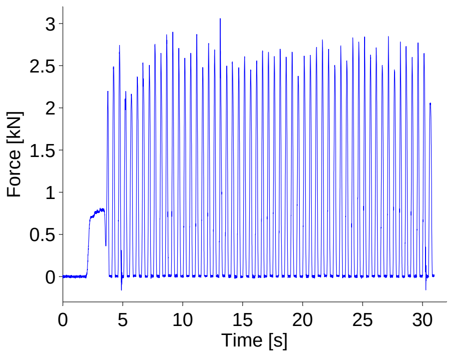

Figure E.3: Full jumping load data signal.

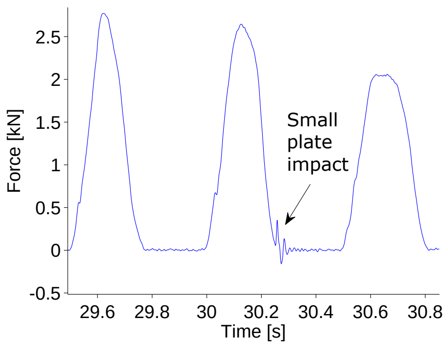

Figure E.4: Effect on signal from plate impact.

E.1 Contact Ratio

The contact ratio c_r is a quantity used in the load model proposed by Ellis & Ji. It is given as the ratio between the contact duration t_c and the period of the jumping motion T_p. The load model is based on that the jumping load can be described as semi-sinusoidal pulses as seen in Eq. (E.1).

$$F(t) = \begin{cases} K_p G \sin(\pi t / t_c) & 0 \leq t \leq t_c \\ 0 & t_c < t \leq T_p \end{cases} \tag{E.1}$$

where

K_p F_{max}/G.
F_{max} Peak dynamic load.
G Weight of the jumper [kN].

The contact ratio and the factor K_p are related as seen in Eq. (E.2), and hence the contact ratio can be estimated by using the average peak data values and the weight of the jumper [8]. This is the first method to estimate the contact ratio.

$$K_p = \frac{\pi}{2c_r}\,, \qquad c_r = \frac{\pi G}{2F_{max}} \tag{E.2}$$

Two other methods, besides the relation between the peak force and the jumper's weight given in Eq. (E.2), are used for estimating the contact ratio from the experiments. These depend on more visual and geometric analysis of the signal. When analyzing the data obtained in the laboratory, the period of the jumping motion is determined from the time interval between each succeeding peak. The contact duration, which is needed to identify the contact ratio, can however be estimated in several ways. The first method is based on defining a threshold close to zero, but above the noise level of the force signal. The threshold is from experience set to 0.2 kN. Signal positions corresponding to each crossing of the threshold are searched throughout the signal, and t_c is calculated as the time difference between each point. In Figure E.5 the relevant data points such as F_{max}, marked by red circles, and t_c crossings, marked by red crosses, are illustrated in a zoom in on the full signal for the sake of understanding. The contact ratio is by this method calculated by averaging the values of t_c and T_p, and using Eq. (E.3).

$$c_r = \frac{t_c}{T_p} \tag{E.3}$$

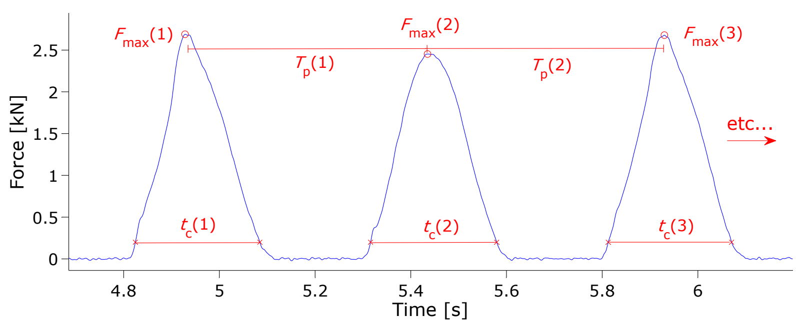

Figure E.5: Relevant data points for signal analysis.

The final method of estimating the contact ratio is a geometric approach using the trigonometric properties of a sine curve. For any sine curve, the time difference between data points of half the peak amplitude will relate to the time difference at zero by the factor 1.5. This means that a threshold at half the average peak amplitude value $F_{\max}/2$ can be introduced, and t_c is then calculated by multiplying the average value of the time between crossings of the threshold, as illustrated in the previous method, by a factor of 1.5.

The contact ratio was estimated through a series of experiments with two persons jumping for approximately 15 s at both 2.0 Hz and 2.1 Hz, five times for each frequency. The results are seen in Table E.1, where the method number refers to the estimation method, numbered in the same order as introduced above.

PERSON AND FREQUENCY	METHOD	CONTACT RATIO 1	2	3	4	5	Mean	
P1 at 2.0 Hz	1	0.45	0.47	0.46	0.47	0.43	**0.46**	**0.45**
	2	0.47	0.49	0.46	0.49	0.46	**0.47**	
	3	0.42	0.45	0.43	0.45	0.41	**0.43**	
P1 at 2.1 Hz	1	0.43	0.43	0.45	0.38	N/A	**0.42**	**0.43**
	2	0.47	0.47	0.49	0.43	N/A	**0.47**	
	3	0.41	0.42	0.43	0.36	N/A	**0.41**	
P2 at 2.0 Hz	1	0.47	0.48	0.48	0.45	0.43	**0.46**	**0.47**
	2	0.51	0.46	0.51	0.50	0.48	**0.49**	
	3	0.45	0.42	0.46	0.44	0.42	**0.44**	
P2 at 2.1 Hz	1	0.51	0.48	0.45	0.46	0.45	**0.47**	**0.48**
	2	0.53	0.51	0.50	0.50	0.50	**0.51**	
	3	0.48	0.46	0.45	0.44	0.43	**0.45**	

Table E.1: Estimated contact ratios.

From the results it is seen that method two gives the highest contact ratio estimates. It is obviously because it depends on the defined threshold; the higher the threshold, the lower contact ratio. The first and third method, which both rely on the peak values $F_{\max}$, give quite similar results. Also, it can be noted that the second jumper seems to have slightly higher contact ratio than the first. Averaging all the tests, a general contact ratio for jumping at around 2 Hz can be set to $c_r = 0.46$, which corresponds to a typical value for rhythmic exercise and high impact aerobics [7].

E.2 Fourier Coefficients

Both the Eurocode load model and the model proposed by Ellis & Ji are based on representing the jumping load by means of a Fourier series as shown in Eq. (E.4) and Eq. (E.5).

$$F(t) = G\left(1.0 + \sum_{i=1}^{\infty} a_i \cos\left(\frac{2\pi i}{T_p} t\right) + \sum_{i=1}^{\infty} b_i \sin\left(\frac{2\pi i}{T_p} t\right)\right) \tag{E.4}$$

$$= G\left(1.0 + \sum_{i=1}^{\infty} \alpha_i \sin\left(\frac{2\pi i}{T_p} t + \varphi_i\right)\right) \tag{E.5}$$

where

G Static load of person.

α_i Fourier coefficient for the i^{th} jumping load component, $\alpha_i = \sqrt{a_i^2 + b_i^2}$.

φ_i Phase lag for the i^{th} jumping load component, $\varphi_i = \tan^{-1}\left(\frac{a_i}{b_i}\right)$.

T_p Period of jumping motion.

The Eurocode model provides three Fourier coefficients and leaves the determination of phase lags to the user, whereas the Ellis & Ji model determines the factors a_i and b_i from the contact ratio [8]. Initially the Ellis & Ji model was used on the form shown in Eq. (E.5) as one would offhand think, that using the relations between α_i, φ_i and a_i, b_i would make the choice of formulation indifferent. The formulation given by Eq. (E.5) makes it possible to compare the Fourier coefficients of both the models and was hence more convenient to use. When comparing the force calculated by both models, inconsistency was experienced around certain values of contact ratio, and it was chosen to investigate the importance of the formulation. In Figure E.6, 3D plots show the load as formulated by Equations (E.4) and (E.5) as function of contact ratio in a small time interval.

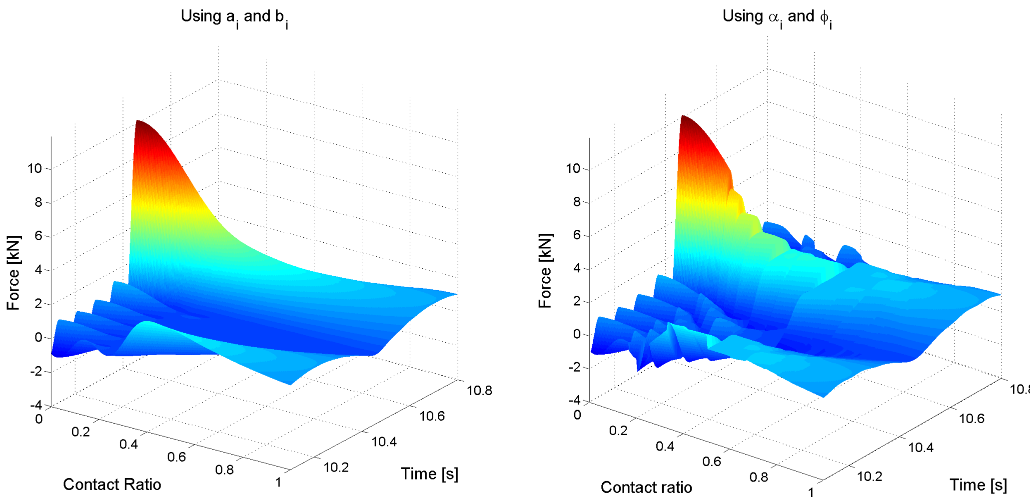

Figure E.6: 3D plots of different load formulations.

As seen in the figure, the force calculated by Eq. (E.5) shows clear disjoints around certain contact ratios. A further investigation of the formulation showed that caution should be taken with the conversion of a_i and b_i to φ_i, $\varphi_i = \tan^{-1}(a_i/b_i)$. It was found that a more appropriate formulation could be used, namely $\varphi_i = \tan 2^{-1}(-b_i/a_i)$, where $\tan 2$ is a function that adds 180° or π to φ_i whenever a_i takes on negative values. Using this new relation between a_i, b_i and φ_i indeed made the choice of formulation indifferent, and furthermore made the comparison of Fourier coefficients possible.

Using the contact ratio previously determined to be $c_r = 0.46$ for general jumping at around 2 Hz, the Fourier coefficients from the Ellis & Ji model can be calculated using the relation, $\alpha_i = \sqrt{a_i^2 + b_i^2}$. Ellis & Ji suggest using the first 6 harmonic components to which the Fourier coefficients at $c_r = 0.46$ becomes: 1.63, 0.81, 0.11, 0.14, 0.06 and 0.05. These values are close to the values given by the Eurocode for the first three components; 1.6, 1.0 and 0.2.

The Fourier coefficients from jumping can also be estimated from the performed experiments. This is done by analyzing the FFT plots. In the models just described, the Fourier coefficients match discrete frequency values corresponding to integer multipliers of the jumping frequency. In the case of an FFT plot of a measured signal, a number of data points will appear around the wanted frequency, depending on the quality and resolution of the FFT signal. The Fourier coefficient equal to a discrete frequency can be set to the sum of the data points in a defined range around the peak. In the following, three data points are included around the first two load components and two for the third. Due to the small magnitude of the higher components, only the first three components are assessed.

PERSON AND FREQUENCY	i	FOURIER COEFFICIENT, α_i					
		1	2	3	4	5	Mean
P1 at 2.0 Hz	1	1.79	1.64	1.60	1.73	1.54	**1.66**
	2	1.13	0.91	0.98	0.93	0.91	**0.97**
	3	0.22	0.18	0.20	0.10	0.19	**0.18**
P1 at 2.1 Hz	1	1.72	1.64	1.47	1.46	N/A	**1.57**
	2	1.06	0.97	0.83	0.95	N/A	**0.95**
	3	0.24	0.19	0.16	0.33	N/A	**0.23**
P2 at 2.0 Hz	1	1.86	1.76	1.55	1.87	1.84	**1.78**
	2	0.96	1.04	0.76	1.07	1.09	**0.98**
	3	0.12	0.18	0.10	0.20	0.22	**0.16**
P2 at 2.1 Hz	1	1.87	1.95	1.88	1.88	1.72	**1.86**
	2	0.92	1.00	0.94	1.07	0.95	**0.97**
	3	0	0.10	0.11	0.15	0.17	**0.11**

Table E.2: Estimated Fourier coefficients.

The Fourier coefficients estimated from the experiments are listed in Table E.2 and can now be compared with with the values suggested by Eurocode and the model by Ellis & Ji. For the sake of completeness the values by Ellis & Ji are calculated to match the contact ratios of each test as listed in Table E.1.

CONTACT RATIO	MODEL	FOURIER COEFFICIENTS		
		α_1	α_2	α_3
–	EC	1.6	1.0	0.2
0.43	Ellis & Ji	1.68	0.92	0.22
	Experiment	1.57	0.95	0.23
0.45	Ellis & Ji	1.65	0.85	0.14
	Experiment	1.66	0.97	0.18
0.47	Ellis & Ji	1.62	0.78	0.08
	Experiment	1.78	0.98	0.16
0.48	Ellis & Ji	1.60	0.74	0.05
	Experiment	1.86	0.97	0.11

Table E.3: Comparison of model and estimated Fourier coefficients.

As seen from the results, the measured jump forces from person P1 provide Fourier coefficient values closer to the values suggested by Eurocodes, and values calculated from the Ellis & Ji model, than the forces measured from person P2. The values estimated from the experiments are connected with a lot of uncertainty, as they depend a lot on the quality of the signal obtained from the FFT analysis. Especially when bearing this in mind, the values obtained from P1 fit both models very nicely. The coefficients obtained from P2 are on the other hand not in agreement with the models. When detecting high α_1 values, one would expect a low contact ratio, but the contact ratio investigation of P2 jumps showed contact ratios near $c_r = 0.50$. This lead to the conclusion that if the experiments were to be used for determination of the actual Fourier coefficients, longer samples would be required, so that the FFT plot would achieve a higher resolution. Nevertheless the obtained values support the models chosen for this project.

Appendix **F**

Newmark Time Integration

This appendix describes the Newmark time integration method used for solving the equations of motion throughout the report. The matter of the appendix is based on [18] and [20].

The general Newmark time integration method is expressed by the following equations for the unknown displacement vector $\mathbf{u}$:

$$\mathbf{M}\ddot{\mathbf{u}}_{j+1} + \mathbf{C}\dot{\mathbf{u}}_{j+1} + \mathbf{K}\mathbf{u}_{j+1} = \mathbf{F}_{j+1}\,, \qquad j = 1, \ldots, n \tag{F.1}$$

$$\mathbf{u}_{j+1} = \mathbf{u}_j + \dot{\mathbf{u}}_j \Delta t + \left(\left(\frac{1}{2} - \beta \right) \ddot{\mathbf{u}}_j + \beta \ddot{\mathbf{u}}_{j+1} \right) \Delta t^2 \tag{F.2}$$

$$\dot{\mathbf{u}}_{j+1} = \left((1-\gamma)\, \ddot{\mathbf{u}}_j + \gamma \ddot{\mathbf{u}}_{j+1} \right) \Delta t \tag{F.3}$$

Eq. (F.1) is the equation of motion at the time t_{j+1}. Eq. (F.2) and Eq. (F.3) are approximate Taylor expansions. The γ and β values show the approximation of the acceleration in the time intervals, e.g. parameters $(\gamma,\beta) = \left(\frac{1}{2}, \frac{1}{6}\right)$ indicates linear variation and $(\gamma,\beta) = \left(\frac{1}{2}, \frac{1}{4}\right)$ indicate constant acceleration in the interval, see Figure F.1.

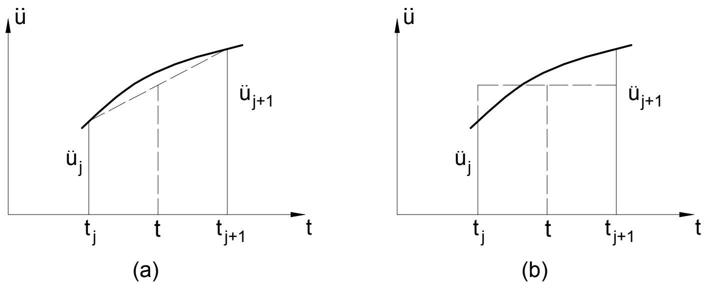

Figure F.1: Approximation of acceleration in the time intervals. (a) $(\gamma,\beta) = \left(\frac{1}{2}, \frac{1}{6}\right)$, (b) $(\gamma,\beta) = \left(\frac{1}{2}, \frac{1}{4}\right)$.

The process diagram of the Newmark algorithm is shown in Figure F.2. For the known initial displacement $\mathbf{u}_0$ and velocity $\dot{\mathbf{u}}_0$ vectors, the load vector $\mathbf{F}$, the system mass, stiffness and damping matrices $\mathbf{M}$, $\mathbf{K}$, $\mathbf{C}$ are used to determine the initial acceleration $\ddot{\mathbf{u}}_0$. Next n repetitions is done for the chosen time step Δt. In the loop predictors, the new displacement and velocity are calculated, and from these a new acceleration is calculated. Finally, a new displacement and velocity are estimated. The algorithm can be found in `Newmark.m`. The following items identify the accuracy for the Newmark time integration.

- *Truncation error*: error caused by truncation of the digits
- *Numerical stability*: error related with dissipation of a given disturbance
- *Period errors*: error related with elongation or shortening of the period
- *Numerical damping*: error related with amplitude errors

The errors, except the first, are dependent of the chosen γ and β values. In this report, the (γ,β) parameters are assumed to be $\left(\frac{1}{2}, \frac{1}{4}\right)$. Hereby, the algorithm is unconditionally stable despite

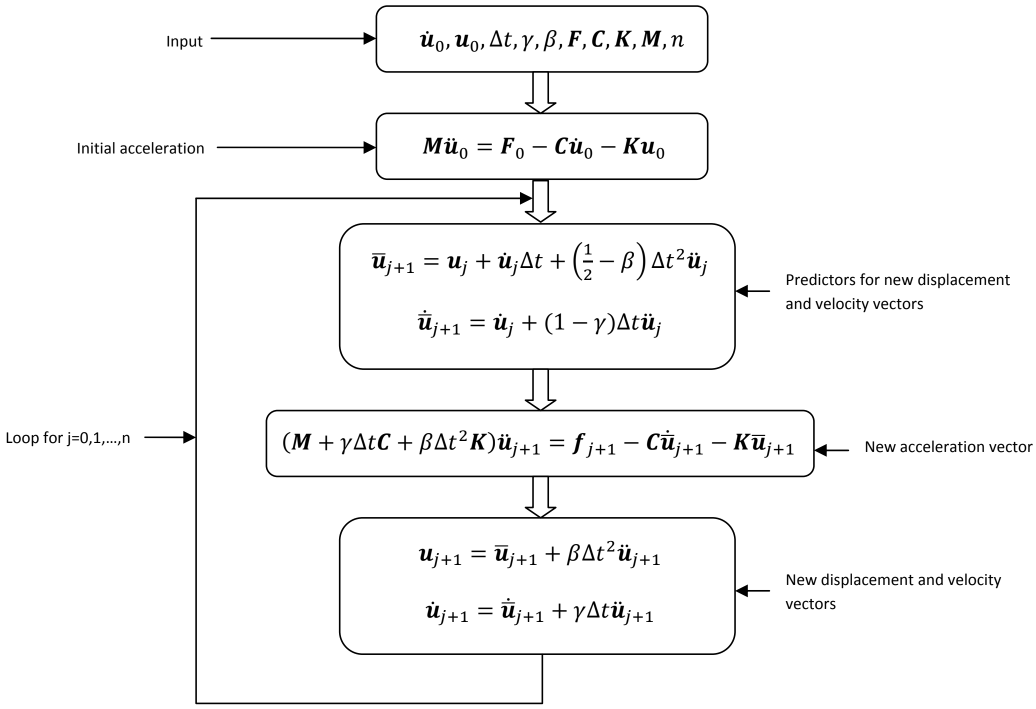

Figure F.2: Newmark algorithm.

any time step, as it fulfils the condition of Eq. (F.4) [18].

$$\frac{1}{2} \leq \gamma \leq 2\beta \tag{F.4}$$

The relative period error is evaluated in Eq. (F.5).

$$\frac{\Delta T}{T} = \frac{\bar{T} - T}{T} = \left(\frac{1}{96}\left(12\gamma^2 - 36\gamma + 11\right) + \frac{1}{2}\beta\right)\kappa^2 + o(\kappa^4) \quad , \quad \kappa = \omega_1 \cdot \Delta t \tag{F.5}$$

Eq. (F.5) indicates that $\bar{T} > T$, which means that the solution will have period elongation, independent of the chosen time step. The time step is chosen from reference [20]. It indicates that good accuracy is obtained when the time step fulfils Eq. (F.6).

$$\Delta t = \frac{\pi}{50\omega_1} \approx 1.7 \cdot 10^{-3} \tag{F.6}$$

Here the angular frequency ω_1 corresponds to the first eigenmode. The numerical damping error has no influence on the solution as the parameter γ is chosen to be equal to $\frac{1}{2}$. This means that no amplitude errors are introduced.

Literature

[1] **Andersen and Frigaard, 2008**.
T.L. Andersen and P. Frigaard.
Lecture Notes for the Course in Water Wave Mechanics, 2008.

[2] **Ayyub and McCuen, 2003**.
Bilal M. Ayyub and Richard H. McCuen.
Probability, Statistics and Reliability for Engineers and Scientists.
Chapman & Hall/CRC, 2nd edition, 2003.

[3] **Bachmann et al., 1995**.
H. Bachmann et al.
Vibration Problems in Structures: Practical Guidelines.
Birkhäuser, 2nd edition, 1995.

[4] **Clough and Penzien, 1975**.
R.W. Clough and J. Penzien.
Dynamics of Structures.
McGraw-Hill, Inc., 1975.
ISBN 0-07-011392-0.

[5] **Cook, Malkus, Plesha, and Witt, 2002**.
Robert D. Cook, David S. Malkus, Michael E. Plesha, and Robert J. Witt.
Concepts and Applications of Finite Element Analysis.
John Wiley & Sons Inc., 4th edition, 2002.
ISBN 978-0-471-35605-9.

[6] **Dickinson, 1978**.
S.M. Dickinson.
The Buckling and Frequency of Flexural Vibration of Rectangular Isotropic and Orthotropic Plates using Rayleigh's Method.
Journal of Sound and Vibration, 61(1), pp. 1–8, 1978.

[7] **Ellis and Ji, 2004**.
B.R. Ellis and T. Ji.
The response of structures to dynamic crowd loads.
BRE Digest, 426, 2004.

[8] **Ellis and Ji, 1994**.
B.R. Ellis and T. Ji.
Floor vibration induced by dance-type loads: theory.
The Structural Engineer, 72(3), pp. 37–44, 1994.

[9] **Ellis and Ji, 1994**.
B.R. Ellis and T. Ji.
Floor vibration induced by dance-type loads: verification.
The Structural Engineer, 72(3), pp. 45–50, 1994.

[10] **Erhvervs- og Byggestyrelsen, 2010**.
Erhvervs- og Byggestyrelsen.
Nationalt Anneks til Eurocode 0: Projekteringsgrundlag for bærende konstruktioner.
Erhvervs- og Byggestyrelsen, 5th edition, 2010.

[11] **Erhvervs- og Byggestyrelsen, 2007**.
Erhvervs- og Byggestyrelsen.
Nationalt Anneks til Eurocode 1: Last på bygværker – Del 1-1: Generelle laster – Densiteter, egenlast og nyttelast for bygninger.
Erhvervs- og Byggestyrelsen, 2nd edition, 2007.

[12] **Erhvervs- og Byggestyrelsen, 2007**.
Erhvervs- og Byggestyrelsen.
Nationalt Anneks til Eurocode 2: Betonkonstruktioner–Del 1-1: Generelle regler samt regler for bygningskonstruktioner.
Erhvervs- og Byggestyrelsen, 2nd edition, 2007.

[13] **Hansen and Sørensen, 2002**.
S.O. Hansen and John D. Sørensen.
Dynamic loads due to synchronized movements of people.
Proceedings of the Fourth International Conference on Structural Dynamics, Vol. 2, 2002.

[14] **Iyengar and Iyengar, 1967**.
K.T. Sundara Raja Iyengar and R. Narayana Iyengar.
Determination of the orthotropic plate parameters of stiffened plates and grillages in free vibration.
Applied Scientific Research, 17(6), pp. 422–438, 1967.

[15] **Jensen, 2007**.
Bjarne Chr. Jensen.
Betonkonstruktioner efter DS411.
Nyt Teknisk Forlag, 3rd edition, 2007.

[16] **Jensen et al., 2009**.
Bjarne Chr. Jensen et al.
Teknisk Ståbi.
Nyt Teknisk Forlag, 20th edition, 2009.

[17] **Nielsen, 2004**.
S.R.K. Nielsen.
Vibration Theory, Vol. 1.
Aalborg Universitet, 3rd edition, 2004.

[18] **Nielsen, 2007**.
S.R.K. Nielsen.
Structural Dynamics, Vol. 9.
Aalborg Universitet, 2nd edition, 2007.

[19] **Nordkraft, 2010**.
Nordkraft.
Nordkraft, 2010.
http://nordkraft.dk/.

[20] **Petyt, 1990**.
M. Petyt.
Introduction to Finite Element Vibration Analysis.
Cambridge University Press, 1990.

[21] **Rao, 1990**.
Singiresu S. Rao.
Mechanical Vibrations.
Addison-Wesley Publishing Company, 2nd edition, 1990.

[22] **Sachse, Pavic, and Reynolds, 2003**.
R. Sachse, A. Pavic, and P. Reynolds.
Human-Structure Dynamic Interaction in Civil Engineering Dynamics - A Literature Review, Department of Civil and Structural Engineering, University of Sheffield, 2003.

[23] **Simulia, 2010**.
Simulia.
Abaqus documentation.
Dassault Systèmes Simulia Corp., 2010.

[24] **Spæncom, 2008**.
Spæncom.
Spæncom A/S, 2008.
http://www.spaencom.dk.

[25] **Suikkanen, 2010**.
Bernt Suikkanen.
Vibrationskomfort i dækkonstruktioner, 2010.
http://bef.dk/files/DanskBeton/Betonelement/Publikationer/Vibrationskomfort....pdf.

[26] **Sun, 2006**.
Eric Qiuli Sun.
Shear Locking and Hourglassing in MSC Nastran, ABAQUS, and ANSYS, 2006.
http://www.mscsoftware.com/events/vpd2006/na/presentations/tech_papers/27.pdf.

[27] **Timoshenko**, **1937**.
Stephen P. Timoshenko.
Vibration Problems in Engineering.
D. van Nostrand Company Inc., New York, 2nd edition, 1937.

[28] **Troitsky**, **1976**.
M.S. Troitsky.
Stiffened Plates: Bending, Stability and Vibrations.
Elsevier Scientific Publishing Company, New York, 1976.

[29] **Virklund Sport**, **2010**.
Virklund Sport.
Virklund-Sport A/S, 2010.
http://www.virklund-sport.dk/.

[30] **Zivanovic, Pavic, and Reynolds**, **2005**.
S. Zivanovic, A. Pavic, and P. Reynolds.
Vibration serviceability of footbridges under human-induced excitation: a literature review.
Journal of Sound and Vibration, 279(1-2), pp. 1–73, 2005.